Full length article

The giant Upper Yangtze Pb–Zn province in SW China: Reviews, new advances and a new genetic model

Jia-Xi Zhou[a,c,d,*], Zhen-Zhong Xiang[a,b], Mei-Fu Zhou[c], Yue-Xing Feng[d], Kai Luo[a,b], Zhi-Long Huang[a], Tao Wu[d,e]

[a] Stake Key Laboratory of Ore Deposit Geochemistry, Institute of Geochemistry, Chinese Academy Sciences, Guiyang 550081, China
[b] University of Chinese Academy Sciences, Beijing 100049, China
[c] Department of Earth Sciences, University of Hong Kong, Hong Kong, China
[d] Radiogenic Isotope Facility, School of Earth and Environment Sciences, University of Queensland, Brisbane, QLD 4072, Australia
[e] School of Earth Sciences, Zhejiang University, Hangzhou 310027, China

ARTICLE INFO

ABSTRACT

In the western margin of the Yangtze Block, SW China, the Emeishan large igneous province (ELIP) is spatially associated with > 400 carbonate-hosted epigenetic Pb–Zn deposits. These deposits form the giant Upper Yangtze Pb–Zn metallogenic province with > 20 Mt base metals. In the southeastern part of this province, the important Pb–Zn deposits include those of the Yinchangpo, Yunluhe, Maozhachang, Tianqiao, Banbanqiao, Mangdong, Shaojiwan, Liangyan, Qingshan, Shanshulin, Nayongzhi and Guanziyao deposits. Sulfide ore bodies in these deposits are (i) hosted in late Ediacaran to middle Permian limestone, dolomitic limestone and dolostone; (ii) structurally controlled by reverse fault-anticline tectonic systems; and (iii) spatially associated with the ELIP flood basalts and mafic dikes, and early Permian, early Carboniferous and early Cambrian organic matter-rich black shales. C–O isotopic compositions suggest that dolostone and limestone, mantle-derived rocks of the ELIP, and sedimentary organic matters supplied C–O to the hydrothermal systems through water/rock (W/R) inter-action. New and existing S isotopic compositions of sulfides imply multiple sources of S and the reduction of sulfate through both abiotic thermochemical (TSR) and bacterially mediated (BSR) processes. Zn isotopes in-dicate that the sources of Zn were most likely related to the ELIP with various contributions from sediments and basements locally. Pb isotope signatures are suggestive of derivation of Pb from basements and sedimentary rocks with variable influences from the ELIP. Sr isotopes support that mantle-derived rocks, sediments and basements were involved in Pb–Zn mineralization, and they have various contributions in different deposits. We consider that the Pb–Zn deposits in the Upper Yangtze province are the mixed products of multiple S species-bearing solutions and metal-rich fluids, both of which were derived from, flowed through or interacted with multiple lithostratigraphic units in the western Yangtze Block. The change of tectonic regimes from extension to compression after eruption of basalts of the ELIP, and then to extension during Early Mesozoic, facilitated ex-traction, migration, and excretion of ore-forming metals and associated fluids. Mixing of fluids and reduction geochemical barrier activated TSR, causing cyclical carbonate dissolution, CO_2 degassing and recrystallization (namely carbonate buffer). All these processes triggered continuous precipitation of huge amounts of hydro-thermal minerals. Underplating and eruption of ELIP basalts provided heat flow, fluids and volatiles, whereas the basalts acted as an impermeable and protective layer, and even as ore-hosting rocks. These Pb–Zn deposits have spatial and genetic association with igneous activities of the ELIP, and are characterized by high ore grades (> 10 wt% Pb + Zn), high concentrations of associated metals (e.g. Cu, Ag, Ge, and Cd), and medium-low temperatures (usually < 300 °C) and salinities (commonly < 20 wt% NaCl equiv.), all of which are sig-nificantly different from those of typical Mississippi Valley-type (MVT) deposits. Hence, the carbonate-hosted epigenetic Pb–Zn deposits in the Upper Yangtze metallogenic province representing to a new type of Pb–Zn deposits that are hosted in platform carbonate sequences and formed within compressional zones of passive margin tectonic settings.

* Corresponding author at: Stake Key Laboratory of Ore Deposit Geochemistry, Institute of Geochemistry, Chinese Academy Sciences, Guiyang 550081, China.
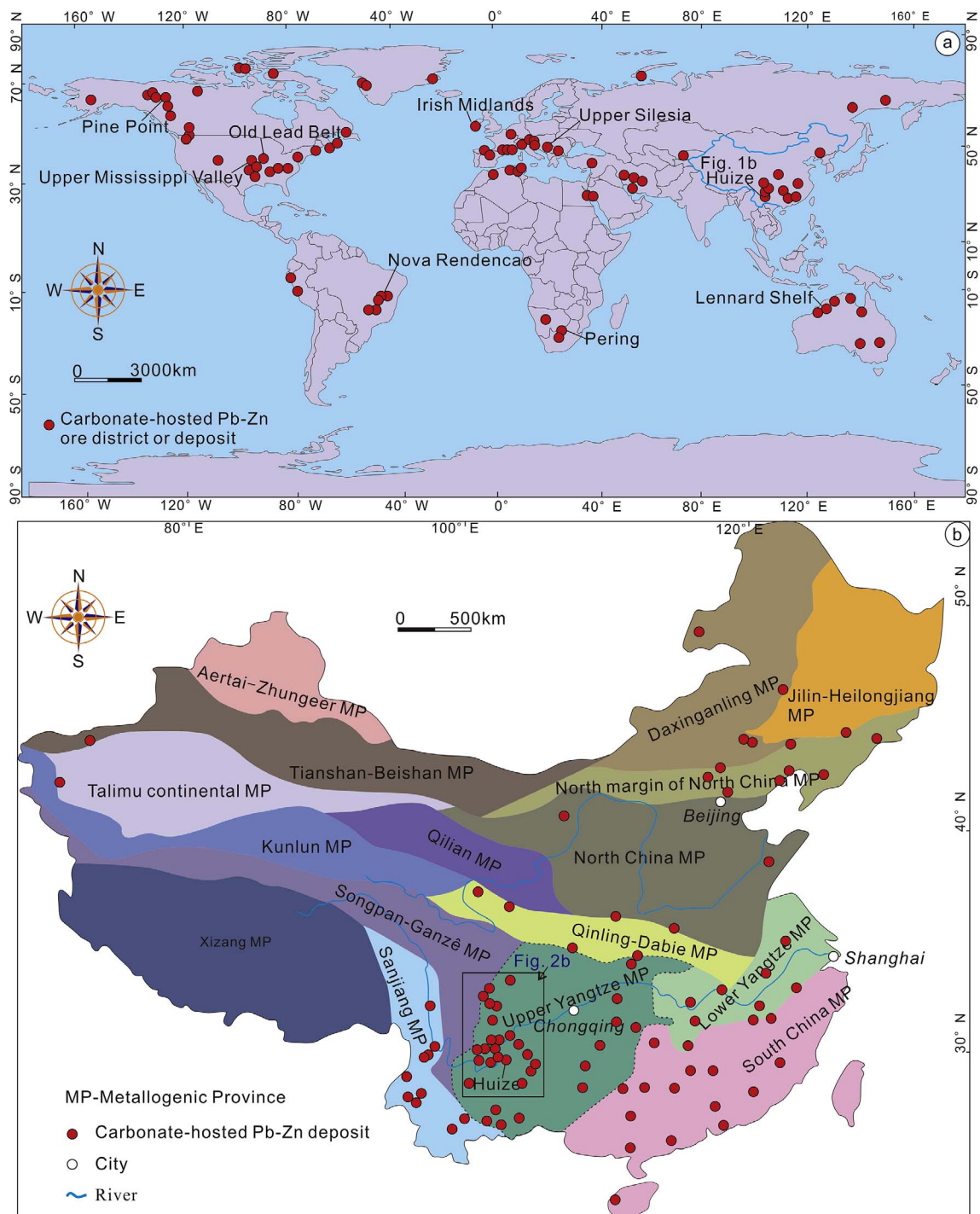 E-mail address: zhoujiaxi@vip.gyig.ac.cn (J.-X. Zhou).

Fig. 1. (a) Global distribution of carbonate-hosted epigenetic Pb–Zn ore districts and deposits (modified from Taylor et al., 2009; Zhang et al., 2015a); (b) distribution of carbonate-hosted epigenetic Pb–Zn deposits in China (modified from Wang et al., 2014; Zhang et al., 2015a).

1. Introduction

Sediment-hosted Pb–Zn deposits, generally absent of temporal or spatial association with igneous activities, contain the greatest Pb and Zn resources in the world, and dominate the worldwide production of these base metals (Leach et al., 2005; Taylor et al., 2009; Zhang et al., 2015a). Carbonate-hosted Pb–Zn deposits (traditionally named as Mississippi Valley-type, MVT), an important type of sediment-hosted Pb–Zn deposits (another vital type is clastic-dominated Pb–Zn deposits, known as sedimentary exhalative, SEDEX), mainly occur in platform carbonate sequences and are typically formed within extensional zones

inboard of orogenic belts at passive margin tectonic settings (Bradley and Leach, 2003; Groves and Bierlein, 2007; Leach et al., 2010). The carbonate-hosted epigenetic Pb–Zn sulfide deposits are distributed in almost all of the countries in the world (Fig. 1a). The most famous ore districts or deposits (Fig. 1a) include the Pine Point in Canada (Powell and Macqueen, 1984), Upper Mississippi Valley in the United States (Leach and Rowan, 1986; Brannon et al., 1992), Irish Midlands in Ireland (Wilkinson et al., 2005), Upper Silesia in Poland (Heijlen et al., 2003), Lennard Shelf in Australia (Tompkins et al., 1994) and the Upper Yangtze in China (Zaw et al., 2007; Zhou et al., 2013a, 2018a; Wang et al., 2014; Zhang et al., 2015b). Although extensive research has
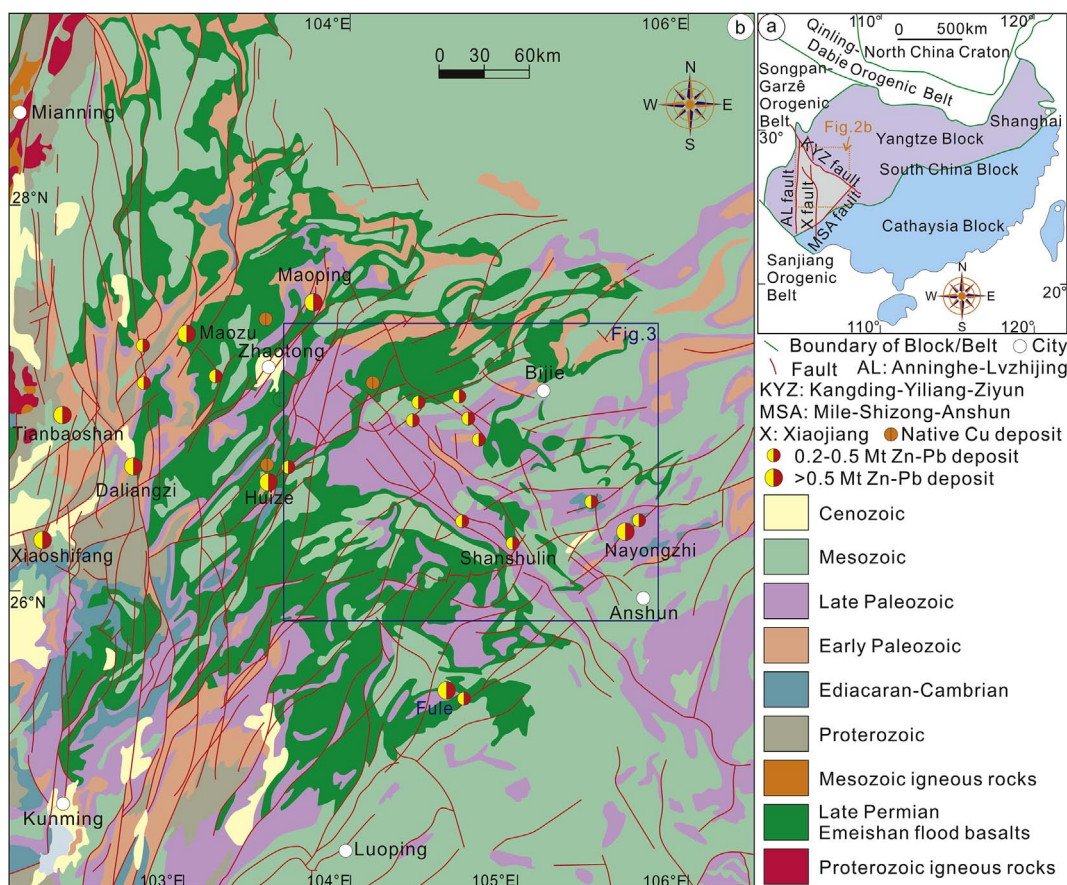
Fig. 2. (a) Regional geological setting of South China; (b) geological sketch map of the Upper Yangtze carbonate-hosted epigenetic Pb–Zn metallogenic province (modified from Liu and Lin, 1999; Yan DP unpublished map).

contributed greatly to the understanding of ore genesis, however, as the carbonate-hosted Pb–Zn deposits are the products of various ore-forming processes in a variety of geological and tectonic settings (Wilkinson et al., 2009; Zhou et al., 2014a, 2018b; Davidheiser-Kroll et al., 2014; Marsh et al., 2016), their mineralization is complex and the ore formation processes are still unclear.

Carbonate-hosted Pb–Zn deposits are abundant in China (Fig. 1b), which are primary sources of Pb and Zn, and significant sources of Ag and Ge (Huang et al., 2004; Wang et al., 2014; Zhang et al., 2015a). Such type of Pb–Zn deposits mainly occurs in South China and are commonly distributed in clusters (Fig. 1b). For example, in the western Yangtze Block (Fig. 2a), > 400 Pb–Zn deposits have been discovered within the triangular domain (~0.2 × 10⁶ km²) of SW Sichuan, NE Yunnan and NW Guizhou provinces (Fig. 2b) (Zheng and Wang, 1991; Liu and Lin, 1999; Huang et al., 2010; Zhou et al., 2013b, 2018b), which constitute the giant Upper Yangtze Pb–Zn metallogenic province (Zhou et al., 2014b). The Upper Yangtze metallogenic province contains > 2000 Mt reserves of sulfide ore, grading 10–35 wt% Pb + Zn (Zhou et al., 2013c), which accounts for 27% of the total Pb + Zn resources in China (Zhang et al., 2015b). The triangular domain of the Upper Yangtze province is structurally bounded by the NE-trending Mile-Shizong-Anshun (MSA), NW-trending Kangding-Yiliang-Ziyun (KYZ) and NS-trending Anninghe-Lvzhijiang (AL) faults (Fig. 2a). In the Upper Yangtze metallogenic province, the Pb–Zn deposits are characterized by (i) sulfide ore bodies stratigraphically occur in the Proterozoic Kunyang Group to middle Permian Qixia-Maokou Formation and are spatially related to mantle-derived rocks of the Emeishan large igneous province (ELIP) (Figs. 2b and 3); (ii) sulfide ore bodies occur as stratiform, lentiform or scrotiform shape within fold bedding-planes or steeply-dipping veins along fault dip planes (Zheng and Wang, 1991; Zhou et al., 2001, 2013d; Wu et al., 2013; Wei et al., 2015; Li et al.,

2015; Zhu et al., 2016a; Bao et al., 2017; Tan et al., 2017); (iii) sulfide ores have high grade, averaging > 10 wt% Pb + Zn, with abundant Ag, Cu, Cd, Ge and Ga (Ye et al., 2011; Zhou et al., 2011, 2018b; Zhu et al., 2017); and (iv) sulfide ores are precipitated from the mantle/metamorphic fluids of medium-low temperatures (< 300 °C) and salinities (< 20 wt% NaCl equiv.) (Huang et al., 2004; Jin, 2008; Bai et al., 2013; Zhou et al., 2013e, Li et al., 2016; Zhang et al., 2015b; Zhu et al., 2016b).

The origin of these Pb–Zn deposits in the Upper Yangtze metallogenic province has been dealt with in literature (e.g. Zhou et al., 2013a; Li et al., 2015; Zhu et al., 2016a; Liu et al., 2017; Kong et al., 2017). However, most of these studies only focused on individual deposits and concerned with ore deposit geology, trace elements, isotopes, geochronology or fluid inclusions. Thus, the regional mineralization and ore formation processes are still lacking (Zhou et al., 2018b), which limits the overall understanding of such type of Pb–Zn sulfide deposits and regional exploration. Sulfide ores in Pb–Zn deposits mainly consist of base metal sulfide minerals (e.g. pyrite, sphalerite, galena and chalcopyrite) and hydrothermal carbonate minerals (such as dolomite and calcite). Hence, the element and isotope geochemistry of these mineralizing elements (e.g. C, O, S, Fe, Cu, Zn and Pb) themselves can directly reveal their sources and the migration paths or evolutions of associated fluids. For example, C–O, S, Zn and Pb, and also Sr isotopes have been wildly used to trace the sources of ore-forming elements and associated fluids, and to reflect the environments of ore formation and the causes of hydrothermal mineral precipitation (e.g. Rye and Sawkins, 1974; Changkakoti et al., 1988; Zheng and Wang, 1991; Kamona et al., 1999; Zhou et al., 2001; Heijlen et al., 2003; Wilkinson et al., 2005; Kelley et al., 2009; Zhou et al., 2010, 2016a; He et al., 2016). Furthermore, laser-ablation multi-collector inductively coupled plasma mass spectroscopy (LA-MC-ICPMS) and secondary ion mass
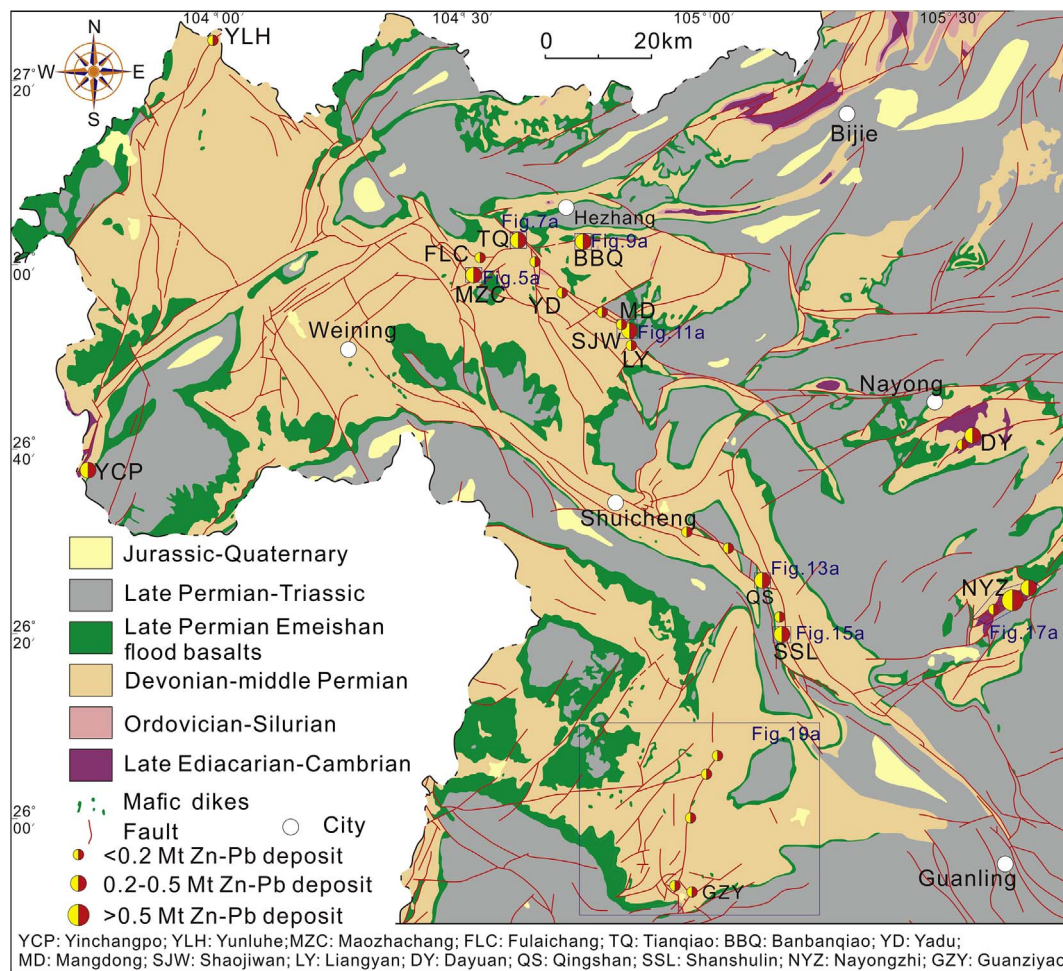
Fig. 3. Geological sketch map of the NW Guizhou district (modified from Zhu et al., 2016a; Zhou et al., 2018a).

spectroscopy (SIMS) can accurately analyze isotopic compositions of hydrothermal minerals in situ and have been widely used in the research of ore genesis (e.g. Ikehata et al., 2008; Barker et al., 2009; Nishizawa et al., 2010; Zhang et al., 2014a; Yuan et al., 2015; Bao et al., 2016, 2017; Zhou et al., 2018a). Here we use two newly-discovered Pb–Zn deposits, the Maozhachang and Liangyan deposits in the NW Guizhou district, southeastern part of the Upper Yangtze metallogenic province, as a case study, utilizing NanoSIMS in situ S and femtosecond (fs) LA-MC-ICPMS in situ Pb isotopic data, together with previously reported bulk data of stable (C–O–S–Zn) and radiogenic (Pb–Sr) isotopes, and detailed field data of twelve typical Pb–Zn deposits, including the Yinchangpo, Yunluhe, Maozhachang, Tianqiao, Banbanqiao, Mangdong, Shaojiwan, Liangyan, Qingshan, Shanshulin, Nayongzhi and Guanziyao deposits, aimed at revealing the regional mineralization and metallogenic processes of the Pb–Zn deposits in the Upper Yangtze metallogenic province, SW China. The outcomes will have wide significance for understanding of the formation of carbonate-hosted epigenetic Pb–Zn deposits and are useful for ore prospecting in the Upper Yangtze Pb–Zn metallogenic province.

2. Geological setting

2.1. General geology of the western Yangtze Block

South China Block is composed of Yangtze and Cathysia blocks, of which the Yangtze Block is tectonically bounded by the Sanjiang Orogenic Belt to the SW, Songpan-Ganzê Orogenic Belt to the NW, Qinling-Dabie Orogenic Belt to the north and Cathysia Block to the

south (Fig. 2a). The Yangtze Block consists of Paleoproterozoic to early Neoproterozoic basement complexes and late Neoproterozoic to Cenozoic cover sequences (Yan et al., 2003; Sun et al., 2008; Hu et al., 2017a, 2017b), of which the former comprises metamorphic rocks (e.g. gneiss, mica schist, amphibolite, marble and quartzite) that were intruded by late Neoproterozoic and Mesozoic igneous rocks (Fig. 2b) (Gao et al., 2011; Zhou et al., 2014c), and the latter is made up of sedimentary and volcanic rocks (Figs. 3 and 4; Liu and Lin, 1999; Huang et al., 2004; Jin, 2008). The sedimentary cover sequences consist of late Neoproterozoic (Ediacaran) to early Mesozoic (Triassic) marine and late Mesozoic (Jurassic) to Cenozoic (Quaternary) continental sedimentary rocks, namely carbonate and clastic rocks, as well as other sediments (Figs. 3 and 4) (Liu and Lin, 1999; Zhou et al., 2013a; Hu et al., 2017a, 2017b). The volcanic rocks are late Permian continental flood basalts of the ELIP (Fig. 2b) (Zhou et al., 2002). The platform carbonate sequences constitute a key part of Ediacaran to Triassic marine strata, and are rich in evaporites and organic matters, as well as contain numerous Pb–Zn sulfide deposits and Au deposits (Huang et al., 2004; Jin, 2008; Cheng et al., 2015a; Zhou et al., 2014a, 2018a, 2018b). Tectonics that strictly control sedimentation, magmatism and mineralization in the western Yangtze Block are characterized by multistage activities (Hercynian, Indosinian, Yanshanian, and Himalayan orogenic events) (Figs. 2 and 3).

A significant feature of the western Yangtze Block is the occurrence of the late Permian ELIP (~260 Ma), which covers ~ $7 \times 10^5 \, km^2$ of the western Yangtze Block (Fig. 2b) and eastern Songpan-Ganzê Orogenic Belt, with displaced correlative units in northern Vietnam (Song Da zone) (Zhou et al., 2002; Xu et al., 2007; Shellnutt, 2014; Zhong

Formation		Lithology	Thickness (m)	Lithological character
Quaternary			0-21	Gravel, sandy soil, and diluvium.
Palaeogene			0-60	Conglomerate, claystone, sandstone, and marl.
Cretaceous			0-230	Mudstone, marlstone, sandstone, and siltstone.
Jurassic			100-700	Sandstone, marlstone, mudstone, and quartz sandstone.
Triassic	Guanling		12-775	Limestone and marl; Sandstone and mud dolomite; Limestone and black shale.
Triassic	Yongzhen-ning		0-485	Limestone, shale, and dolomitic limestone.
Triassic	Feixianguan Daye		0-358	Sandstone, shale, limestone, and claystone.
Permian	Longtan		147-360	Sandstone, shale, and claystone, hosting coal.
Permian	Emeishan Basalts		>400	Flood basalts, hosting native Cu ore body
Permian	Qixia-Maokou		>400	Limestone, dolomiti/bioclastic limestone, hosting Pb-Zn ore body, i.e. Shaojiwan
Permian	Liangshan		80-187	Sandstone, calcareous shale, and argillaceous siltstone, hosting Pb-Zn ore body, i.e. Qingshan
Carboni-ferous	Maping		189-347	Limestone, dolomitic limestone, bioclastic limestone, dolostone, hosting Pb-Zn ore body, i.e. Yinchangpo

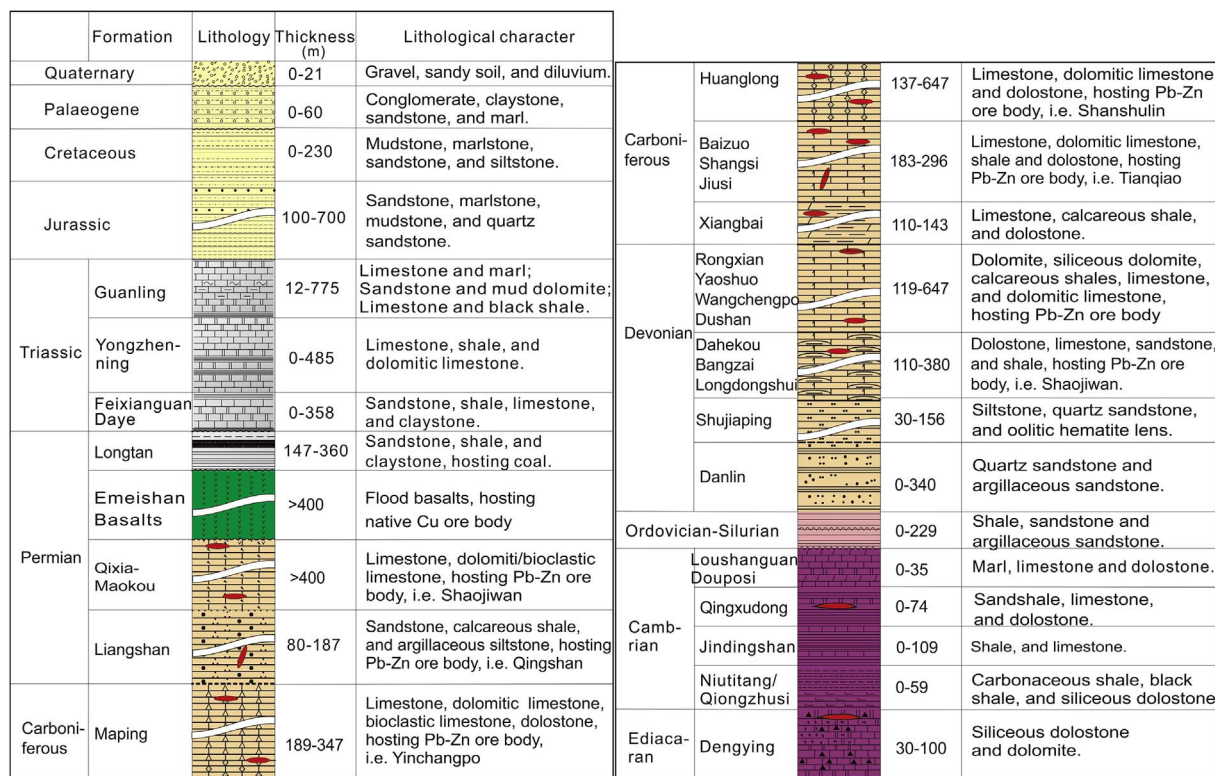|	Formation	Thickness	Lithological character
Carboni-ferous	Huanglong	137-647	Limestone, dolomitic limestone, and dolostone, hosting Pb-Zn ore body, i.e. Shanshulin
Carboni-ferous	Baizuo Shangsi Jiusi	183-296	Limestone, dolomitic limestone, shale and dolostone, hosting Pb-Zn ore body, i.e. Tianqiao
Carboni-ferous	Xiangbai	110-143	Limestone, calcareous shale, and dolostone.
Devonian	Rongxian Yaoshuo Wangchengpo Dushan	119-647	Dolomite, siliceous dolomite, calcareous shales, limestone, and dolomitic limestone, hosting Pb-Zn ore body
Devonian	Dahekou Bangzai Longdongshui	110-380	Dolostone, limestone, sandstone, and shale, hosting Pb-Zn ore body, i.e. Shaojiwan
Devonian	Shujiaping	30-156	Siltstone, quartz sandstone, and oolitic hematite lens.
Devonian	Danlin	0-340	Quartz sandstone and argillaceous sandstone.
Ordovician-Silurian		0-229	Shale, sandstone and argillaceous sandstone.
Cambrian	Loushanguan Douposi	0-35	Marl, limestone and dolostone.
Cambrian	Qingxudong	0-74	Sandshale, limestone, and dolostone.
Cambrian	Jindingshan	0-109	Shale, and limestone.
Cambrian	Niutitang/ Qiongzhusi	0-59	Carbonaceous shale, black shale, and siliceous dolostone.
Ediacaran	Dengying	30-100	Siliceous dolostone and dolomite.

Fig. 4. Integrated histogram of strata and their concise lithologies in the NW Guizhou district (modified from Jin, 2008).

et al., 2014; Li et al., 2017; Liu et al., 2017). Many economically important Fe–Ti–V oxide deposits, Ni–Cu-(PGE) sulfide deposits, native Cu deposits, Pb–Zn deposits (Fig. 2b) and Carlin-type Au deposits occur within the ELIP (Liu and Lin, 1999; Zhou et al., 2002, 2018b; Ali et al., 2005; Zhu et al., 2007; Jian et al., 2009; Chen et al., 2015a; Zhang et al., 2015b; Tran et al., 2016; Hu et al., 2017a; Wang et al., 2017). Emeishan continental flood basalts constitute an important part of the ELIP, and are up to ~5 km maximum thickness in Yunnan part, whereas the maximum thickness is only a few hundred meters in Guizhou part (Xu et al., 2001; Pirajno, 2013; Shellnutt, 2014). The basalts are also the host rocks of native Cu deposits and a few Pb–Zn deposits (Liu and Lin, 1999; Zhu et al., 2007). After eruption of Emeishan basalts, the Indosinian Orogeny (257–200 Ma) resulted from the closure of Paleo-Tethys Ocean (Carter et al., 2001; Lepvrier et al., 2004; Enkelmann et al., 2007; Reid et al., 2007; Pullen et al., 2008; Qiu et al., 2016), causing the formation of fault-fold tectonic systems that structurally controlled the occurrence of hydrothermal deposits (such as native Cu, Pb–Zn and Au) in the western Yangtze Block (Fig. 2b) (Zaw et al., 2007; Zhu et al., 2007; Zhou et al., 2013a, 2018a; Wang et al., 2014; Chen et al., 2015a; Zhang et al., 2015b; Hu et al., 2017b).

In the western Yangtze Block, the Upper Yangtze Pb–Zn metallogenic province covers ~0.2 × 10⁶ km² of SW Sichuan, NE Yunnan and NW Guizhou provinces, and hosts 408 carbonate-hosted Pb–Zn deposits in late Mesoproterozoic (Kunyang Group) to late Paleozoic (middle Permian Qixia-Maokou Formation) that spatially associated with late Permian Emeishan basalts (Fig. 2b) (Liu and Lin, 1999; Xu et al., 2014; Zhou et al., 2014a, 2018b; Wang et al., 2014; Zhang et al., 2015b; Hu et al., 2017a). Timing of these Pb–Zn deposits in the Upper Yangtze metallogenic province was constrained between 245 Ma and 192 ± 7 Ma (including two peaked ages of 245–220 Ma and 215–190 Ma) according to Pb model ages, and isochron ages of calcite/fluorite Sm–Nd and sphalerite/pyrite Rb–Sr isotope systems (Guan and Li, 1999; Li et al., 2007; Lin et al., 2010; Mao et al., 2012; Zhou et al., 2013a, 2013e, 2015; Zhang et al., 2015b; Hu et al., 2017b).

2.2. Geology of the NW Guizhou district

The NW Guizhou district is located in the southeastern part of the Upper Yangtze Pb–Zn metallogenic province (Fig. 2b). In this district, the Proterozoic basement metamorphic rocks are not exposed, the cover sequences comprise late Ediacaran-Triassic marine and Jurassic-Quaternary continental carbonates and clastic rocks (and other sediments), as well as late Permian volcanic rocks (Emeishan basalts) (Figs. 3 and 4) (Wang, 1994; Jin, 2008; Zhou et al., 2013a). The late Ediacaran Dengying Formation is mainly composed of dolostone, which is conformably overlain by early Cambrian Qiongzhusi, Niutitang, Jindingshan and Qingxudong Formations that mainly consist of shale and carbonate rocks. Early Cambrian sedimentary rocks are conformably overlain by marl and carbonate rocks of middle Cambrian Douposi Formation and late Cambrian Loushanguan Formation. Sedimentary rocks of the Loushanguan Formation are unconformably overlain by Ordovician-Silurian shale and sandstone, which are in turn unconformably overlain by early Devonian Danlin Formation sandstone. Sandstone of the Danlin Formation is conformably overlain by siltstone, sandstone, shale and carbonate rocks of middle Devonian Shujiaping, and Longdongshui, Bangzai and Dahekou Formations, which are conformably overlain by late Devonian Dushan, Wangchengpo, Yaoshuo and Rongxian Formations that mainly consists of shale and carbonate rocks. Sedimentary rocks of late Devonian are conformably overlain by shale and carbonate rocks of early Carboniferous Xiangbai, Jiusi, Shangsi and Baizuo Formations, which are in turn conformably overlain by late Carboniferous Huanglong and Maping Formations that are mainly made up of carbonate rocks. Late Carboniferous carbonate rocks are conformably overlain by early Permian Liangshan Formation sandstone, shale and siltstone, which are conformably overlain by middle Permian Qixia-Maokou Formation that is mainly composed of carbonate rocks. Carbonate rocks of the Qixia-Maokou Formation are disconformably overlain by late Permian Emeishan and Longtan Formations that mainly consist of basalts and coal-bearing clastic rocks, respectively, of which the latter is conformably overlain by early
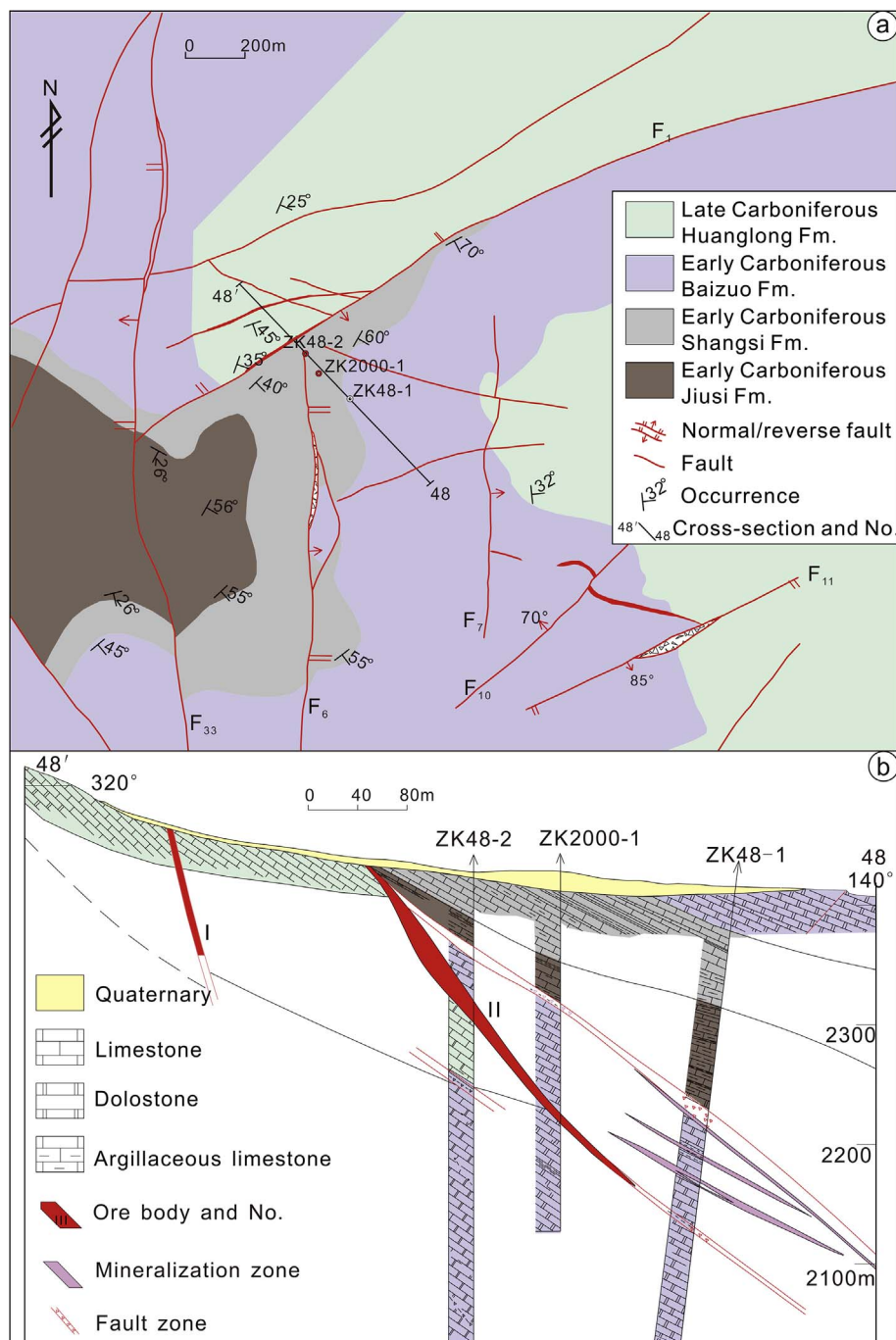
Fig. 5. (a) Geological sketch map of the Maozhachang Pb–Zn deposit (modified from Jin, 2008); (b) cross-section map of No. 48 exploration line (modified from Jin, 2008).

Triassic Daye, Feixianguan and Yongzhenning Formations that are mainly made up of sandstone, shale, claystone and carbonate rocks. Sedimentary rocks of early Triassic are conformably overlain by middle Triassic Guanling Formation that mainly consists of shale, marl, sandstone and carbonate rocks, which are unconformably overlain by Jurassic strata that mainly comprise sandstone, marlstone and mudstone. Cretaceous-Quaternary sediments sparsely unconformable overlie on Cambrian-Triassic sedimentary and volcanic rocks (Figs. 3 and 4).

Faults and folds in the NW Guizhou district are well developed, which can be divided into NNE-, NE-, NEE and NW-trending groups that mainly include the NNE-trending Yinchangpo-Yunluhe, NEE-trending Maozhachang-Banbanqiao, NW-trending Tianqiao-Liangyan and Qingshan-Shanshulin, and NE-trending Dayuan, Nayongzhi and Guanziyao fault-fold tectonic systems (Jin, 2008; Zhou et al., 2013a, 2014b, 2018a; Chen et al., 2015b, 2017; Jin et al., 2016a, 2016b; Liu

et al., 2017; Zeng et al., 2017). Among these tectonic systems, the NW-trending Tianqiao-Liangyan and Qingshan-Shanshulin are attached to the regional Kangding-Yiliang-Ziyun deep fault (KYZ in Fig. 2a), which strictly controlled sedimentation, magmatism and mineralization in the NW Guizhou district (Fig. 3) (Jin, 2008). Most tectonic systems are mainly composed of a series of high angle reverse faults and Jura-type folds, of which reverse faults and anticlines jointly controlled the occurrence of Pb–Zn sulfide ore (Figs. 5, 7, 9 and 11) (Jin, 2008; Zhou et al., 2013b, 2014a; Liu et al., 2017). For example, the NNE-trending Yinchangpo-Yunluhe tectonic belt is also a Pb–Zn mineralization zone, in which typical deposits are the Yinchangpo and Yunluhe Pb–Zn deposits (Fig. 3).

The Emeishan flood basalts and mafic dikes (diabase) related to the ELIP occur in the NW Guizhou district and are spatially associated with Pb–Zn deposits (Fig. 3). More than 100 Pb–Zn deposits have been found
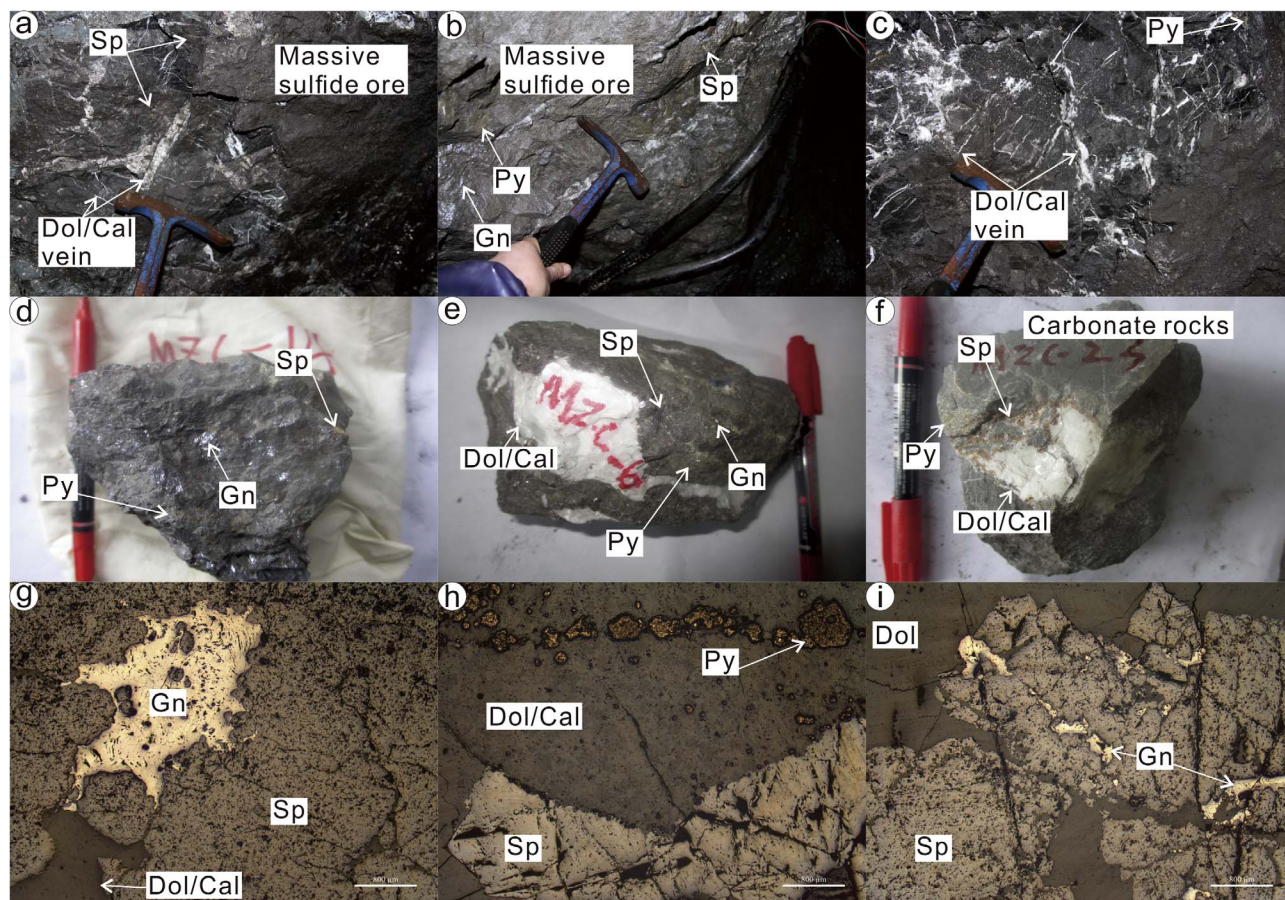
Fig. 6. Photographs of field, hand specimens and microscope; (a) massive sulfide ore, sphalerite occurs in massive shapes and dolomite/calcite presents as veins; (b) massive sulfide ore, sphalerite, pyrite and galena occur in massive types; (c) pyrite forms massive aggregations and dolomite/calcite occurs as veins; (d) massive sulfide ore, sphalerite, pyrite and galena occur in massive shapes; (e) dolomite/calcite occurs as fragments fill the fracture of sphalerite, pyrite and galena massive aggregations; (f) sphalerite, pyrite and dolomite/calcite occurs as veinlets or fragments in carbonate rocks; (g) galena and dolomite/calcite fill the fractures of sphalerite; (h) granular pyrite enclosed by dolomite/calcite that coexists with sphalerite; (i) dolomite and galena veins fill the fractures of sphalerite. Sp = sphalerite; Py = pyrite; Gn = galena; Dol = dolomite; Cal = calcite.

in this district, most of which are hosted by carbonate rocks of early Cambrian Qingxudong Formation and Carboniferous (Fig. 4). Among these Pb–Zn deposits, the Nayongzhi is the largest one, which contains total Pb + Zn metal reverses more than 1.5 Mt (Jin et al., 2016b; Zhou et al., 2018a). The general features of these Pb–Zn deposits are summarized in Table 1. The following sections are focused on the geology of several chosen Pb–Zn deposits.

3. Geology of typical Pb–Zn ore deposits

3.1. Maozhachang

The newly-discovered Maozhachang Pb–Zn deposit is located in the central part of the NW Guizhou district (Fig. 3). In the Maozhachang mining area, the exposed strata are Carboniferous, including early Carboniferous Jiusi, Shangsi and Baizuo Formations, and late Carboniferous Huanglong Formation (Fig. 5a) (Jin, 2008). The Jiusi Formation that mainly consists of shale and limestone is conformably overlain by the Shangsi Formation that comprises dolomitic limestone and limestone, which is in turn conformably overlain by the Baizuo Formation that is mainly composed of dolomitic limestone and dolostone. The Huanglong Formation is mainly made up of limestone and dolostone, which conformably overlays on carbonate rocks of the Baizuo Formation (Figs. 4 and 5). In addition, clay layers of Quaternary sparsely distributed on Carboniferous rocks (Fig. 5b).

Structures in the Maozhachang ore district mainly include the NS-, NE- and NW-trending faults and the SE-dipping monoclinal structure

(Fig. 5a). The F_1 is a high angle reverse fault and trends to the NE (Fig. 5a), which belongs to the NEE-trending Maozhachang-Banbanqiao fault (Fig. 3). Other important structures, such as the F_6 and F_{33} are NS-trending normal faults, and the F_{11} is a NE-trending normal fault. Among these faults, the F_1 reverse fault and the NS-trending normal faults are the main ore-controlling structures (Jin, 2008).

The Maozhachang Pb–Zn deposit is famous for its oxidized and placer ores (Jin, 2008), of which the former is hosted by Carboniferous carbonate rocks (Fig. 5b) and the latter is hosted by clay layers of Quaternary. Placer ore is in planar distribution, whereas oxidized ore occurs as scrotiform or lentiform shape, both of which have earthy, crusty, aciniform and faviform structures (Jin, 2008). No. I oxidized ore body trends N32°–55°E and dips S60°–75°E, and No. II oxidized ore body trends N65°E, dipping S62°E. Oxidized and placer ores mainly consist of smithsonite, cerusite, and limonite, with rare anglesite and hemimorphite. No. I oxidized ore body contains average grades of Pb 0.77 wt% and Zn 6.27 wt%, and No. II oxidized ore body has mean grades of Pb 0.83 wt% and Zn 9.18 wt%. The total Pb + Zn metal reverses of oxidized and placer ores are more than 0.25 Mt (Jin, 2008).

Recently, sulfide ore has been discovered in the deep part of the Maozhachang ore district, which occurs in stratiform or lentiform shape (Fig. 6a–c) and consists mainly of sphalerite, galena and pyrite as ore minerals, and dolomite and calcite (with rare barite) as gangue minerals (Fig. 6a–i). Sulfide minerals form massive, banded, veined and disseminated structures (Fig. 6a–f), with granular, eutectic, and stress deformation textures (Fig. 6g–i). Sulfide ore has mean grades of 0.63–1.23 wt% Pb and 11.69–12.71 wt% Zn. Ore formation in this
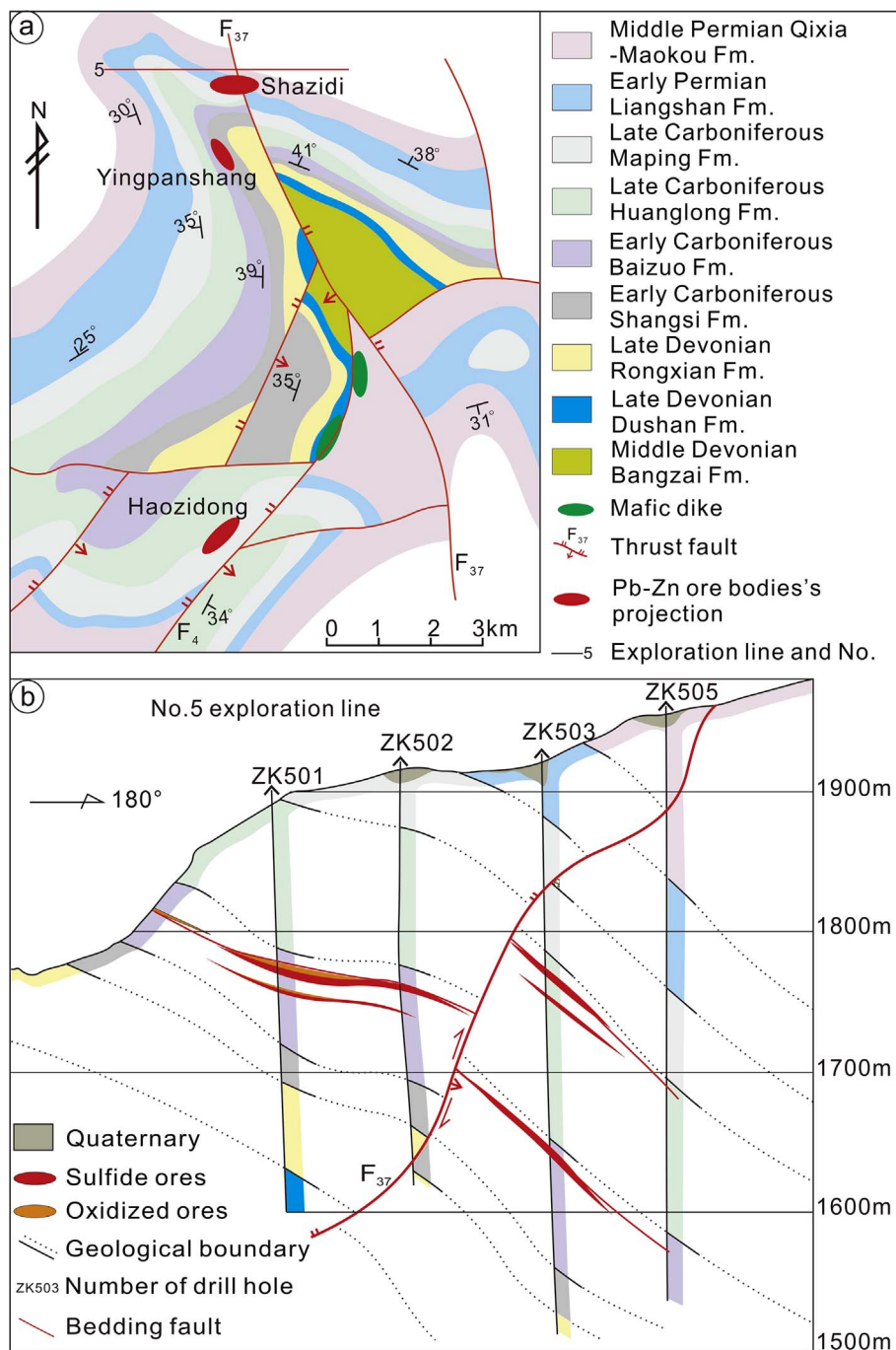
Fig. 7. (a) Geological sketch map of the Tianqiao Pb–Zn deposit (modified from Jin, 2008; Zhou et al., 2013a); (b) cross-section map of No. 5 exploration line (modified from Jin, 2008; Zhou et al., 2014a).

deposit has experienced hydrothermal and supergene processes, of which the former can be divided into sulfide + carbonate and carbonate ± barite phases. Wall rock alteration in the Maozhachang ore district is not complex and mainly includes dolomization, calcilization, Fe/Mn carbonatization and baratization (Table 1).

3.2. Tianqiao

The Tianqiao Pb–Zn deposit is located NE near to the Maozhachang deposit (Fig. 3). Geology of the Tianqiao deposit has been described in detail by Zhou et al. (2013a, 2014a), hence only a brief account of local geology is given here. In the Tianqiao mining area, the exposed strata are middle Devonian Bangzai, late Devonian Dushan and Rongxian, early Carboniferous Shangsi and Baizuo, late Carboniferous Huanglong and Maping, early Permian Liangshan and middle Permian Qixia-

Maokou Formations (Fig. 7a). The Bangzai Formation that mainly consists of siltstone and quartz sandstone is conformably overlain by the Dushan Formation that mainly comprises dolostone, dolomitic limestone and claystone, which is in turn conformably overlain by limestone and dolostone of the Rongxian Formation. Carbonate rocks of the Rongxian Formation are unconformably overlain by the Shangsi Formation, which is conformably overlain by the Baizuo Formation. The Baizuo Formation is conformably overlain by the Huanglong Formation, which is in turn conformably overlain by the Maping Formation that mainly consists of limestone and dolostone. The lithologies of the Shangsi, Baizuo and Huanglong Formations are similar to those in the Maozhachang mining area, and the lithologies and sequence stratigraphic relationships of the Maping, Liangshan and Qixia-Maokou Formations please refer the specification above (Section 2.2; Fig. 4).

The Devonian, Carboniferous and Permian rocks form the Tianqiao
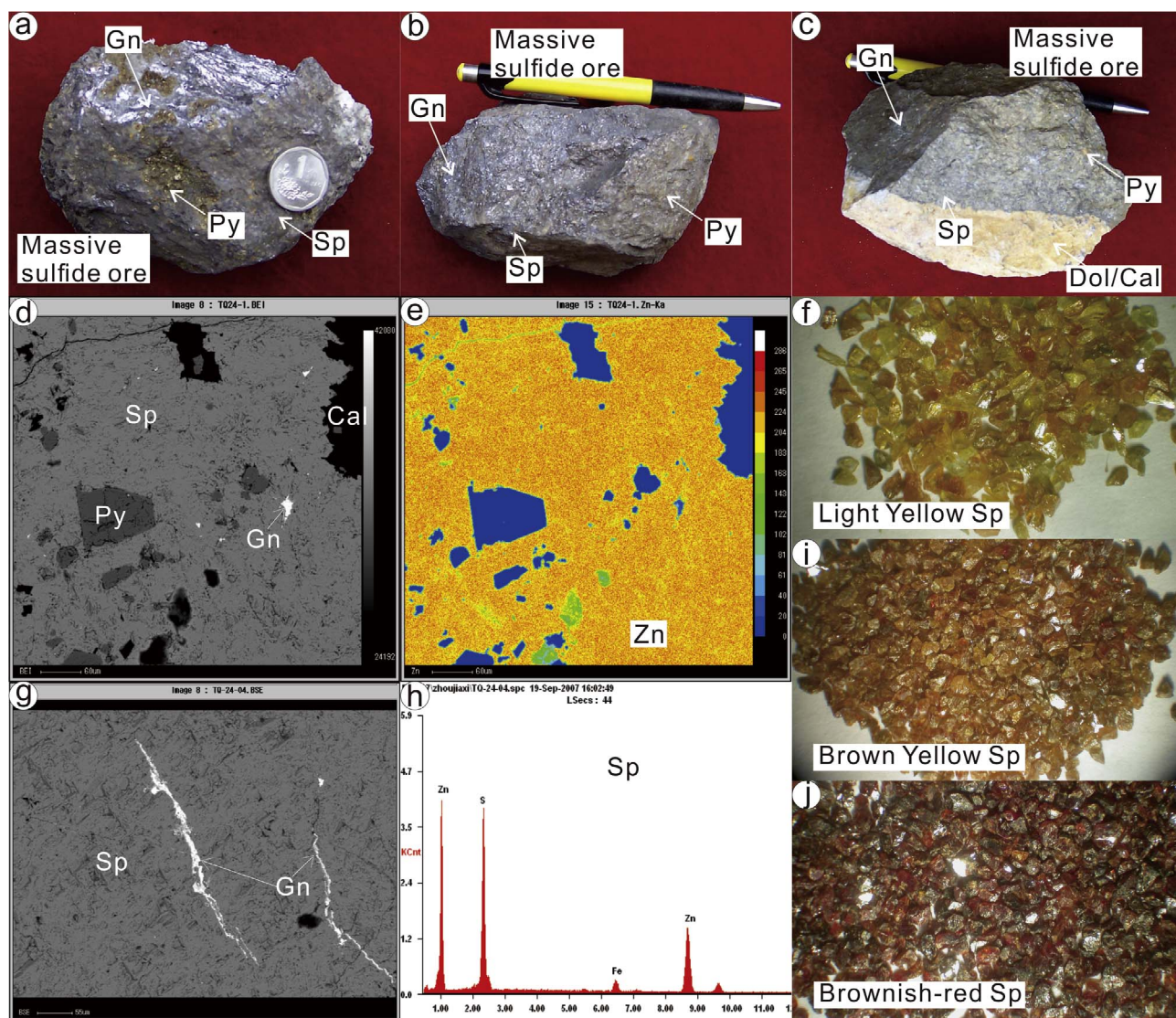
Fig. 8. Photographs of hand specimens, microscope and EPMA; (a)–(b) massive sulfide ore, sphalerite, pyrite and galena occur in massive shapes; (c) massive sulfide ore, sphalerite, pyrite and galena occur in massive types and coexists dolomite/calcite; (d) granular pyrite and galena enclosed by sphalerite that is filled by calcite; (e) Zn elemental mapping; (f) light yellow sphalerite; (g) galena veinlets fill the fractures of sphalerite; (h) energy spectrum diagram of sphalerite; (i) brown yellow sphalerite; (j) brownish-red sphalerite. Sp = sphalerite; Py = pyrite; Gn = galena; Dol = dolomite; Cal = calcite. (For interpretation of the references to color in this figure legend, the reader is referred to the web version of this article.)

anticline, whose axial plane strikes N45°–60°W, and two limbs dip NE and SW with dipping angles of 30°–45° (Fig. 7a). The Devonian rocks form the core of the Tianqiao anticline, and two limbs comprise Carboniferous and Permian rocks (Fig. 7a). Being the largest fault in the mining area, the F_{37} reverse fault is 14 km long with a 1–6 m wide shear zone and crosscuts the Tianqiao anticline (Fig. 7a and b). It strikes N50–90°E and dips 50°–70° to the NE. The tectonic relationship between the Tianqiao anticline and the F_{37} reverse fault was considered to be synchronous (Zhou et al., 2013a).

Thirty-two ore bodies, hosted by carbonate rocks of the Baizuo and Huanglong Formations, and occurred as stratiform or lentiform shape within two limbs of the Tianqiao anticline, forming Shazidi and Yingpanshang sulfide ore sections (Fig. 7a and b). Another Haozidong oxidized ore section, is located within the southwestern limb of the Tianqiao anticline (Fig. 7a). The largest ore body in the Shazidi section is 320 m long, 220 m wide and 1.7–5.2 m thick, with grades of 0.04–7.32 wt% Pb and 0.49–26.7 wt% Zn. The largest ore body in the Yingpanshang section is 200 m long, 100 m wide and 1.3–1.8 m thick. Ore in this body has average grades of 1.23 wt% Pb and 15.69 wt% Zn.

Sulfide ore is mainly composed of sphalerite, galena and pyrite, with calcite and dolomite as gangue minerals (Fig. 8a–d, g–h). In addition, a small amount of chalcopyrite, quartz, barite, fluorite and clay minerals are also present (Zhou et al., 2013a, 2014a). These minerals form massive (Fig. 8a–c), disseminated or banded ore structure, with granular, filled, enclosed, replacement, eutectic, and stress deformation textures (Fig. 8d and e, g) (Zhou et al., 2013a, 2014a). Sulfide minerals formed in sulfide + carbonate ± quartz ± fluorite hydrothermal phase. There are three generations of sphalerite have been recognized according to their different crystal habits and colors (Fig. 8f, i–j), as well as mineral assemblages (Zhou et al., 2013a, 2014a). Wall rock alteration in the Tianqiao mining area is relatively complex, including mainly dolomization, calcilization, Fe/Mn carbonatization, baratization, silicification and fluoritization (Table 1) (Zhou et al., 2013a, 2014a).

3.3. Banbanqiao

The newly-discovered Banbanqiao Pb–Zn deposit is located east near to the Tianqiao deposit (Fig. 3). In the Banbanqiao mining area, the exposed strata are early Carboniferous Shangsi, late Carboniferous Huanglong, early Permian Liangshan and middle Permian Qixia-Maokou Formations (Fig. 9a). The Shangsi Formation is unconformably
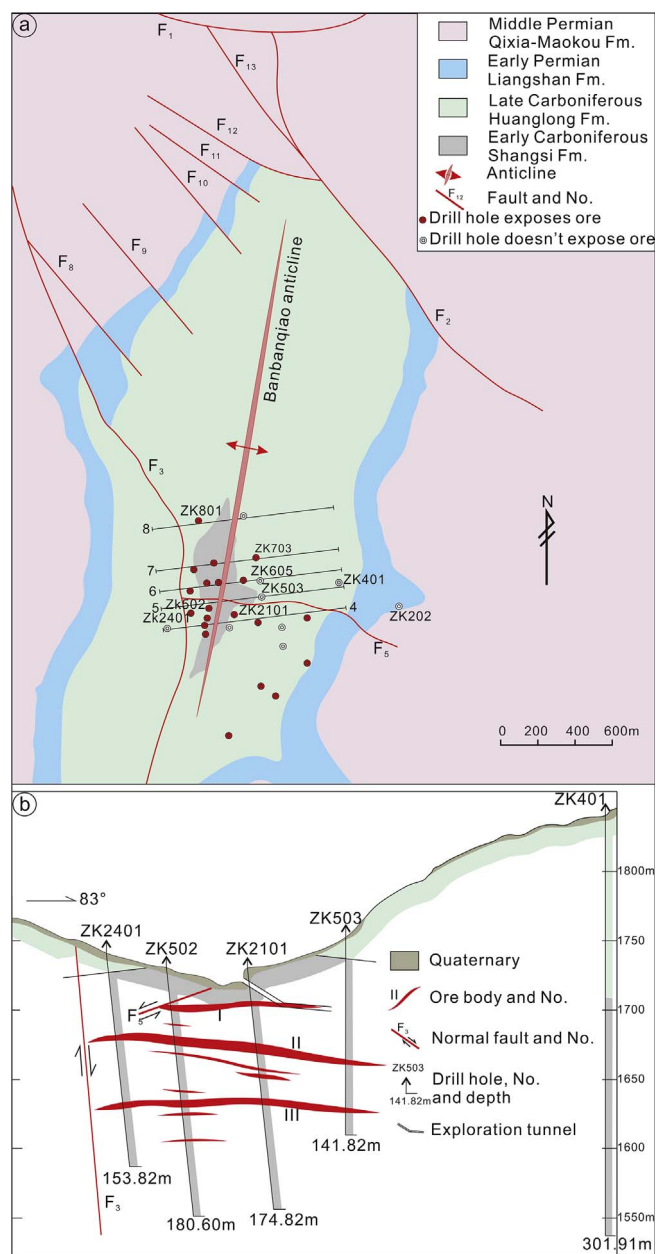
Fig. 9. (a) Geological sketch map of the Banbanqiao Pb–Zn deposit (modified from Zhou et al., 2014a; Li et al., 2015); (b) cross-section map of No. 5 exploration line (modified from Zhou et al., 2014a; Li et al., 2015).

overlain by the Huanglong Formation, which is in turn unconformably overlain by the Liangshan Formation (Zhou et al., 2014b; Li et al., 2015). The lithologies of the Shangsi and Huanglong Formations are similar to those in the Maozhachang and Tianqiao mining areas, and the lithologies and sequence stratigraphic relationships of the Liangshan and Qixia-Maokou Formations please refer the illustration above (Section 2.2; Fig. 4).

Sedimentary rocks of the Shangsi, Huanglong, Liangshan and Qixia-Maokou Formations form the Banbanqiao anticline (Fig. 9a and b), of which the Shangsi Formation rocks form the core part and the rocks of the Huanglong, Liangshan and Qixia-Maokou Formations form the two limbs. In addition, the EW- and NW-trending faults are developed, such as the E-W-trending Dushan-Huamianzhai (F_1 in Fig. 10a) and the NE-trending F_3 faults (Figs. 3 and 9a). The F_1 is a reverse fault, belonging to the Maozhachang-Banbanqiao regional fault, with dipping angles between 40° and 70°, and the F_3 is normal fault that has dipping angles of 45°–85°.

Sulfide ore in the Banbanqiao deposit mainly occurs as stratiform shape (Fig. 9b). Three main ore bodies have been found in the Banbanqiao mining area, of which No. II ore body is the largest one and occurs within the Banbanqiao anticline (Fig. 9b). The Banbanqiao deposit contains > 1.5 Mt of sulfide ore with grades of 0.26–10.32 wt% Pb and 0.81–28.8 wt% Zn (Li et al., 2015). Oxidized ore has complex mineral assemblages, including smithsonite, limonite, cerussite, and sulfides, as well as carbonate minerals (Fig. 10b). Sulfide ore displays either massive, disseminated, breccia cemented veins or banded structure, and mainly consists of sphalerite, pyrite and galena as ore minerals, and calcite, dolomite and quartz as gangue minerals (Fig. 10c–i). Hydrothermal minerals have anhedral to euhedral granular, metasomatic, filled, enclosed, or stress deformation texture (Fig. 10g–i). Three generations of sphalerite with different crystal habits, colors (Fig. 10g–i), and mineral assemblages were formed in the hydrothermal sulfide phase (Zhou et al., 2014a; Li et al., 2015). Wall rock alteration in the Banbanqiao deposit is simple and includes dolomization, calcilization, Fe-Mn carbonatization and silicification (Table 1).

3.4. Shaojiwan

The Shaojiwan Pb–Zn deposit is located in the SE Tianqiao-Liangyan fault-fold tectonic system (Fig. 3). In the Shaojiwan mining area, the exposed lithologies are sedimentary rocks of middle Devonian Longdongshui and Bangzai, late Devonian Dushan and Rongxian, early Carboniferous Jiusi and Shangsi, late Carboniferous Maping, early Permian Liangshan, and middle Permian Qixia-Maokou Formations, and Quaternary sediments (Fig. 11a) (Zhou et al., 2013b). The Longdongshui Formation that mainly consists of sandstone, limestone and dolostone is conformably overlain by the Bangzai Formation, which is in turn conformably overlain by the Dushan Formation. The lithologies of the Bangzai, Dushan, Rongxian, Jiusi, Shangsi, Maping, Liangshan and Qixia-Maokou Formations are similar to those in the Maozhachang, Tianqiao and Banbanqiao mining areas, and the sequence stratigraphic relationships of the Dushan, Rongxian, Jiusi, Shangsi, Maping, Liangshan and Qixia-Maokou Formations please refer the description above (Section 2.2; Fig. 4).

The NW- and NE-trending faults are developed in the Shaojiwan mining area (Fig. 11a). These NW-trending faults comprise a series of high angle reverse faults and form an imbricate thrust nappe structure in the Mangdong-Shaojiwan region (Zhou et al., 2013b). The Shaojiwan deposit occurs in the southeastern part of the asymmetrical Mangdong-Shaojiwan anticline, which trends 310°, with axial plane dipping to the SW (Fig. 11a). These NW-tending reverse faults and anticline belong to the Tianqiao-Liangyan fault-fold tectonic system that is attached to the regional Kangding-Yiliang-Ziyun deep fault (KYZ in Fig. 2a) and strictly control the occurrence of Pb–Zn ore in the Mangdong-Shaojiwan region (Fig. 11a).

Sulfide ore in the Shaojiwan deposit occurs as steeply dipping veins and gently dipping stratiform shape (Fig. 11b). Three ore bodies have been delineated, of which No. I ore body occurs as steeply dipping veins in regional fault zone, and trend extends 360 m long and dip extends 300 m. Above the water table, oxidized ore is dominant, whereas brecciated and massive sulfide ores occur below. The Pb + Zn metal reserves of this ore body exceed 0.4 Mt with grades of Pb 0.71–10.6 wt % (av. 3.37 wt%), Zn 2.09–30.3 wt% (av. 11.7 wt%) and Ag 6.6–70.5 g/t (Zhou et al., 2013b). Sulfide ore mainly consists of sphalerite, galena, pyrite, dolomite and calcite (Fig. 12a–j), with rare quartz and clay minerals (Jin, 2008; Zhou et al., 2013b), which form either massive, banded, disseminated or veined structure (Fig. 12a–f), with granular, fractured, filled, enclosed, metasomatic and eutectic textures (Fig. 12j). Wall rock alteration in the Shaojiwan deposit is similar to that of the Banbanqiao deposit, including dolomization, calcilization, Fe-Mn carbonatization and silicification (Table 1). Details of ore deposit geology are available in Zhou et al. (2013b).
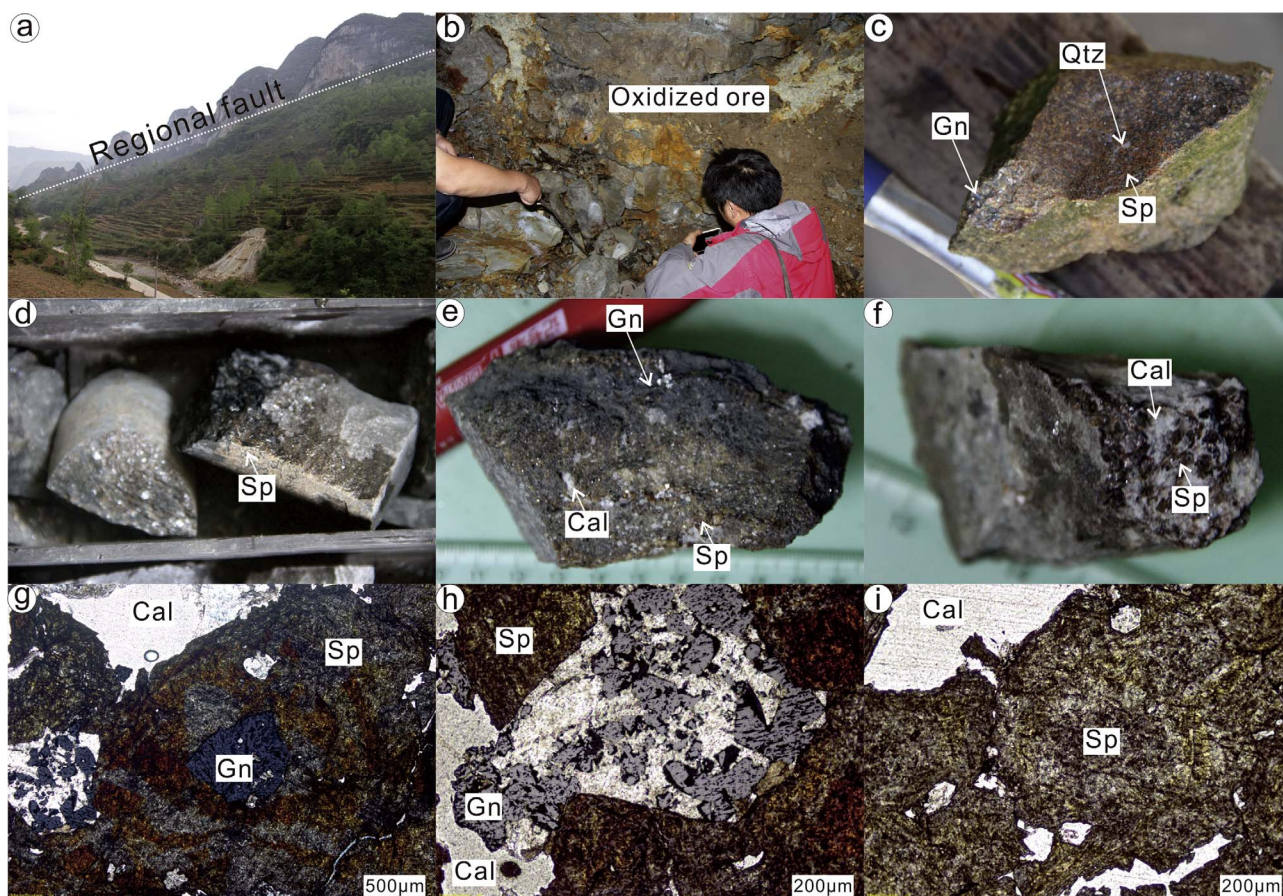
Fig. 10. Photographs of field, hand specimens and microscope; (a) the NEE-trending Maozhachang-Banbanqiao regional fault; (b) oxidized ore; (c) dense disseminated sulfide ore, sphalerite and galena occur as aggregation shapes, quartz fragments fill the fractures of them; (d) dense disseminated sulfide ore; (e) dense disseminated sulfide ore, sphalerite and galena form aggregations, calcite fragments fill the fractures of them; (f) disseminated sulfide ore, sphalerite and galena present in aggregation types and are cemented by calcite; (g) granular galena and calcite are enclosed by sphalerite that displays zones of color; (h) calcite encloses galena and fills the fractures of sphalerite, which shows color's zones; (i) calcite fills the fractures of sphalerite that exhibits color zoning. Sp = sphalerite; Py = pyrite; Gn = galena; Dol = dolomite; Cal = calcite; Qtz = quartz.

3.5. Qingshan

The Qingshan Pb–Zn deposit is located in the NW Qingshan-Shanshulin fault-fold tectonic system (Fig. 3). In the Qingshan mining area, the exposed rocks are sedimentary rocks of late Carboniferous Huanglong and Maping, early Permian Liangshan and middle Permian Qixia-Maokou Formations, and clay layers of Quaternary (Fig. 13a). The lithologies and sequence stratigraphic relationships of the Huanglong, Maping, Liangshan and Qixia-Maokou Formations are similar to those in other mining areas described above. In addition, mafic dike (diabase) related to the ELIP has spatially association with sulfide ore in the Qingshan mining area (Fig. 13a and b).

There are three important faults in the Qingshan ore district, namely the NW-trending F_1, NNW-trending F_{28} and the NNE-trending F_{26} faults (Figs. 13a and 14a). Among these faults, the F_1 belongs to the NW-trending Qingshan-Shanshulin fault-fold tectonic system (Fig. 3) and is an important ore-controlling structure (Fig. 13b).

Three major ore bodies have been found in the Qingshan deposit, of which No. I ore body dip extends 145 m, 70 m long and 1.3–32 m wide, with mean grades of 9.92 wt% Pb and 37.58 wt% Zn; No. II ore body dip extends 45 m, trend extends 42 m and 0.9–6.3 m in width with average grades of 9.22 wt% Pb and 35.12 wt% Zn; and No. III ore body is 40 m in depth, 30 m in length, and 0.5–3.6 m in width, and has mean grades of 3.76 wt% Pb and 34.96 wt% Zn (Zhou et al., 2013c). Ore minerals are mainly galena, sphalerite and pyrite (Fig. 14b–d, h), with few chalcopyrite and arsenopyrite; gangue minerals are dominantly dolomite and calcite (Fig. 14b–d, h), with a small number of barite and quartz (Zhou et al., 2013c). Sulfide ore has massive, veined, net vein, banded, and disseminated structures (Fig. 14b and c, h), with sub-hedral-euhedral granular, enclosed, metasomatic and eutectic textures (Fig. 14d) (Zhou et al., 2013c). Wall rock alteration in the Qingshan deposit is relatively complex and includes dolomization, calcilization, baratization, fluoritization, silicification and chloritization (Table 1).

3.6. Shanshulin

The Shanshulin Pb–Zn deposit is geographically located southeast near to the Qingshan deposit and is structurally controlled by the Qingshan-Shanshulin fault-fold tectonic system (Fig. 3). In the Shanshulin mining area, the exposed strata are late Carboniferous Huanglong, middle Permian Qixia-Maokou, late Permian Emeishan basalts, and late Permian Longtan Formations, as well as early to middle Triassic (Fig. 15a). The lithologies and sequence stratigraphic relationships of these strata please refer the description above (Section 2.2; Fig. 4).

There are three main faults and two folds in the Shanshulin mining area (Fig. 15a). The NW-trending Qingshan-Shanshulin fault-fold tectonic system consists of many high angle reverse faults (such as F_1 in Fig. 15a) with dipping angles of 50°–80°, of which the reverse faults (such as F_9 in Fig. 15a) in the Shanshulin deposit have dipping angles of 55°–75°. The F_3 and F_5 are normal fault (Fig. 15a). The Carboniferous and Permian rocks form the Guanyinshan anticline, and the Permian and Triassic rocks form the Guanyinshan syncline (Fig. 15a).

Sulfide ore in the Shanshulin deposit mainly occurs as steeply-dipping veins along reverse fault dip planes (Fig. 15b), and few stratiform or lentiform shape within the Huanglong Formation carbonate rocks.
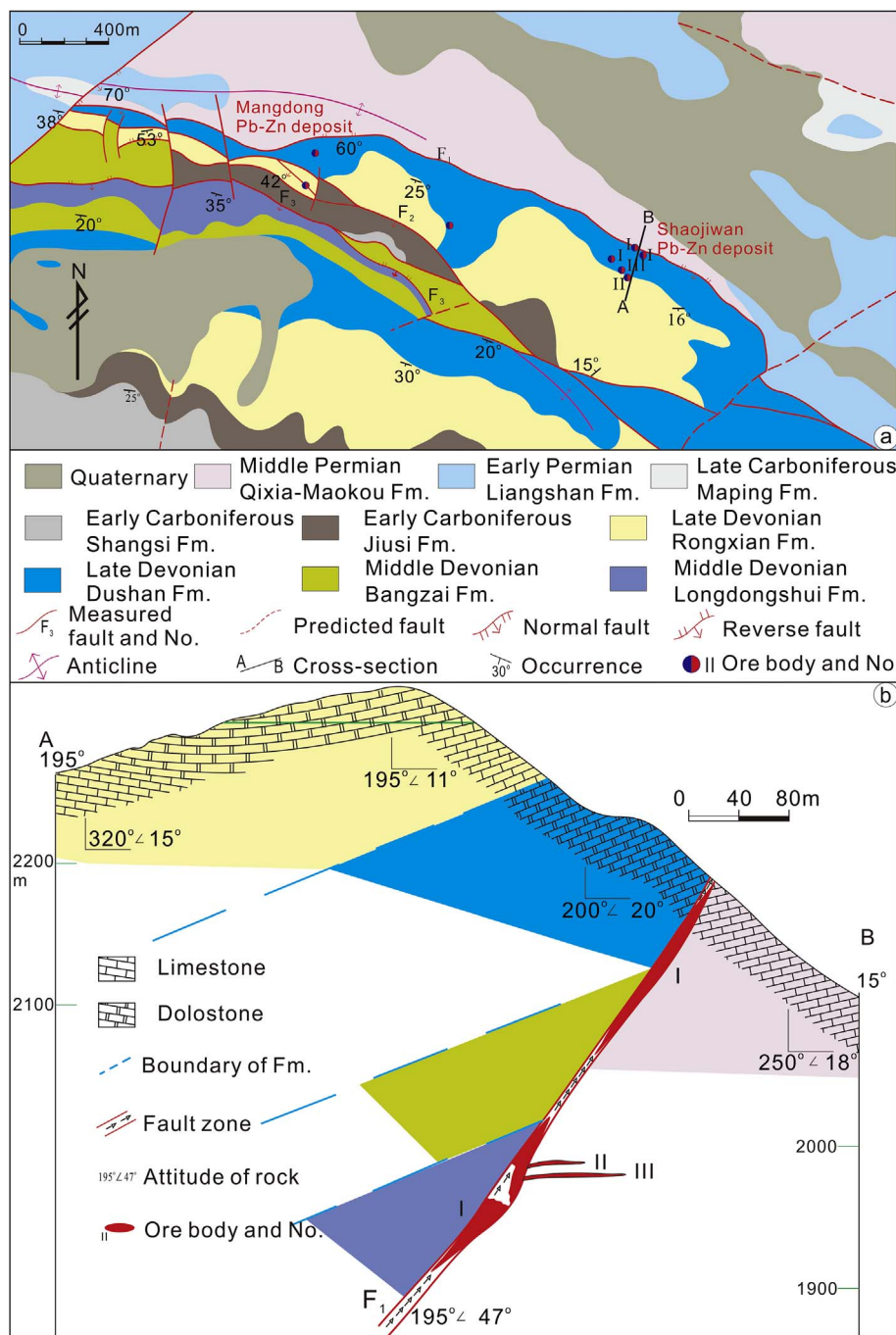
Fig. 11. (a) Geological sketch map of the Mangdong-Shaojiwan Pb–Zn deposits (modified from Jin, 2008; Zhou et al., 2013b); (b) A–B cross-section map (modified from Jin, 2008; Zhang et al., 2011; Zhou et al., 2013b).

Twenty-two ore bodies have been found in the mining area, of which No. IV ore body is the largest one and occurs as veined or lentiform shape along F₉ reverse fault (Fig. 15b). This ore body trend extends 460 m and dip extends 200 m, with a mean thickness of 5.2 m. It contains at least 2 Mt of sulfide ore with grades of 0.24–7.94 wt% Pb (av. 3.64 wt%) and 1.09–26.64 wt% Zn (av. 14.98 wt%). Sulfide ore mainly consists of galena, sphalerite and pyrite (with a small number of chalcopyrite and arsenopyrite) as ore minerals, and dolomite and calcite as gangue minerals (with few barite and quartz) (Fig. 16a–i). Ore minerals form either massive, fine-veined, disseminated or banded sulfide ore (Fig. 16a–f), with anhedral-euhedral granular, filled, enclosed, metasomatic, eutectic and replacement textures (Fig. 16g–i) (Zhou et al., 2014b). There are three generations of sphalerite according to their different crystal habits, colors and mineral assemblages (Zhou et al., 2014b). Wall rock alteration in the Shanshulin deposit is simple and

includes dolomization, calcilization, baratization, and silicification (Table 1).

3.7. Nayongzhi

The Nayongzhi deposit is situated in the eastern part of the NW Guizhou district and the central Wuzhishan anticline (Figs. 3 and 17a). In the Wuzhishan anticline area, the exposed lithologies are sedimentary rocks of late Ediacaran, Cambrian, early Carboniferous, early Permian and early Triassic (Fig. 17a). The late Ediacaran Dengying Formation that consists mainly of limestone and dolostone are unconformably overlain by siltstone and shale of early Cambrian Jindingshan Formation, which are conformably overlain by early Cambrian Qingxudong Formation that comprises mainly limestone and dolostone. Carbonate rocks of the Qingxudong Formation are

Table 1
A brief geological feature of Pb–Zn deposits in the NW Guizhou district, southeastern part of the Upper Yangtze Pb–Zn metallogenic province, SW China.

No.	Name	Tonnage	Ore-hosting strata and rocks	Ore-controlling structures	Ore bodies' shapes	Occurrences	Ore minerals	Gangue minerals	Ore grades	Textures	Structures	Wall rock alteration	References
1	YCP	> 0.3 Mt Ag–Pb–Zn	Late Carboniferous Huanglong Fm., dolostone	NNE regional Yinchangpo-Yunluhe fault and fold bedding plane structures	Stratiform, lentiform and veined shapes	Trends NNE, SEE-dipping, with dip angles of 40°–48°	Galena, sphalerite and pyrite, with rare native Ag, chalcopyrite, cinnabarite, tetrahedrite, bournonite, freibergite, acanthite and polybasite	Dolomite and calcite, with rare quartz and clay minerals	No. I ore body has Pb + Zn 9.1 wt%, Ag 310 g/t; No. II ore body contains Pb + Zn 7.5 wt%, Ag 225 g/t; No. III ore body has Pb + Zn 12 wt%, Ag 273 g/t; and No. IV ore body contains Pb + Zn 8.3 wt%, Ag 235 g/t	Anhedral-euhedral granular, enclosed, eutectic, replacement, recrystallized and stress deformation textures	Massive, veined, disseminated, fractured, and colloidal structures	Dolomization, calcitization, Fe/Mn carbonatization and silicification	Hu (1999)
2	YLH	> 0.2 Mt Zn–Pb–Ag	Late Devonian Wangchengpo Fm., fine- to coarse-grained dolostone and argillaceous dolostone	NNE regional Yinchangpo-Yunluhe fault and its secondary pinniform faults, fracture zones and their intersection parts	Clintheriform, stratiform and lentiform shapes	Ore body trends SE and SW, dipping 25°–50°	Sphalerite, galena and pyrite, with rare chalcopyrite	Dolomite and calcite, with rare quartz and clay minerals	Zn 6.5–35.92 wt%, Pb 9.33–10.80 wt%, Ag 45.12–372 g/t	Granular, enclosed, eutectic, replacement, colloidal, metasomatic, and stress deformation textures	Massive, veined, veinlets cements brecciated and disseminated structes	Dolomization, calcitization, Fe/Mn carbonatization and silicification	Jin et al. (2016a)
3	MZC	> 0.3 Mt Zn–Pb; oxidized and placer ores are in shallow part, and newly-discovered sulfide ore is in deep part	Carboniferous carbonate rocks and Quaternary clay layers	NEE-trending Maozhachang-Banbanqiao fault, and NW- and NS-trending tectonic intersection parts	Oxidized and placer ores occur in veined, scrotiform, lentiform and planar, shapes; Sulfide ore occurs in stratiform and lentiform shapes	No. I ore body trends NE 32°–55°, dipping SE; No. II ore body trends NE65°, dipping SE 62°	Oxidized and placer ores are composed of smithsonite, cerusite, and limonite, with rare anglesite and hemimorphite; Sulfide ore consists mainly of sphalerite, galena and pyrite	Dolomite and calcite, with rare barite	Oxidized No. I ore body has mean Pb 0.77 wt%, Zn 6.27 wt%; and No. II ore body has mean Pb 0.83 wt%, Zn 9.18 wt%. Sulfide ore, averaging Pb 0.63–1.23 wt%, Zn 11.69–12.71 wt%	Sulfide ore has granular, eutectic, and stress deformation textures	Oxidized and placer ores have earthy, crusty, aciniform and faviform structures; sulfide ore has massive, veined and disseminated structures	Dolomization, calcitization, Fe/Mn carbonatization and baratization	Jin (2008)
4	TQ	> 0.38 Mt Zn–Pb	Late Carboniferous Huanglong Fm., and early Carboniferous Baizuo Fm., dolostone	NW-trending Tianqiao-Liangyan fault, Tiqiao anticline, NE-trending Maozhachang-Tianqiao fault	Stratiform, clintheriform, lentiform and scrotiform shapes	Trends SWW (250°–270°) along the formation strike, dipping 15°–30°	Sphalerite, galena and pyrite, with rare chalcopyrite	Dolomite and calcite, with rare quartz, barite, fluorite and clay minerals	No. II$_1$ ore body Pb 1.23 wt%, Zn 5.60 wt%; No. II$_6$ ore body Pb 5.51 wt%, Zn 15.00 wt%; and No.II$_7$ ore body Pb 3.60 wt%, Zn 6.52 wt%	Granular, filled, enclosed, replacement, eutectic, and stress deformation textures	Massive, banded, veined and disseminated structures	Dolomization, calcitization, Fe-Mn carbonatization, baratization, silicification and fluoritization	Zhou et al. (2013a), (2014a)
5	BBQ	> 0.2 Mt Zn–Pb	Early carboniferous Shangsi Fm., carbonate rocks	NEE-trending Maozhachang-Banbanqiao fault, NW-trending reverse fault and NNE-trending Banbanqiao anticline	Stratiform, lentiform and veined shapes	Trends NNW (330°–360°) along the formation strike, dipping 3°–10°	Mainly sphalerite, galena and pyrite	Mainly dolomite, calcite and quartz	Pb 0.26–10.32 wt% and Zn 0.81–28.8 wt%	Anhedral to euhedral granular, metasomatic, filled, enclosed and stress deformation textures	Massive, disseminated, cement breccia veined and banded structures	Dolomization, calcitization, Fe-Mn carbonatization and silicification	Zhou et al. (2014a), Li et al. (2015)
6	MD	> 0.2 Mt Zn–Pb	Middle Permian Qixia-Maokou Fm., and middle-	NW-trending Tianqiao-Liangyan fault	Stratiform, lentiform and	NW-trending along Yunluhe-	Mainly sphalerite, galena and pyrite	Mainly dolomite and calcite	Pb 0.5–10.1 wt% (mean 4.25 wt%) and Zn	Granular, filled, enclosed, metasomatic	Massive, cement breccia veined	Dolomization, calcitization, and	Xiang et al. (2015)

(continued on next page)

Table 1 (continued)

| No.	Name	Tonnage	Ore-hosting strata and rocks	Ore-controlling structures	Ore bodies' shapes	Occurrences	Ore minerals	Gangue minerals	Ore grades	Textures	Structures	Wall rock alteration	References
			late Devonian carbonate rocks	and Mangdong-Shaojiwan nappe structure	steeply dipping veined shapes	Liangyan fault, dipping SE 45°–65°			1.09–25.72 wt% (mean 10.86 wt%)	and eutectic textures	and disseminated structures	Fe-Mn carbonatization	
7	SJW	> 0.3 Mt Zn–Pb	Middle Permian Qixia-Maokou Fm., and middle-late Devonian carbonate rocks	NW-trending Tianqiao-Liangyan fault and Mangdong-Shaojiwan nappe structure	Stratiform, lentiform and steeply dipping veined shapes	Trends 285°–290°, dipping SE 50°–70°	Mainly sphalerite, galena and pyrite	Dolomite and calcite, with rare quartz and clay minerals	Pb 0.71–10.6 wt%, average 3.37 wt%; Zn 2.09–30.3 wt%, mean 11.7 wt%; Ag 6.6–70.5 g/t	Granular, fractured, filled, enclosed, metasomatic and eutectic textures	Massive, banded, disseminated and veined structures	Dolomization, calcilization, Fe-Mn carbonatization and silicification	Zhou et al. (2013b)
8	LY	> 0.2 Mt Zn–Pb	Late Carboniferous carbonate rocks	NW-trending Tianqiao-Liangyan fault	Stratiform, lentiform and veined shapes	Strikes NW, dipping SE 45°–60°	Mainly galena, sphalerite and pyrite	Dolomite and calcite, with rare barite and quartz	Pb 1.39–7.89 wt% and Zn 2.02–18.07 wt%	Granular, filled, enclosed, colloidal, metasomatic and eutectic textures	Massive, disseminated and breccia cemented fine vein structures	Dolomization, calcilization, baratization and silicification	Jin (2008)
9	QS	> 0.3 Mt Zn–Pb	Late Carboniferous Maping Fm., carbonate rocks	NW-trending Qingshan-Shanshulin fault	Irregular scrotiform, lentiform and veined shapes	Strikes NE-SW, dipping SE 50°–75°	Galena, sphalerite and pyrite, with rare chalcopyrite and arsenopyrite	Dolomite and calcite, with rare barite, quartz and fluorite	No. I ore body, Pb 9.92 wt%, Zn 37.58 wt%; No. II ore body, Pb 3.76 wt%, Zn 34.96 wt%; and No. III ore body, Pb 9.22 wt%, Zn 35.10 wt%	Subhedral-euhedral granular, enclosed, metasomatic and eutectic textures	Massive, veined, net vein, banded, and disseminated structures	Dolomization, calcilization, baratization, fluoritization, silicification and chloritization	Zhou et al. (2013c)
10	SSL	> 0.4 Mt Zn–Pb	Late Carboniferous Huanglong Fm., carbonate rocks	NW-trending Qingshan-Shanshulin fault, and Guanyinshan anticline	Stratiform, veined, lentiform and scrotiform shapes	Strikes SE, dipping 55°–75°	Galena, sphalerite and pyrite, with rare chalcopyrite and arsenopyrite	Dolomite and calcite, with rare barite and quartz	No. IV ore body, Pb 0.24–7.94 wt% (av. 3.64 wt%), and Zn 1.09–26.64 wt% (av. 14.98 wt%)	Anhedral-euhedral granular, filled, enclosed, metasomatic, eutectic and replacement textures	Massive, fine-veined, disseminated and banded structures	Dolomization, calcilization, baratization, and silicification	Zhou et al. (2014b)
11	NYZ	> 1.5 Mt Zn–Pb	Early Cambrian-late Ediacaran carbonate rocks	NE-regional fault and Wuzhishan anticline	Stratiform, lentiform, and steeply dipping veined shapes	Strikes NE and dip SE with a dipping angle of 8°–20°	Mainly sphalerite, secondary galena and pyrite	Dolomite and calcite, with rare quartz and barite	No. II 0.5–6.63 wt% (av. 4.03 wt%) Zn and 0.04–4.05 wt% (av. 0.45 wt%) Pb	Granular, filled, enclosed, fragmented and replacement textures	Massive, veined, and disseminated structures	Dolomization, calcilization, baratization, and silicification	Jin et al. (2015, 2016b), Chen et al. (2017), Zhou et al. (2018a)
12	GZY	> 0.2 Mt Zn–Pb	Early Carboniferous-middle Devonian carbonate rocks	NNE- and NE-trending regional fault, and fracture zones	Stratiform, lentiform, veined, and scrotiform shapes	Trends along the formation strike	Sphalerite, and galena, with rare pyrite and chalcopyrite	Dolomite and calcite, with rare siderite, quartz, barite and fluorite	Pb 0.56–6.69 wt% and Zn 1.01–14.35 wt%	Granular, enclosed, metasomatic and eutectic textures	Massive, banded, veined and disseminated structures	Dolomization, calcilization, Fe-carbonatization, baratization, silicification and fluoritization	Zeng et al. (2017)

Note: see Figs. 3–19.

293
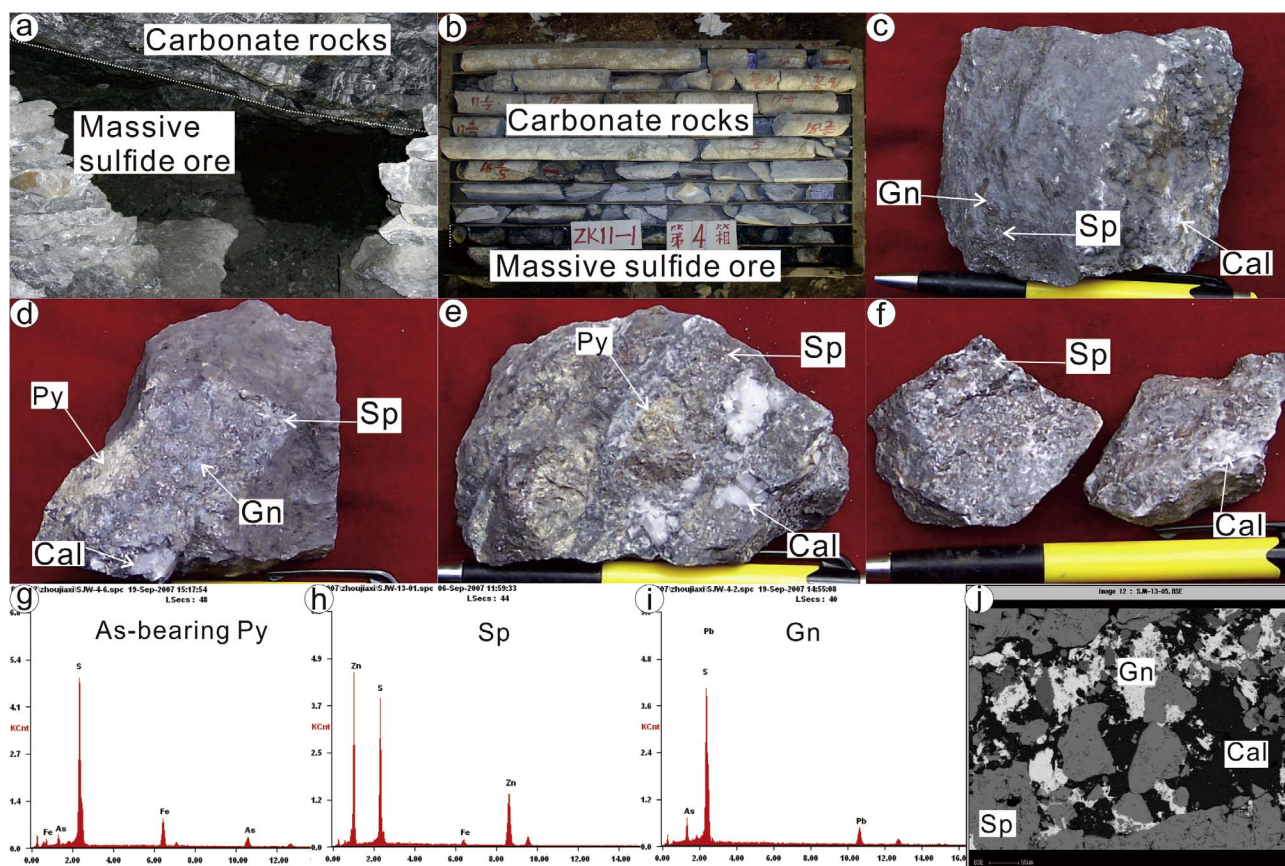
Fig. 12. Photographs of field, hand specimens and microscope; (a) massive sulfide ore and its relationship with carbonate rocks; (b) drill hole reveals the relationship between massive sulfide ore and carbonate rocks; (c) massive sulfide ore, sphalerite and galena occur as aggregation shapes, calcite fragments fill the fractures of them; (d) massive sulfide ore, sphalerite, pyrite and galena occur as aggregation types, calcite fragments fill the fractures of them; (e) massive sulfide ore, sphalerite, and pyrite form aggregations, Cal fragments fill the fractures of them; (f) massive sulfide ore, sphalerite presents as aggregation types, calcite fragments fill the fractures of sphalerite; (g) energy spectrum diagram of As-bearing pyrite; (h) energy spectrum diagram of sphalerite; (i) energy spectrum diagram of galena; (j) granular sphalerite coexists with galena and calcite. Sp = sphalerite; Py = pyrite; Gn = galena; Cal = calcite.

conformably overlain by middle Cambrian Douposi Formation that is composed mainly of dolostone and sandstone, which are in turn conformably overlain by limestone and dolostone of late Cambrian Loushanguan Formation. Early Carboniferous Xiangbai Formation rocks that unconformably overlay on the Loushanguan Formation carbonate rocks are conformably overlain by early Carboniferous Jiusi Formation rocks, which are in turn unconformably overlain by early Permian Liangshan Formation rocks. Sedimentary rocks of the Liangshan Formation are unconformably overlain by early Triassic Daye Formation that mainly consists of limestone (Chen et al., 2015b, 2017; Jin et al., 2015, 2016b; Zhou et al., 2018a). In the Nayongzhi mining area, the exposed rocks are the Qingxudong Formation carbonate rocks (Fig. 17a and b).

In the Wuzhishan anticline area, the structures are well-developed (Figs. 3 and 17a) (Chen et al., 2015b; Jin et al., 2015). The Wuzhishan anticline, a NE-trending asymmetric anticline, is 16 km in length and 4 km in width with an axis trending 45°. The Narun fault (F$_1$ in Fig. 17a) is a normal fault, which strikes the NE, dips to the SE and intersects the NW-trending Shuicheng-Weining regional fault-fold tectonic system (Fig. 3). The Dujiaqiao fault (F$_2$ in Fig. 17a) is a reverse fault that strikes 30° and dips SE with angles of 60°–70°. Another important structure, the F$_7$ reverse fault, trends north with dipping angles of 51°–75°.

In the Nayongzhi deposit, there are at least one steeply-dipping vein and twenty stratiform or lentiform ore bodies (Jin et al., 2016b; Chen et al., 2017; Zhou et al., 2018a). The steeply-dipping vein occurs along the F$_7$ reverse fault zone (Fig. 17b), and is 20–50 m long, 0.5–3 m wide and 200 m thick, with grade of > 10 wt% Zn. There are three groups of stratiform or lentiform ore bodies (Fig. 17b). Among these groups, Group II is the largest one and is hosted by limestone and dolostone

with the same orientation to the host rocks, namely strikes NE and dips SE at angles of 8°–20°. The main ore body in Group II is 2725 m long, 250–775 m wide and 1–29.6 m thick, with 0.5–36.63 wt% Zn (av. 4.03 wt%) and 0.04–4.05 wt% Pb (av. 0.45 wt%). Sulfide ore in the Nayongzhi deposit consists mainly of sphalerite, galena and pyrite, with calcite and dolomite as the primary gangue minerals, and rare quartz and barite as local associated minerals (Fig. 18a–k). Sulfide ore has either veins, massive, or disseminated structure (Fig. 18a–h), with granular, fragmented and replacement textures (Fig. 18i–k). The spatial distribution of sulfide ore shows the formation sequence is from sphalerite-dominated massive/dense disseminated ore, and sphalerite- and galena-dominated massive/sparely disseminated ore, to metasomatic, filled or cemented ore vein. Therefore, sulfide minerals have at least two generations (Jin et al., 2016b; Zhou et al., 2018a). Wall rock alteration includes dolomization, calcilization, silicification and baratization (Table 1). Details of ore deposit geology and mineralogy were described in Zhou et al. (2018a).

3.8. Guanziyao

The Guanziyao Pb–Zn deposit is located in the southern part of the NW Guizhou district (Fig. 3). In the Guanziyao region, the exposed strata are middle-late Devonian, late Devonian-early Carboniferous, late Carboniferous, early-middle Permian, late Permian Emeishan basalts, late Permian Longtan Formation, Triassic and Cretaceous (Fig. 19a) (Zeng et al., 2017). The middle Devonian Bangzai Formation rocks are unconformably overlain by late Devonian Wangchengpo Formation that mainly consists of carbonate rocks and shale, which are unconformably overlain by early Carboniferous Xiangbai Formation
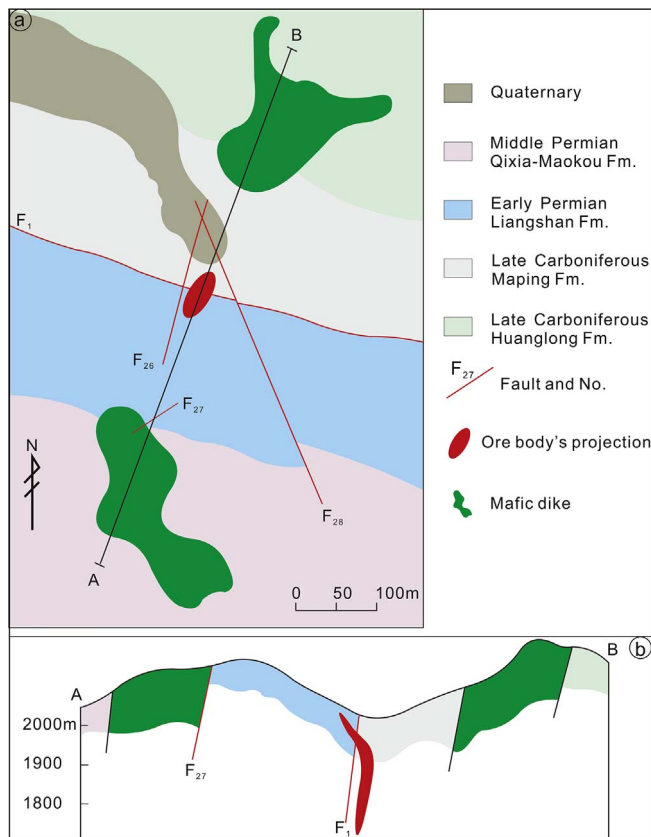
Fig. 13. (a) Geological sketch map of the Qingshan Pb–Zn deposit (modified from Jin, 2008; Zhou et al., 2013c); (b) A–B cross-section map (modified from Jin, 2008; Zhou et al., 2013c).

that mainly comprises shale and carbonate rocks. Late Carboniferous Maping Formation carbonate rocks that unconformably overlay on the Xiangbai Formation sedimentary rocks are conformably overlain by early Permian Liangshan Formation rocks. The lithologies and sequence stratigraphic relationships of the Liangshan, Qixia-Maokou and Emeishan Formations, Triassic and Cretaceous please refer the description above (Section 2.2; Fig. 4). In addition, mafic dikes related to the ELIP have spatially association with sulfide ore in the Guanziyao region (Fig. 19a). In the Guanziyao mining area, the exposed rocks are shale, carbonate rocks of the Bangzai, Wangchengpo, Xiangbai and Maping Formations (Fig. 19a and b).

Structures in the Guanziyao region are developed, including mainly the NNE-, NE- and NW-trending faults and folds (Figs. 3 and 19a). Almost all the faults are reverse fault (Zeng et al., 2017), of which the NNE-trending Guanziyao fault is a regional reverse fault that controlled the distribution of Pb–Zn deposits in this region (Fig. 19a). The Guanziyao deposit occurs in the intersection part of the NNE- and NE-trending faults.

More than twenty-nine Pb–Zn mineralization spots have been found in the Guanziyao region, in which sulfide ore occurs as stratiform, lentiform, veined, and scrotiform shapes within bedding-planes or steeply-dipping veins along fault dip planes (Fig. 19b) (Zeng et al., 2017). Ore minerals are mainly sphalerite and galena, with rare pyrite and chalcopyrite, and gangue minerals are dominantly dolomite and calcite, with rare siderite, quartz, barite and fluorite (Zeng et al., 2017). These minerals form either massive, banded, veined or disseminated ore with granular, enclosed, metasomatic and eutectic textures (Zeng et al., 2017). Sulfide ore body commonly contains 0.56–6.69 wt% Pb and 1.01–14.35 wt% Zn. Wall rock alteration in the Guanziyao region is relatively complex and includes dolomization, calcilization, Fe-carbonatization, baratization, silicification and fluoritization (Table 1).

4. Samples and analytical methods

4.1. Samples

Sulfide ore samples were collected from ore exploration tunnels and drill holes in the Maozhachang and Liangyan deposits (Figs. 3 and 5b). After the mineralogical observation, and analysis under microscope (Figs. 6 and 23) and scanning electron microscope (SEM), pyrite and galena crystals formed at main ore formation phase were selected for in situ NanoSIMS S (Fig. 23) and fs LA-MC-ICPMS Pb isotope analyses, respectively.

4.2. Analytical methods

4.2.1. NanoSIMS in situ S isotope analysis

In situ S isotopes were analyzed using a CAMECA NanoSIMS at the Key Lab of Earth and Planetary Physics, Institute of Geology and Geophysics, Chinese Academy of Sciences (CAS). In order to meet the diverse requirements of spatial resolution, the NanoSIMS was made using 3 different settings of the Faraday cups/electron multiplier (EM) detectors. The bracketing method of standard-sample-standard was used to correct instrumental mass fractionation. International standard included Balmat (pyrite and sphalerite) and CAR-123 (pyrite), and internal standard included PY-1117 (pyrite), CS-01 (pyrite), JC-14 (sphalerite) and MY09-12 (sphalerite). The analytical uncertainty was better than 0.2‰ (1σ). The $\delta^{34}S$ values were reported relative to the Vienna Canyon Diablo Troilite (V-CDT) standard. Details of NanoSIMS instrument parameters, and in situ analysis techniques were described in Zhang et al. (2014b) and Zhou et al. (2018a, 2018b).

4.2.2. Fs LA-MC-ICPMS in situ Pb isotope analysis

In situ Pb isotope analysis was undertaken using a Nu II MC-ICPMS instrument combined with a 266 nm femtosecond (fs) laser ablation system at the State Key Laboratory of Continental Dynamics, Northwest University. Line scan ablation consisted of background collection for 20 s followed by 50 s of laser ablation for signal collection. Laser ablation parameters were: 15 μm spot size; 100% output energy, > 600 μJ; 100% energy density, 6 J/cm²; laser frequency, 5–50 Hz; and ablation way, line 3 μm/s. These ensured a strong enough signal for in situ Pb isotope analysis. The Tl (20 ppb), NIST SRM 997 ($^{205}Tl/^{203}Tl = 2.38890$) and NIST SRM 610 glass served as internal and external standards. The repeated analyses of NIST SRM 610 glass yielded highly reliable and reproducible results that have a mean $^{206}Pb/^{204}Pb = 17.052 \pm 0.003$, $^{207}Pb/^{204}Pb = 15.515 \pm 0.003$ and $^{208}Pb/^{204}Pb = 36.980 \pm 0.007$ (1s, $n = 183$). Details of fs LA-MC-ICPMS instrument parameters and in situ analysis techniques were described in Bao et al. (2016) and Zhou et al. (2018a, 2018b).

5. Carbon and O isotopic compositions

5.1. Variations of C–O isotopic compositions

The statistical C–O isotopic data for syn- and post-ore calcite/dolomite, as well as altered and fresh dolostone/limestone from the chosen Yinchangpo, Yunluhe, Tianqiao, Banbanqiao, Shaojiwan, Qingshan and Shanshulin Pb–Zn deposits (Chen, 1986; Wang, 1996; Mao et al., 1998; Zhang et al., 1998; Hu, 1999; Mao, 2000; Dou and Zhou, 2013; Zhou et al., 2013a, 2013c, 2014b; Li et al., 2015; Jin et al., 2016a) are listed in Appendix Table S1 and are shown in Figs. 20–22.

Syn-ore calcite/dolomite samples have $\delta^{13}C_{PDB}$ and $\delta^{18}O_{SMOW}$ values ranging from −10.1 to +0.7‰ (−2.7‰ on average) and +11.3 to +23.6‰ (+18.1‰ on average), respectively; post-ore calcite/dolomite samples have $\delta^{13}C_{PDB}$ and $\delta^{18}O_{SMOW}$ values in range of −10.9 to +1.1‰ (−2.2‰ on average) and +15.2 to +22.6‰ (+19.7‰ on average), respectively; altered dolostone samples have $\delta^{13}C_{PDB}$ values ranging from −3.0 to +0.9‰ (−1.4‰ on average) and $\delta^{18}O_{SMOW}$
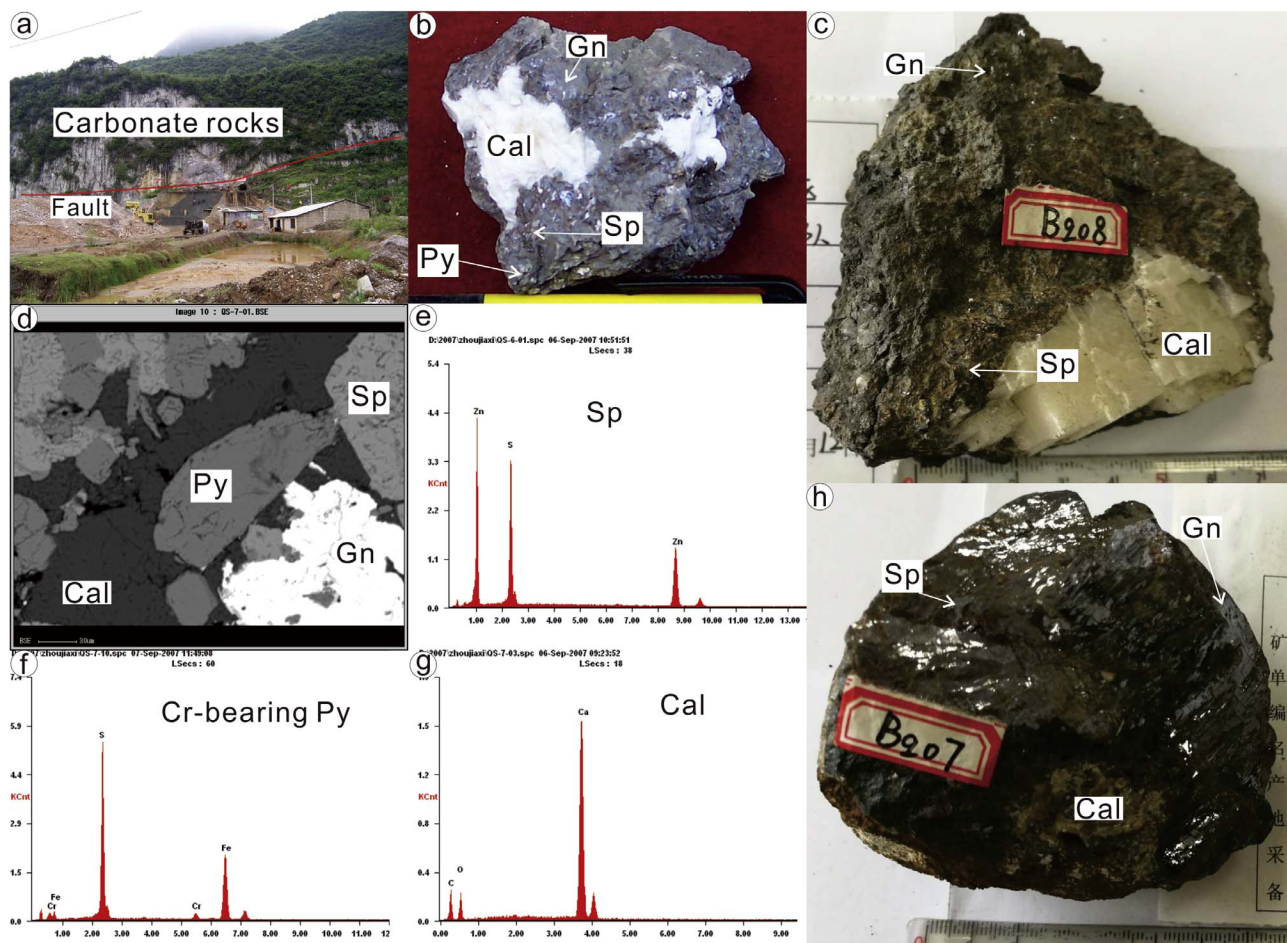
Fig. 14. Photographs of field, hand specimens and microscope; (a) fault within carbonate rocks; (b) massive sulfide ore, sphalerite, pyrite and galena form aggregations, calcite fragments fill the fractures of them; (c) massive sulfide ore, sphalerite and galena occur as aggregation shapes, calcite fragments fill the fractures of them; (d) sphalerite coexists with pyrite and galena, all of which are filled or cemented by calcite; (e) energy spectrum diagram of sphalerite; (f) energy spectrum diagram of Cr-bearing pyrite; (g) energy spectrum diagram of calcite; (h) massive sulfide ore, sphalerite and galena occur as aggregation types, calcite fragments fill the fractures of them. Sp = sphalerite; Py = pyrite; Gn = galena; Cal = calcite.

values of +18.6 to +20.9‰ (+20.2‰ on average); and fresh dolostone/limestone samples have $\delta^{13}C_{PDB}$ and $\delta^{18}O_{SMOW}$ in range of −1.8 to +3.9‰ (+0.9‰ on average) and +21.0 to +26.8‰ (+23.5‰ on average), respectively. From syn- to post-ore and altered, and then to fresh carbonates, both $\delta^{13}C_{PDB}$ and $\delta^{18}O_{SMOW}$ values are gradually increased (Fig. 20a and b). Moreover, C–O isotopic data for syn-ore calcite/dolomite have the following regularities: (i) from the SSW (the Yinchangpo deposit: $\delta^{13}C_{PDB}$ = −3.2 to −0.3‰, −2.0‰ on average; $\delta^{18}O_{SMOW}$ = +11.3 to +18.5‰, +15.5‰ on average) to the NNE (the Yunluhe deposit: $\delta^{13}C_{PDB}$ = −10.1 to +0.7‰, −2.9‰ on average; $\delta^{18}O_{SMOW}$ = +15.2 to +23.6‰, +20.8‰ on average) (Fig. 20a and b), along the Yinchangpo-Yunluhe fault (Fig. 3), both of the $\delta^{13}C_{PDB}$ and $\delta^{18}O_{SMOW}$ values are increased; (ii) from the SWW to the NEE along the Maozhachang-Banbanqiao fault (Fig. 3), the $\delta^{13}C_{PDB}$ values (the Tianqiao deposit: −5.3 to −3.4‰, −4.5‰ on average; the Banbanqiao deposit: −2.8 to −0.7‰, −1.1‰ on average) are increased (Fig. 20a), whereas the $\delta^{18}O_{SMOW}$ values (the Tianqiao deposit: +14.9 to +19.6‰, +17.9‰ on average; the Banbanqiao deposit: +14.1 to +17.0‰, +15.5‰ on average) are decreased (Fig. 20b); (iii) from the NW to the SE (the Shaojiwan deposit: $\delta^{13}C_{PDB}$ = −3.1 to −2.5‰, −2.8‰ on average; $\delta^{18}O_{SMOW}$ = +18.9 to +19.3‰, +19.1‰ on average), along the Tianqiao-Liangyan fault (Fig. 3), the $\delta^{13}C_{PDB}$ values are increased (Fig. 20a) with nearly constant $\delta^{18}O_{SMOW}$ values (Fig. 20b); and (iv) from the NW to the SE, along the Qingshan-Shanshulin fault (Fig. 3), the $\delta^{13}C_{PDB}$ values are increased (the Qingshan deposit: −5.0 to −3.4‰, −4.0‰ on average; the Shanshulin deposit: −3.1 to −1.4‰, −1.9‰ on average) (Fig. 20a), whereas the

$\delta^{18}O_{SMOW}$ values (the Qingshan deposit: +18.9 to +19.6‰, +19.2‰ on average; the Shanshulin deposit: +18.8 to +20.3‰, +19.5‰ on average) are also nearly constant (Fig. 20b).

5.2. Sources of C and O, and evolution of hydrothermal systems

As calcite and dolomite are two main carbonate minerals in Pb-Zn sulfide ores (Zhou et al., 2013a, 2014b; Jin et al., 2016b; Liu et al., 2017), so HCO_3^- or H_2CO_3 (occurring as liquid phase of CO_2) is the dominant C species in hydrothermal systems. Hence, $\delta^{13}C_{CO2} \approx \delta^{13}C_{fluid}$ if the fractionation of C isotopes between HCO_3^-/H_2CO_3 (liquid) and CO_2 (gas) is negligible (Ohmoto, 1972; Zheng, 1990; Zheng and Hoefs 1993; Hoefs, 2009; Zhou et al., 2018a). The $\delta^{13}C_{CO2}$ values can be calculated using the equation of 1000 lnα $_{(CO2-Calcite)} \approx \delta^{13}C_{CO2} - \delta^{13}C_{Calcite}$ = −2.4612 + 7.663 × 10³/(T + 273.15) − 2.988 × 10⁶/(T + 273.15)² (Bottinga, 1968) ("T" [200 °C] is an average metallogenic temperature; Jin, 2008; Zhou et al., 2013d; Zhu et al., 2016a; Liu et al., 2017). Similarly, the $\delta^{18}O_{H2O}$ values can be calculated using the equation of 1000 lnα $_{(Calcite-H2O)} \approx \delta^{18}O_{Calcite} - \delta^{18}O_{H2O}$ = 2.78 × 10⁶/(T + 273.15)² −3.39 (O'Neil et al., 1969). The theoretical $\delta^{13}C_{fluid}$ and $\delta^{18}O_{fluid}$ values (based on the $\delta^{13}C$ and $\delta^{18}O$ values of syn-ore calcite/dolomite) are of −9.7 to +0.7‰ (−2.4‰ on average) and +2.3 to +14.6‰ (+9.0‰ on average), respectively (Appendix Table S1).

It has been well-documented that C–O isotopic compositions of various reservoirs are distinct (Fig. 21), for example, the $\delta^{13}C$ and $\delta^{18}O$ values of mantle are −8 to −4‰ and +6 to +10‰, respectively
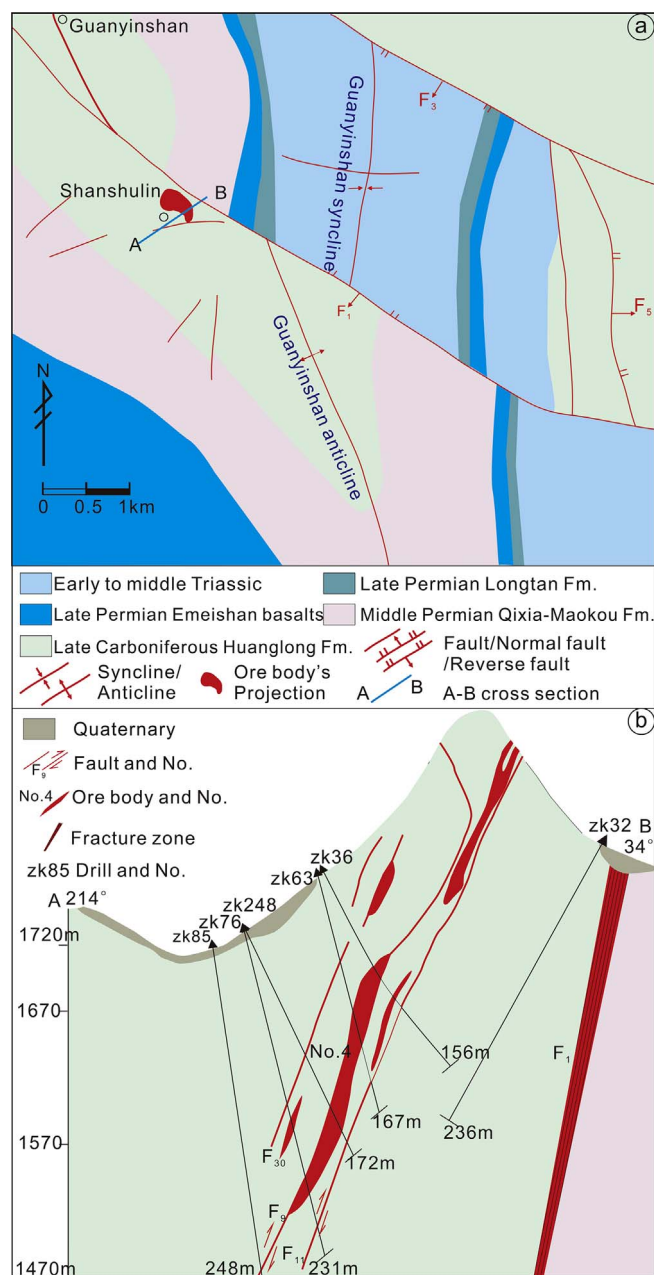
Fig. 15. (a) Geological sketch map of the Shanshulin Pb–Zn deposit (modified from Jin, 2008; Zhou et al., 2014b); (b) A–B cross-section map (modified from Jin, 2008; Zhou et al., 2014b).

(Taylor et al., 1967; Demény et al., 1998), typical marine carbonate rocks have $\delta^{13}C$ values of -4 to $+4$‰ and $\delta^{18}O$ values of $+20$ to $+30$‰ (Veizer and Hoefs, 1976), whereas the $\delta^{13}C$ and $\delta^{18}O$ values of sedimentary organic matters mainly range from -30 to -15‰ and $+24$ to $+30$‰, respectively (Kump and Arthur, 1999; Hoefs, 2009). Thus, the C–O isotopes of syn-ore calcite/dolomite can provide a crucial constraint on the sources and evolution of hydrothermal systems.

The C–O isotopes of syn-ore calcites/dolomites and associated fluids ($\delta^{13}C_{fluid} = -9.7$ to $+0.7$‰, -2.4‰ on average; $\delta^{18}O_{fluid} = +2.3$ to $+14.6$‰, $+9.0$‰ on average) can't match with anyone of the above-mentioned three main reservoirs (Fig. 21), suggesting that neither mantle, carbonates nor organic matters provided C–O to the hydrothermal systems solely.

The mantle-derived Emeishan flood basalts and mafic dikes are spatially associated with Pb–Zn deposits in the NW Guizhou district (Figs. 2b and 3), indicating that mantle has the possibility to provide

volatiles (including H_2S, CO_2 and H_2O) to the hydrothermal systems (Pirajno, 2000; Huang et al., 2004; Davidheiser-Kroll et al., 2014; Xu et al., 2014; Zhou et al., 2018b). This is also supported by H–O isotopes (Huang et al., 2004) and S isotopes (Figs. 24, 25 and 27). Additionally, the $\delta^{18}O$ values of syn-ore calcites/dolomites and associated fluids are similar to those of metamorphic rocks/fluids ($\delta^{18}O = +2$ to $+25$‰: Hoefs, 2009) (Fig. 20b), implying that metamorphic fluids were also likely involved in ore formation (Zhou et al., 2013a). Furthermore, the evidence from Zn and Pb–Sr isotopes suggest that ore-forming metals and associated fluids were most likely derived from, flowed through or interacted with multiple reservoirs involving mantle-derived rocks of the ELIP, ore-bearing sedimentary rocks and underlying basement metamorphic rocks (see below; Figs. 27–34). Hence, it is most likely that such C–O isotope signatures (Figs. 20a–b and 21) were mainly generated by water/rock (W/R) interaction between mixed (mantle and metamorphic) fluids and carbonate rocks, and were affected by dehydroxylation of organic matters within sedimentary strata in local (Fig. 21). On the other hand, the simulated C–O isotopic evolution curves of syn-ore calcite/dolomite that were precipitated through the W/R interaction between hydrothermal fluids (initial $\delta^{13}C_{fluid} = -2$‰, $\delta^{18}O_{fluid} = +9$‰) and limestone (Fig. 22) (O'Neil et al., 1969; Zheng and Hoefs, 1993), indicating that the evolution curves of H_2CO_3 (Fig. 22) as the dominant C species can generate our C–O isotope signatures (Zheng and Hoefs, 1993). Such an initial C–O isotopic composition of hydrothermal fluids is exactly similar to the average theoretical $\delta^{13}C_{fluid}$ (-2.4‰) and $\delta^{18}O_{fluid}$ ($+9$‰) values. This means that the W/R interaction plays a crucial role during the precipitation of hydrothermal carbonate minerals (Zhou et al., 2018a). In addition, the corresponding simulated temperatures are between 300 and 150 °C (Fig. 22), which are consistent with the homogenization temperatures of fluid inclusions (280–120 °C) (Jin, 2008; Zhou et al., 2013d; Zhu et al., 2016a; Liu et al., 2017).

The gradually increased C–O isotopes from syn-/post-ore calcite/dolomite to altered dolostone, and then to fresh carbonate rocks (Fig. 20a and b), showing that the degree of W/R interaction is gradually decreased, namely the contribution from carbonate rocks is gradually dominant. Hence, the variations of C–O isotopic compositions can trace the migration paths or evolution of hydrothermal systems. The spatial regularities of C–O isotopic data for syn-ore calcite/dolomite (Fig. 20a and b), revealing that the hydrothermal systems were likely migrated or evolved from west to east, i.e. from Yinchangpo to Yunluhe, Tianqiao to Banbanqiao/Shaojiwan, and Qingshan to Shanshulin in the NW Guizhou district (Fig. 3).

6. Sulfur isotopic compositions

6.1. Variations of S isotopic compositions

NanoSIMS in situ S isotopic data for pyrite crystals from the Maozhachang and Liangyan deposits, and previously reported bulk S isotopic data for pyrite, sphalerite, galena and barite from the Yinchangpo, Yunluhe, Maozhachang, Tianqiao, Banbanqiao, Yadu, Mangdong, Shaojiwan, Qingshan, Shanshulin and Nayongzhi deposits (Chen, 1986; Zhang et al., 1998, 2011, 2016; Hu, 1999; Liu and Lin, 1999; Fu, 2004; Gu, 2007; Jin, 2008; Zhou et al., 2013d, 2014a, 2014b; Li et al., 2015; Xiang et al., 2015; Jin et al., 2016b; Chen et al., 2017; Liu et al., 2017) are listed in Appendix Table S2 and are shown in Figs. 23–27.

In situ $\delta^{34}S_{CDT}$ values of pyrite crystals from the Maozhachang and Liangyan Pb–Zn deposits range from $+3.0$ to $+15.1$‰ ($+11.3$‰ on average) and -12.6 to -4.7‰ (-7.9‰ on average), respectively (Fig. 23). Compared with previously reported bulk $\delta^{34}S_{CDT}$ value of pyrite ($+14.0$‰; Jin, 2008) from the Maozhachang deposit, in situ $\delta^{34}S_{CDT}$ values have a much larger range. In addition, pyrite crystals from the Liangyan deposit have lower $\delta^{34}S_{CDT}$ values than other deposits with the exception of pyrite (-18.1‰) from the Yunluhe deposit (Fig. 24).
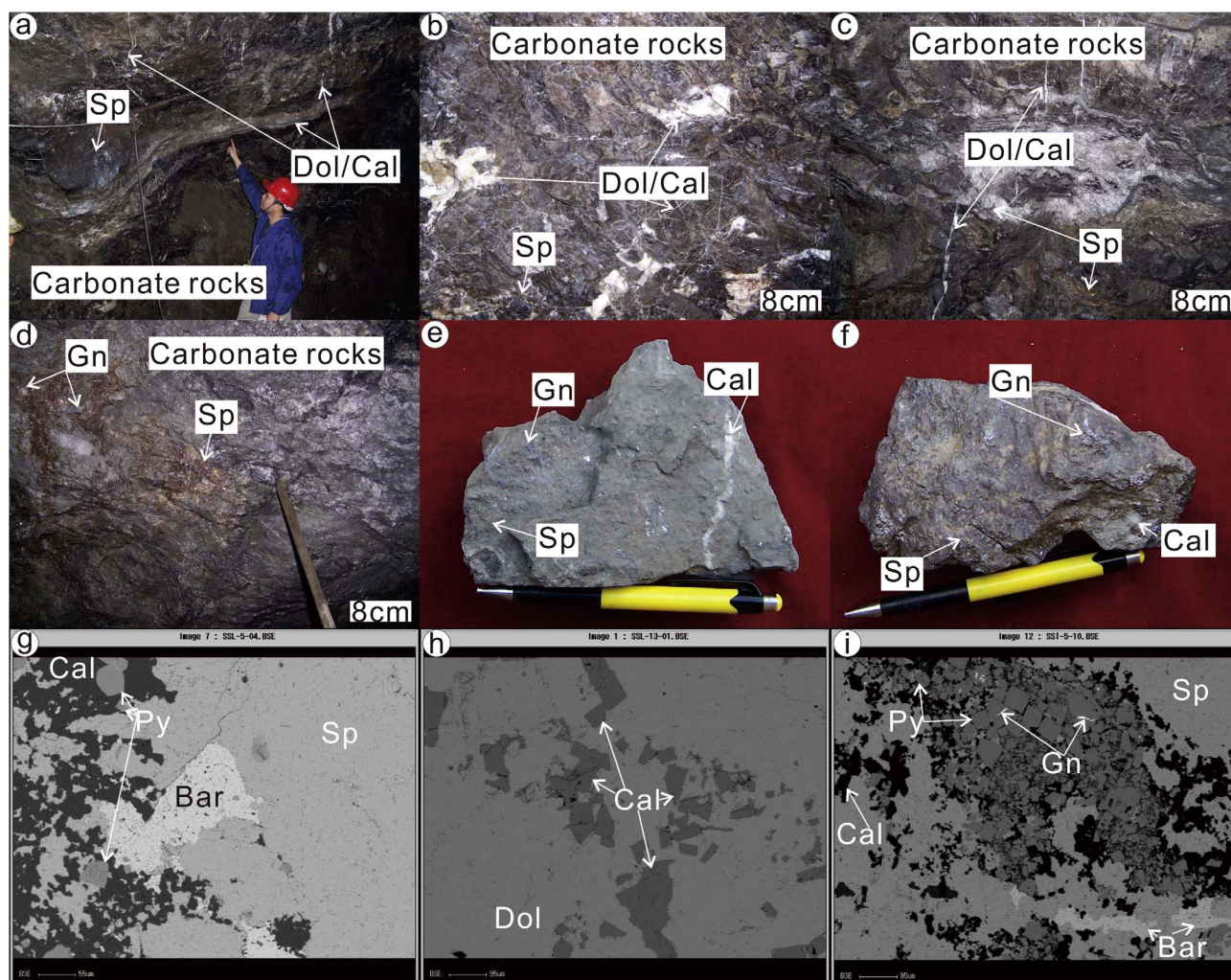
Fig. 16. Photographs of field, hand specimens and microscope; (a) massive sphalerite, and dolomite/calcite veins and veinlets within carbonate rocks; (b)–(c) massive sphalerite, and dolomite/calcite fragments and veinlets within carbonate rocks; (d) massive sphalerite and galena within carbonate rocks; (e) massive sulfide ore, sphalerite and galena display massive aggregate structures and calcite occurs an veinlets; (f) massive sulfide ore, sphalerite and galena occur in aggregation shapes and calcite fragments fill the fractures of them; (g) barite and calcite fill the fractures of sphalerite, and calcite encloses pyrite; (h) Cal fragments are enclosed by dolomite; (i) pyrite fragments, and barite and calcite veinlets fill the fractures of sphalerite. Sp = sphalerite; Py = pyrite; Gn = galena; Dol = dolomite; Cal = calcite; Bar = barite.

Bulk $\delta^{34}S$ values of pyrite, sphalerite and galena from the chosen Pb–Zn deposits range from -18.1 to $+25.5‰$ ($+13.5‰$ on average) (Appendix Table S2). The spatial regularities of S isotopic compositions of these deposits are (i) from the SSW to the NNE along the Yinchangpo-Yunluhe fault (Fig. 3), the $\delta^{34}S$ values (the Yinchangpo deposit: $\delta^{34}S = +7.6$ to $+14.2‰$, $+11.1‰$ on average; the Yunluhe deposit: $\delta^{34}S = -18.1$ to $+2.7‰$, $-2.1‰$ on average) are decreased (Figs. 24 and 25); (ii) from the SWW (the Tianqiao deposit: $\delta^{34}S = +8.3$ to $+15.9‰$, $+12.4‰$ on average) to the NEE (the Banbanqiao deposit: $\delta^{34}S = +3.2$ to $+9.8‰$, $+6.4‰$ on average) (Figs. 24 and 25) along the Maozhachang-Banbanqiao fault (Fig. 3), the $\delta^{34}S$ values are decreased; (iii) along the Tianqiao-Liangyan fault (Fig. 3), the $\delta^{34}S$ values of sulfides and associated fluids are similar to those of the Tianqiao ($\delta^{34}S_{fluid} = +14.5‰$), Yadu ($\delta^{34}S = +8.8$ to $+13.7‰$, $+11.5‰$ on average, $\delta^{34}S_{fluid} = +14.3‰$), Mangdong ($\delta^{34}S = +10.7$ to $+13.7‰$, $+12.2‰$ on average), and Shaojiwan ($\delta^{34}S = +8.4$ to $+11.6‰$, $+10.5‰$ on average) deposits (Figs. 24–26); and (iv) from the NW to the SE along the Qingshan-Shanshulin fault (Fig. 3), the $\delta^{34}S$ values of sulfides and associated fluids (the Qingshan deposit: $\delta^{34}S = +10.7$ to $+19.6‰$, $+15.7‰$ on average, $\delta^{34}S_{fluid} = +15.7‰$; the Shanshulin deposit: $\delta^{34}S = +13.4$ to $+20.3‰$, $+16.8‰$ on average, $\delta^{34}S_{fluid} = +19.0‰$; the Nayongzhi deposit: $\delta^{34}S = +4.7$ to $+25.5‰$, $+19.9‰$ on average) are gradually increased (Figs. 24–26).

6.2. Sources of S, reduced mechanisms, and evolution of hydrothermal systems

Mineralogically, sulfide ores in the NW Guizhou district mainly consist of pyrite, sphalerite, galena and hydrothermal carbonate minerals, as well as quartz and fluorite, with rare barite locally (Figs. 6, 8, 10, 12, 16 and 18). The absence of sulfate minerals in sulfide ores indicates that $\delta^{34}S_{sulfide}$ values, especially $\delta^{34}S_{pyrite} \approx \delta^{34}S_{fluid}$ (Ohmoto, 1972; Seal, 2006; Hoefs, 2009). $\delta^{34}S$ values of sulfides determined by conventional bulk and NanoSIMS in situ techniques range from -18.1 to $+25.5‰$ (Figs. 23–27), reflecting both light and heavy S isotopes are enriched in the hydrothermal systems. Such S isotopic data overlap with mantle-derived S ($\delta^{34}S = -3$ to $+3‰$: Chaussidon et al., 1989), metamorphic rocks/fluids ($\delta^{34}S = -20$ to $+20‰$: Seal et al., 2000), sulfate-bearing (barite) evaporites ($\delta^{34}S = +11.8$ to $+28.3‰$; Jin, 2008; Zhou et al., 2013a, 2013d, 2018a; Liu et al., 2017) and H_2S in oil and gas reservoir ($\delta^{34}S = +5$ to $+20‰$: Zhu et al., 2014), as well as the Cambrian ($\delta^{34}S = +26$ to $+32‰$), Devonian ($\delta^{34}S = +16$ to $+26‰$), Carboniferous ($\delta^{34}S = +13$ to $+23‰$) and Permian ($\delta^{34}S = +10$ to $+26‰$) coeval seawater that was enclosed/trapped by the corresponding sedimentary strata (Claypool et al., 1980; Seal, 2006). This means that (i) salt-gypsum rocks provide the majority of S; (ii) the main sources of S are the coeval seawater sulfate; or (iii) all the
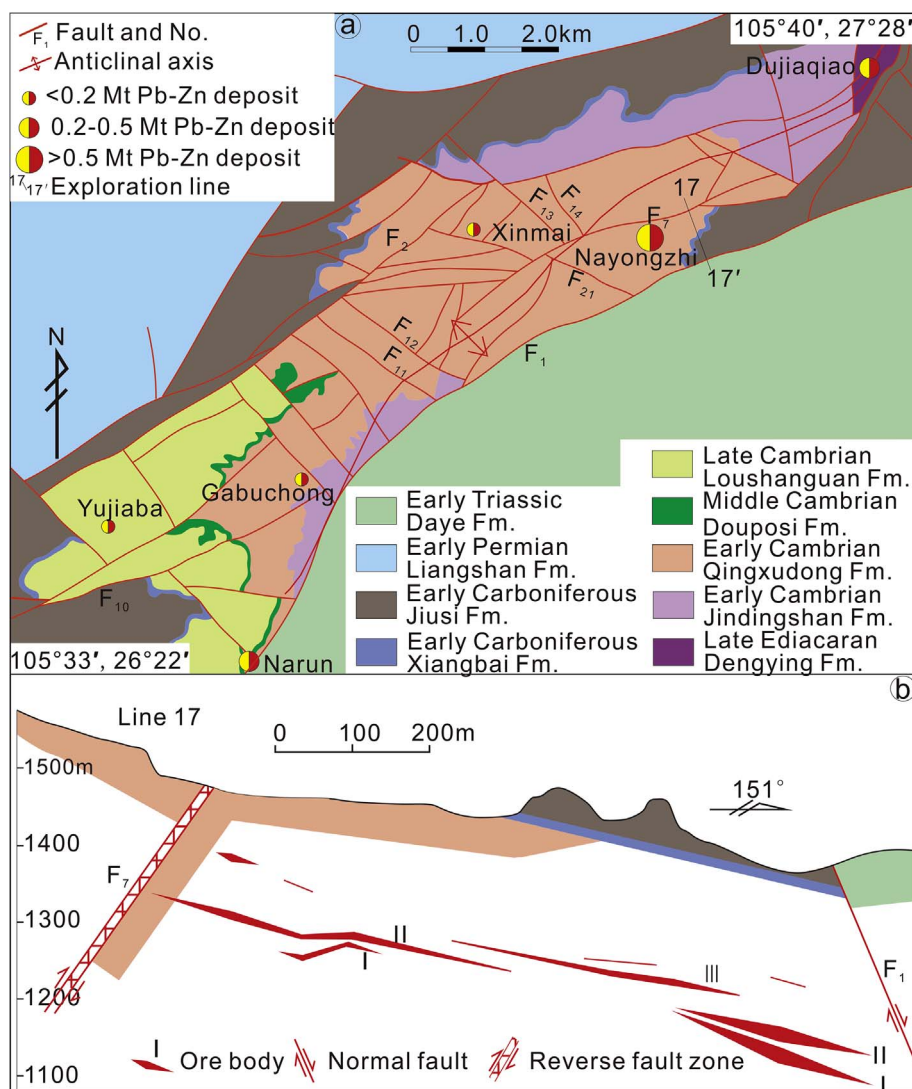
Fig. 17. (a) Geological sketch map of the Wuzhishan region (modified from Jin et al., 2016b; Zhou et al., 2018a); (b) cross-section map of No. 17 exploration line in the Nayongzhi mining area (modified from Jin et al., 2016b; Zhou et al., 2018a).

potential reservoirs are S sources.

Assumed that S was completely derived from evaporites, as the processes of thermochemical sulfide reduction (TSR) or bacterial sulfate reduction (BSR) can generate up to $+15‰$ or $-30‰$ of the $\Delta^{34}S_{sulfate-sulfide}$ value, respectively (Ohmoto et al., 1990; Worden et al., 1995; Ohmoto and Goldhaber, 1997; Basuki et al., 2008), so the predicted $\delta^{34}S_{sulfide}$ value could drop to $-3.2‰$ or $-18.2‰$, respectively. The theoretical $\delta^{34}S_{sulfide}$ values (-18.2 to $+28.3‰$) match well with the observed $\delta^{34}S$ values (-18.1 to $+25.5‰$). Similarly, if S was totally sourced from coeval seawater sulfate ($+10$ to $+32‰$), the theoretical $\delta^{34}S_{sulfide}$ values (-20 to $+32‰$) also match well with the determined $\delta^{34}S$ values (-18.1 to $+25.5‰$). Furthermore, the $\delta^{34}S_{pyrite}$ and $\delta^{34}S_{fluid}$ values also support that both evaporites and coeval seawater sulfate were involved in the supply of S. On the other hand, the evidence of geology, mineralogy and geochronology (Huang et al., 2004, 2010; Bai et al., 2013; Zhou et al., 2013a, 2014a, 2018b; Xu et al., 2014; Li et al., 2015, 2016; Zhu et al., 2016a, 2016b; Tan et al., 2017), as well as C–O, Zn and Pb–Sr isotopes (see Sections 5, 7 and 8), suggesting that both mantle and metamorphic fluids were involved in ore formation. Although the contributions of metamorphic rocks/fluids- or mantle-derived S cannot be ruled out, they are certainly not the only source (Fig. 27). Hence, the main sources of S are marine-derived sulfate, but having diverse contributions from metamorphic rocks/fluids and mantle-derived S in local. For example, at the Yunluhe deposit (sphalerite and galena have $\delta^{34}S$ values range of -1.5 to $+2.7‰$), mantle-

derived S was dominant in the hydrothermal systems (Fig. 26). The caveat is that S^{2-} originated from metamorphic and mantle reservoirs may be trapped at the mineralized areas before metal-rich fluids arrived, as the ELIP (~ 260 Ma: Zhou et al., 2002) occurred earlier than the Pb–Zn mineralization (245–190 Ma; see below) in the western Yangtze Block.

The reduction of sulfate occurs via both abiotic thermochemical (TSR) and bacterially mediated (BSR) processes, which are temperature-dependent (Ohmoto, 1972; Hoefs, 2009; Seal, 2006). TSR activates at a relatively high temperature (> 100–$140\,°C$: Machel et al., 1995; Worden et al., 1995) and can form abundant reduced S rapidly with relatively stable $\delta^{34}S$ values (Ohmoto et al., 1990; Zhou et al., 2013d). BSR occurs at a relatively low temperature ($< 110\,°C$: Jørgenson et al., 1992; Basuki et al., 2008) and can generate plentiful S^{2-} slowly with various $\delta^{34}S$ values (Habicht and Canfield, 1997; Machel, 2001). The homogenization temperatures of fluid inclusions (120–280 °C) (Jin, 2008; Zhou et al., 2013d; Zhu et al., 2016a; Liu et al., 2017) are too high for bacteria to survive, hence BSR should be occurred before the formation sulfide ores. This is in agreement with mineralogical records, for example, pyrite crystals from the Maozhachang deposit have granular and metasomatic textures imply that they are hydrothermal in origin, whereas pyrite crystals from the Liangyan and Yunluhe deposits occur as colloidal forms or framboids that indicate a biological process (Fig. 23) (Jin, 2008; Zhang et al., 2016). In addition, reserves of sulfide ores in the NW Guizhou district are > 50 Mt (Jin, 2008; Zhou et al.,
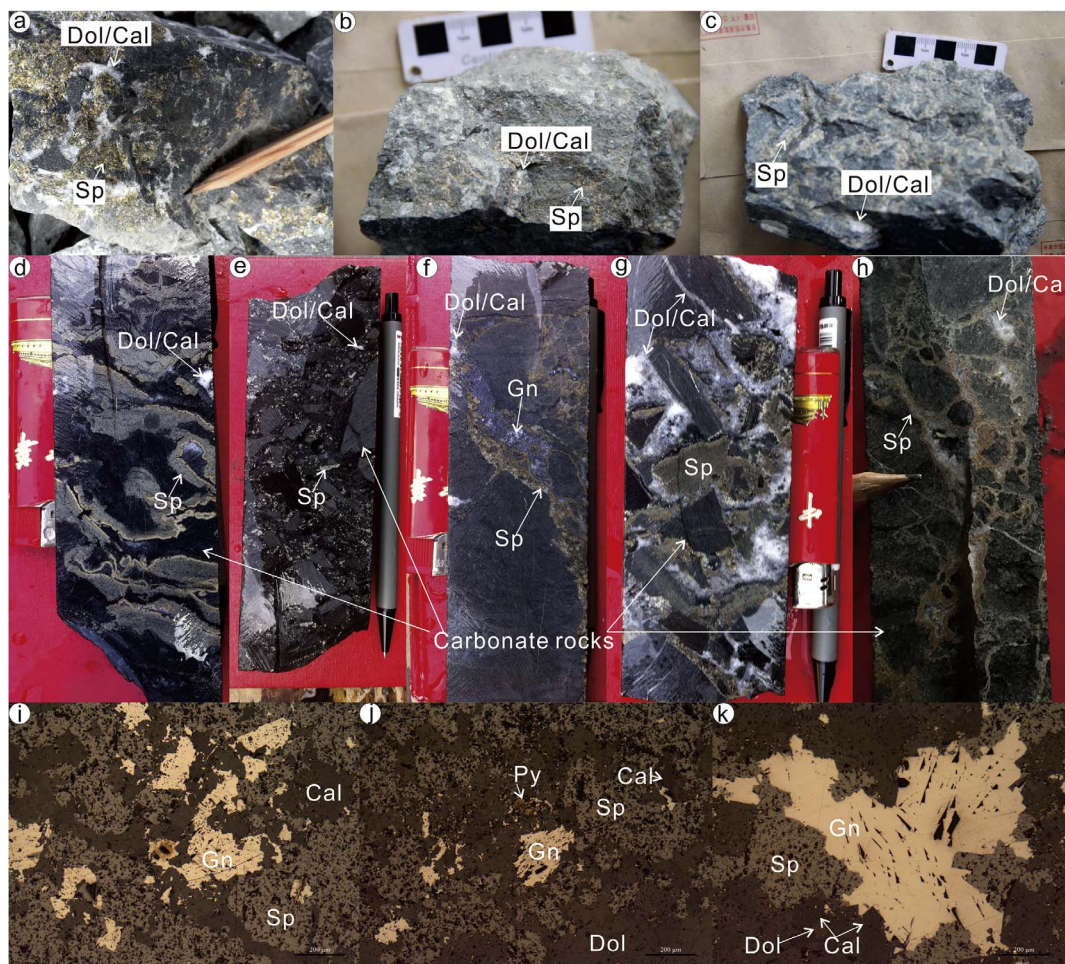
Fig. 18. Photographs of hand specimens and microscope; (a)–(b) dense disseminated ore, sphalerite occurs as aggregates within wall rocks and calcite cements them; (c)–(d) sphalerite veinlets cement carbonate breccia and calcite fragments fill the fractures of carbonate rocks; (e) sphalerite exhibits disseminated structure cement carbonate breccia; (f) dolomite/calcite fragments within sphalerite and galena veins; (g) sphalerite and dolomite/calcite cement carbonate breccia; (h) dolomite/calcite fragments within sphalerite that cements carbonate breccia; (i) calcite veinlets and galena fragments fill the fractures of sphalerite; (j) calcite, dolomite, pyrite and galena fragments fill the fractures of sphalerite; (k) calcite fragments are enclosed by dolomite that coexists with sphalerite and galena. Sp = sphalerite; Py = pyrite; Gn = galena; Dol = dolomite; Cal = calcite.

2013a), implicating a huge requirement of reduced S. Hence, although both TSR and BSR played an important role in the generation of S^{2-}, the BSR only taken place before Pb–Zn mineralization at the depositional sites or in oil and gas reservoirs. This is also supported by colloforms and framboids of pyrite crystals (rich in light S isotopes) from the Liangyan (Fig. 23) and Yunluhe deposits (Zhang et al., 2016).

As the variations of S isotopic compositions can reflect the degrees of TSR/BSR and the contributions from each S reservoirs, hence such variations can reveal the environments, migration paths or evolution of the hydrothermal systems. The $\delta^{34}S$ values of sulfides and associated fluids increase from the Qingshan to Nayongzhi deposits, but decrease from the Tianqiao to Banbanqiao and Yinchangpo to Yunluhe deposits (Figs. 24–26). This shows that the contributions from marine-derived sulfate and the degrees of TSR/BSR were increased from the NW to the SE along the Qingshan-Shanshulin fault, but were decreased from the SSW to the NNE along the Yinchangpo-Yunluhe fault and from the SWW to the NEE along the Maozhachang-Banbanqiao fault (Fig. 3). In contrast, the contributions from mantle (and/or metamorphic) fluids were increased from the Yinchangpo to Yunluhe deposits along the NNE-trending fault. Hence, the migration paths or evolution of the hydrothermal systems were likely from west to east (namely from the Yinchangpo to Yunluhe and Tianqiao to Banbanqiao deposits) in the western part of the NW Guizhou district, as suggested by C–O isotopes (Fig. 20; see Section 5.2), whereas from east to west (i.e. the Nayongzhi to Qingshan deposits) in the eastern part.

7. Zinc isotopic compositions

7.1. Variations of Zn isotopic compositions

The published Zn isotopic data of sphalerite from the Tianqiao, Banbanqiao and Shanshulin deposits, and ore-bearing sedimentary rocks, underlying basement metamorphic rocks and mantle-derived rocks of the ELIP in the NW Guizhou district and adjacent region (Zhou et al., 2014a, 2014b, 2016b; He et al., 2016) are listed in Appendix Table S3 and are shown in Figs. 28 and 29.

The Pb–Zn sulfide deposits in the NW Guizhou district record Zn isotopes range from −0.26 to +0.71‰ (+0.28‰ on average, relative to the JMC 3-0749L standard). Among them, the Tianqiao and Banbanqiao deposits have $\delta^{66}Zn$ values of sphalerite ranging from −0.26 to +0.58‰ (+0.26‰ on average) and +0.07 to +0.71‰ (+0.42‰ on average), respectively, and the Shanshulin deposit has $\delta^{66}Zn$ values of 0 to +0.55‰ for sphalerite (+0.25‰ on average). There is a gradual increasing of $\delta^{66}Zn$ values from generation-I (early phase) to generation-III (late phase) of sphalerite in the above three deposits (Fig. 28). In addition, from the Tianqiao to Banbanqiao deposits, the $\delta^{66}Zn$ values are increased, and from the Tianqiao to Shanshulin deposits, the $\delta^{66}Zn$ values also have an increased trend (Fig. 28). As compared end members, basalts of the ELIP have $\delta^{66}Zn$ values ranging from +0.30 to +0.44‰ (+0.35‰ on average), which are similar to those of basalts worldwide (+0.32 ± 0.16‰, Wang and
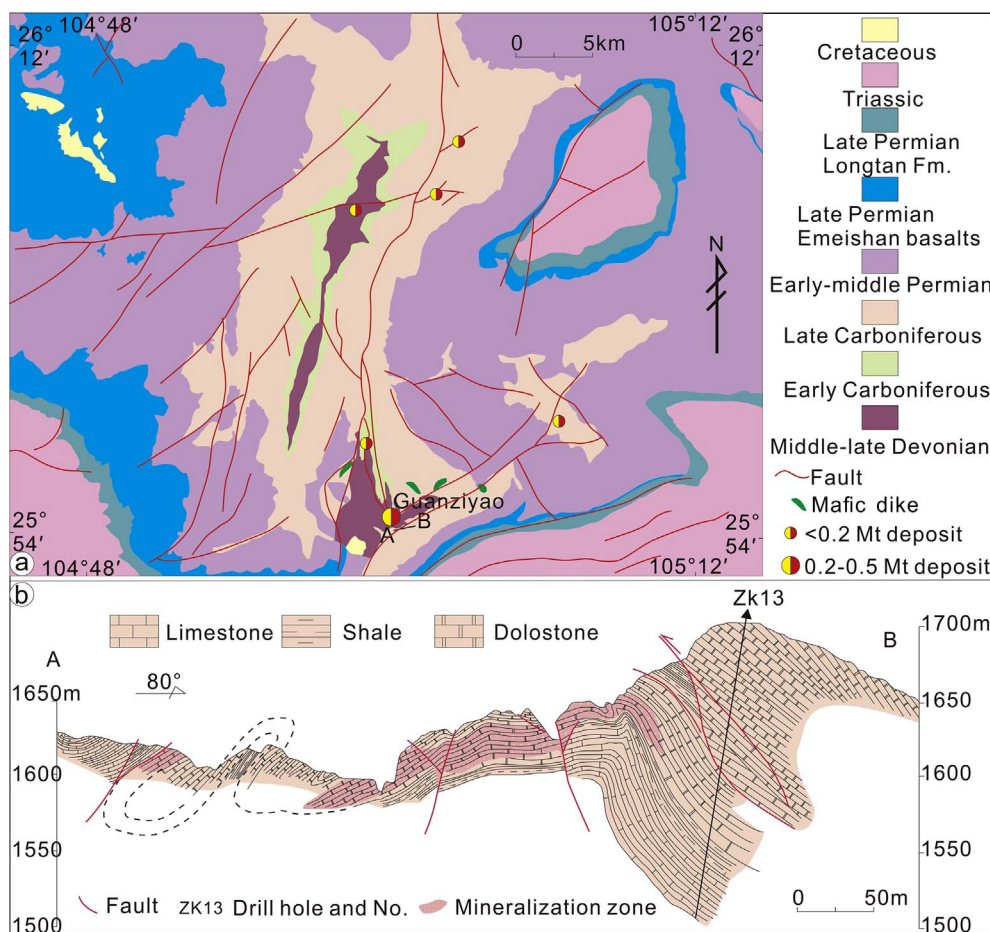
Fig. 19. (a) Geological sketch map of the Guanziyao region (modified from Zeng et al., 2017); (b) A–B cross-section map in the Guanziyao mining area (modified from Zeng et al., 2017).

Zhu, 2010), and ore-bearing sedimentary rocks of late Ediacaran to middle Permian have δ^{66}Zn values in a range of -0.24 to $+0.35‰$ ($+0.01‰$ on average) that are lower than that of underlying basement metamorphic rocks (δ^{66}Zn $= +0.62‰$: He et al., 2016).

7.2. Causes of Zn isotopic variations and sources of hydrothermal systems

It has been documented that Zn isotopes can be used to trace the geochemical processes of extraction, transportation and precipitation of Zn in hydrothermal systems (Mason et al., 2005; Wilkinson et al., 2005; John et al., 2008; Toutain et al., 2008; Kelley et al., 2009; Fujii et al., 2011; Gagnevin et al., 2012; Pašava et al., 2014; Zhou et al., 2014a, 2014b, 2016b; Duan et al., 2016). Significant variations of Zn isotopic compositions have been reported for sphalerite from Pb–Zn deposits of volcanic-hosted massive sulfide (VHMS)-type (Mason et al., 2005), magmatic-type (Jiang et al., 2001), magmatic hydrothermal-type (Duan et al., 2016), sedimentary exhalative (SEDEX)-type (Kelley et al., 2009), Kipushi-type (Sonke et al., 2008), Mississippi Valley-type (MVT) (Albarède, 2004; Pašava et al., 2014; Zhou et al., 2016b), Irish-type (Wilkinson et al., 2005; Gagnevin et al., 2012) and SYG-type (Zhou et al., 2014a, 2014b). These studies indicated the variations of Zn isotopic compositions are likely caused by (i) temperature gradients (Mason et al., 2005; Toutain et al., 2008), (ii) multiple Zn reservoirs (Wilkinson et al., 2005; He et al., 2016), or (iii) fractional crystallization (Kelley et al., 2009; Gagnevin et al., 2012; Zhou et al., 2014a, 2014b, 2016b).

It has been experimentally and field documented that there is no correlation existing between Zn isotopic compositions and temperature gradients at medium-low temperature conditions (namely $< 300\,°C$) (Maréchal and Sheppard, 2002; Wilkinson et al., 2005). The homogenization temperatures of fluid inclusions in hydrothermal minerals

from the NW Guizhou district are mainly between 120 and 280 °C (Jin, 2008; Zhou et al., 2013a; Zhu et al., 2016a; Liu et al., 2017). This means that the temperature gradients play an insignificant role in the variations of Zn isotopic compositions (Fig. 28). On the other hand, as discussed above, all the geological units (including late Permian Emeishan basalts, Paleozoic sedimentary rocks and Proterozoic metamorphic rocks) in the western Yangtze Block have the probability to supply mineralizing metals and associated fluids for the hydrothermal systems (Figs. 20–27). These source rocks have δ^{66}Zn values ranging from -0.24 to $+0.62‰$, which are in agreement with those of sphalerite (δ^{66}Zn $= -0.26$ to $+0.71‰$) within measurement uncertainties (Fig. 28). Our previous thinking eliminated the mixing of multiple Zn sources as a crucial cause in controlling the variations of Zn isotopic compositions (Zhou et al., 2014a, 2014b). This is due to the ^{66}Zn-enriched end members, such as basement rocks, lacking constraint of Zn isotopes. The fluids derived from, flowed through or interacted with high δ^{66}Zn values of Proterozoic metamorphic rocks ($+0.62‰$: He et al., 2016) should be rich in heavy Zn isotopes if the fractionation is negligible during the extraction of Zn. Hence, the mixing of multiple reservoirs can also cause the Zn isotopic variations. However, as suggested by stable (C–O–S, see above) and radiogenic (Pb–Sr, see below) isotopes, the major contributions from mantle/metamorphic fluids were at early phase. Thus, the mixing of multiple Zn reservoirs should cause heavy Zn isotopes precipitated at early ore formation stage, which does not match our observations (Fig. 28). On the other hand, the Rayleigh fractionation has been commonly employed to explain the increasing of δ^{66}Zn values from early to late phases (Gagnevin et al., 2012; Kelley et al., 2009; Mason et al., 2005; Wilkinson et al., 2005; Zhou et al., 2014a, 2014b, 2016b). In this study, as Zn isotopes follow the trend from lighter to heavier during the precipitation of sphalerite in the hydrothermal systems, so the fractional crystallization is likely
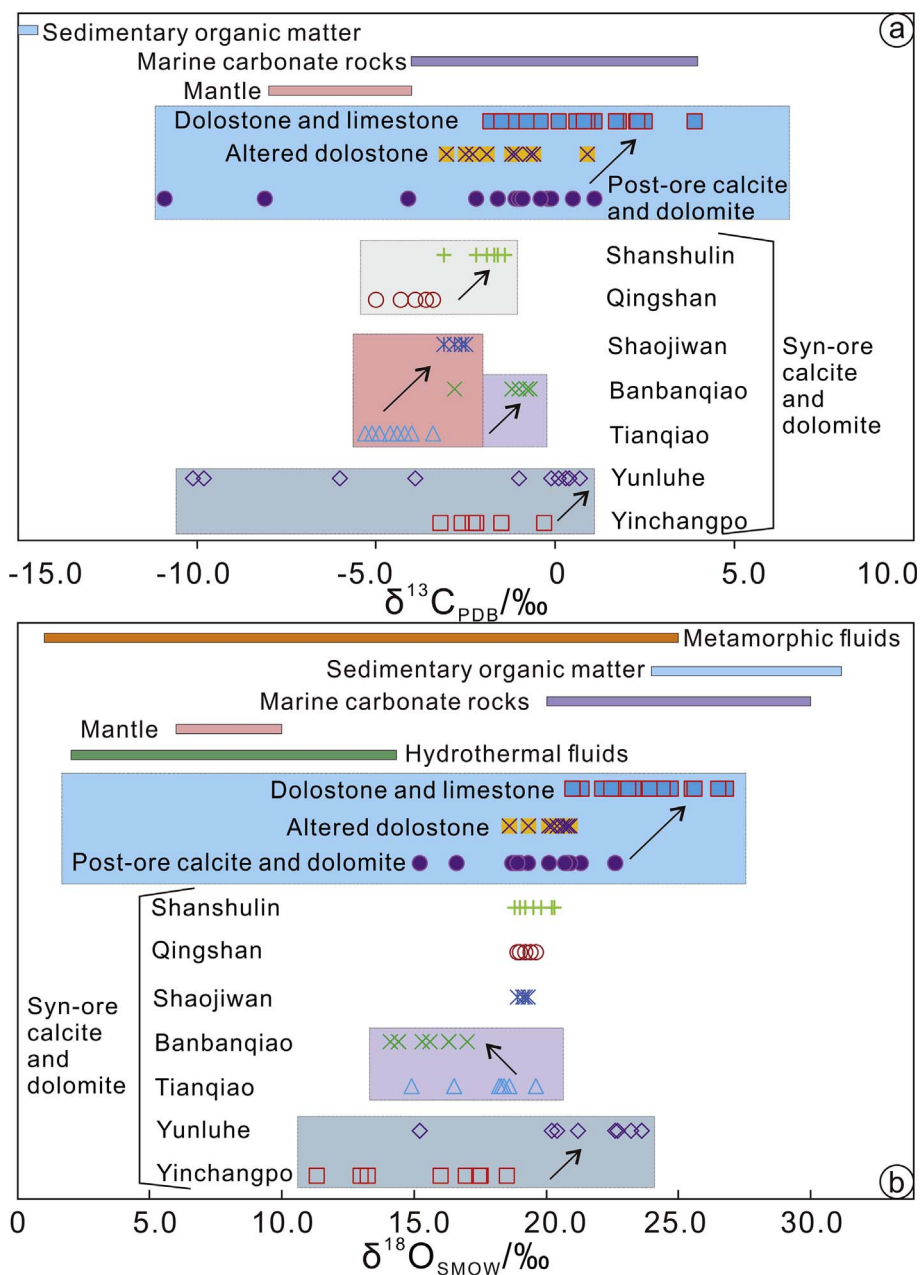
Fig. 20. Comparison plots of C (a) and O (b) isotopic compositions among syn-ore calcite/dolomite, post-ore calcite/dolomite, altered dolostone, and fresh dolostone/limestone in the studied region and adjacent area (Chen, 1986; Wang, 1996; Mao et al., 1998; Zhang et al., 1998; Hu, 1999; Mao, 2000; Dou and Zhou, 2013; Zhou et al., 2013a, 2013c), and mantle (Taylor et al., 1967; Demény et al., 1998), marine carbonate rocks (Veizer and Hoefs, 1976) and sedimentary organic matters (Kump and Arthur, 1999; Hoefs, 2009).

responsible for the variations of Zn isotopic compositions in time and space (Zhou et al., 2014a, 2014b).

Our recent research suggests that the ELIP played an important role in the ore formation of the Pb–Zn deposits in the Upper Yangtze metallogenic province (Zhou et al., 2018b). The average $\delta^{66}Zn$ value (+0.28‰) of sphalerite is similar to that of basalts ($\delta^{66}Zn = +0.32 \pm 0.16$‰, Wang and Zhu, 2010), indicating that the sources of Zn were likely associated with mantle-derived rocks of the ELIP. In addition, the concentrations of Zn in the Emeishan basalts are 66–156 µg/g (Huang et al., 2004; Xu et al., 2001, 2007), showing that the ELIP has the potential to provide abundant Zn to the hydrothermal systems. Moreover, compared with the main types of Pb–Zn deposits worldwide, the $\delta^{66}Zn$ values of the Upper Yangtze-type deposits are most similar to those of Irish-type ones (Fig. 29) (Wilkinson et al., 2005; Gagnevin et al., 2012). The hydrothermal fluids responsible for the Irish-type deposits was considered to be associated with mantle (Davidheiser-Kroll et al., 2014), which is similar to that of the Pb–Zn deposits within the ELIP (Zhou et al., 2018b). Hence, we propose that

the sources of Zn were most likely related to the ELIP with the diverse influences from sedimentary and metamorphic rocks, and the initial Zn isotopic compositions are controlled by the contributions from each end member.

As the Zn isotopic variations were controlled by the fractional crystallization, so the increased trend of $\delta^{66}Zn$ values can reveal the migration paths or evolution of the hydrothermal systems. In this study, the $\delta^{66}Zn$ values gradual increase from the SWW to the NEE along the Maozhachang-Banbanqiao fault (Fig. 3), and from the NW to the SE along the Kangding-Yiliang-Ziyun fault (KYZ in Fig. 2a), indicating that the migration paths or evolution of hydrothermal systems were most likely from west to east, namely from the Tianqiao to Banbanqiao deposits and from the Tianqiao to Shanshulin deposits (Fig. 28), which are in agreement with the implications from C–O and S isotopes (Figs. 20 and 24–25; see Sections 5.2 and 6.2).
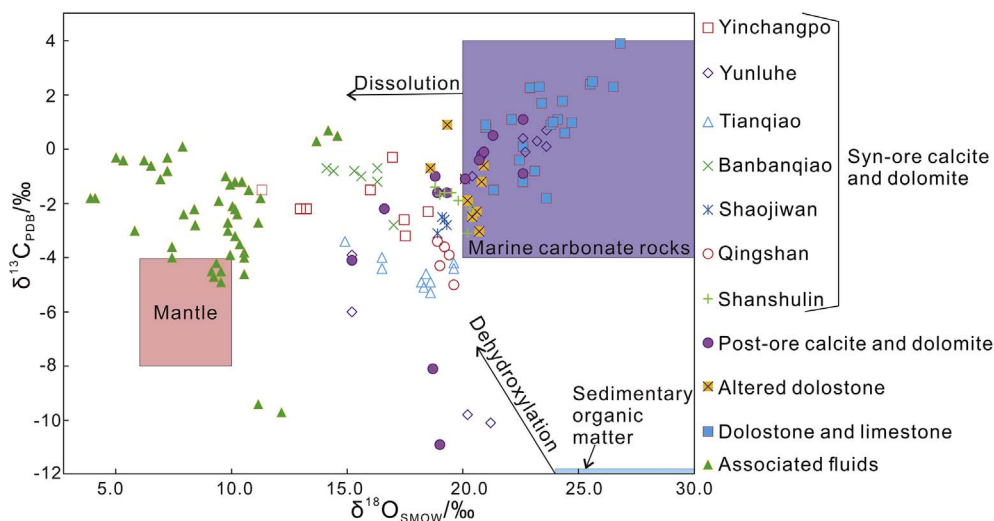
Fig. 21. Diagram of $\delta^{13}C$ vs. $\delta^{18}O$ of syn- and post-ore calcite/dolomite, as well as altered and fresh dolostone/limestone in the studied region and adjacent area (Chen, 1986; Wang, 1996; Mao et al., 1998; Zhang et al., 1998; Hu, 1999; Mao, 2000; Dou and Zhou, 2013; Zhou et al., 2013a, 2013c, 2014b; Li et al., 2015; Jin et al., 2016a), and mantle (Taylor et al., 1967; Demény et al., 1998), marine carbonate rocks (Veizer and Hoefs, 1976) and sedimentary organic matters (Kump and Arthur, 1999; Hoefs, 2009).
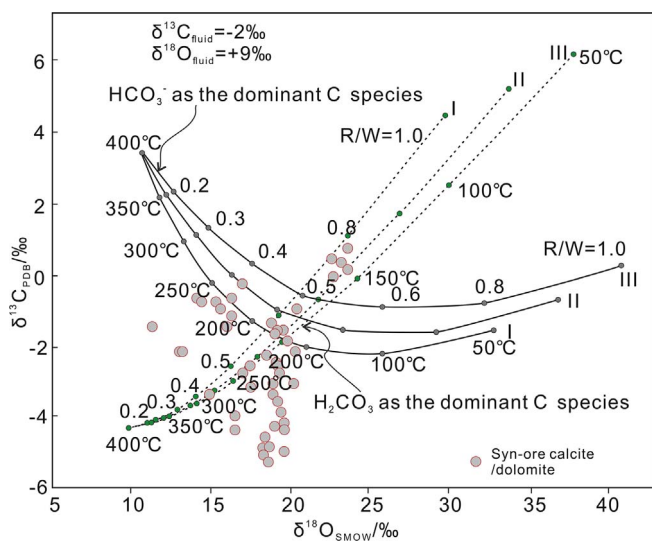
Fig. 22. Diagram of $\delta^{13}C$ vs. $\delta^{18}O$ for calcite/dolomite precipitated though W/R interaction with different R/W ratios and temperatures (400–50 °C) for either HCO_3^- or H_2CO_3 as the dominant C species (after Zheng and Hoefs, 1993), showing the position of syn-ore calcite/dolomite. Initial fluids: $\delta^{13}C = -2‰$, $\delta^{18}O = +9‰$. $\Delta = \delta_{rock} - \delta_{rock}^f$; I: $\Delta^{13}C = +0.2‰$, $\Delta^{18}O = +2‰$; II: $\Delta^{13}C = +1‰$, $\Delta^{18}O = +6‰$; III: $\Delta^{13}C = +2‰$, $\Delta^{18}O = +10‰$.

8. Lead isotopic compositions

8.1. Variations of Pb isotopic compositions

Femtosecond (fs) LA-MC-ICPMS in situ Pb isotopic data for galena crystals from the Maozhachang and Liangyan deposits, and previously reported bulk Pb isotopic data for sulfide minerals/ore in the Yinchangpo, Yunluhe, Fulaichang, Tianqiao, Banbanqiao, Mangdong, Shaojiwan, Qingshan, Shanshulin, Nayongzhi and Guanziyao deposits (Wang, 1993; Zheng, 1994; Hu, 1999; Zhang et al., 1998, 2016; Liu and Lin, 1999; Fu, 2004; Tang et al., 2012; Zhou et al., 2013a, 2013b, 2013c, 2014a, 2014b; Li et al., 2015; Jin et al., 2015, 2016b; Xiang et al., 2015; Chen et al., 2017; Zeng et al., 2017) are listed in Appendix Table S4 and are displayed in Figs. 30–32.

Galena crystals from the Maozhachang and Liangyan deposits have in situ $^{206}Pb/^{204}Pb$ ratios ranging from 18.637 to 18.775 (18.719 on average), $^{207}Pb/^{204}Pb$ ratios from 15.767 to 15.799 (15.785 on average) and $^{208}Pb/^{204}Pb$ ratios from 39.228 to 39.477 (39.371 on average), which overlap with previous published bulk Pb isotopic data

($^{206}Pb/^{204}Pb = 17.824–18.768$, 18.355 on average; $^{207}Pb/^{204}Pb = 15.440–15.920$, 15.695 on average; and $^{208}Pb/^{204}Pb = 37.896–39.641$, 38.730 on average). As shown in the Fig. 30, all the Pb isotopic data plot into two groups. In addition, Pb isotopic ratios of the Yinchangpo deposit cover the range of Pb isotopic data for the Yunluhe deposit (Fig. 31a and b). However, from the Maozhachang to Banbanqiao (Fig. 31c and d), Liangyan to Yunluhe (Fig. 31e and f) and Qingshan to Nayongzhi deposits (Fig. 31g and h), the Pb isotopic ratios of sulfides are gradually decreased.

8.2. Sources of Pb and evolution of hydrothermal systems

The extremely low U and Th contents in sulfide minerals (Carr et al., 1995; Muchez et al., 2005; Pass et al., 2014; Zhou et al., 2016a, 2018a) imply that the Pb isotopic ratios of sulfides are approximate to their corresponding hydrothermal fluids. This enables us to use the Pb isotopes of sulfides to determine the sources, migration paths or evolution of hydrothermal systems.

All the Pb isotopic data plot into the field that crosscuts the Pb evolution curves of mantle, orogenic belt and upper continental crust in the Fig. 32a (Zartman and Doe, 1981), exhibiting that the sources of Pb are complex. Such field also crosscuts those of modern main reservoirs (lower crust, oceanic island volcanic rocks and pelagic sediments; Fig. 32a and b; Zartman and Doe, 1981), further showing that Pb was likely derived from multiple sources.

It has been documented that there are at least three main potential metal sources in the Upper Yangtze Pb–Zn metallogenic province, i.e. mantle-derived rocks of the ELIP, Paleozoic ore-bearing sedimentary rocks and Proterozoic underlying basement metamorphic rocks (Zheng and Wang, 1991; Zhou et al., 2001, 2013a; Huang et al., 2004; Li et al., 2007, 2015, 2016; Zhang et al., 2015b; Jin et al., 2016b; Zhu et al., 2017). Compared with the ore formation age-corrected (245–200 Ma, peaked at 200 Ma; see Section 9.1) Pb isotopic ratios of Emeishan basalts and affinal diabase, sedimentary rocks, and basement rocks, the Pb isotopic ratios of sulfide minerals/ore are overlapping with all of them (Fig. 32a). This means that all the source rocks have the potential to provide Pb to the hydrothermal systems. However, there are clearly two groups of all the Pb isotopic data in Fig. 30, suggesting that there may be two main sources of Pb. In addition, the concentrations of Pb in the Emeishan basalts are only 3–30 μg/g (Huang et al., 2004; Xu et al., 2001, 2007), displaying that the mantle-derived rocks do not have the potential to provide a mass of Pb to the hydrothermal systems. In contrast, the Emeishan basalts contain 6–323 μg/g Cu (Huang et al., 2004; Xu et al., 2001, 2007), and the main sources of Zn and other metals were associated with the ELIP as evidenced by the occurrence of
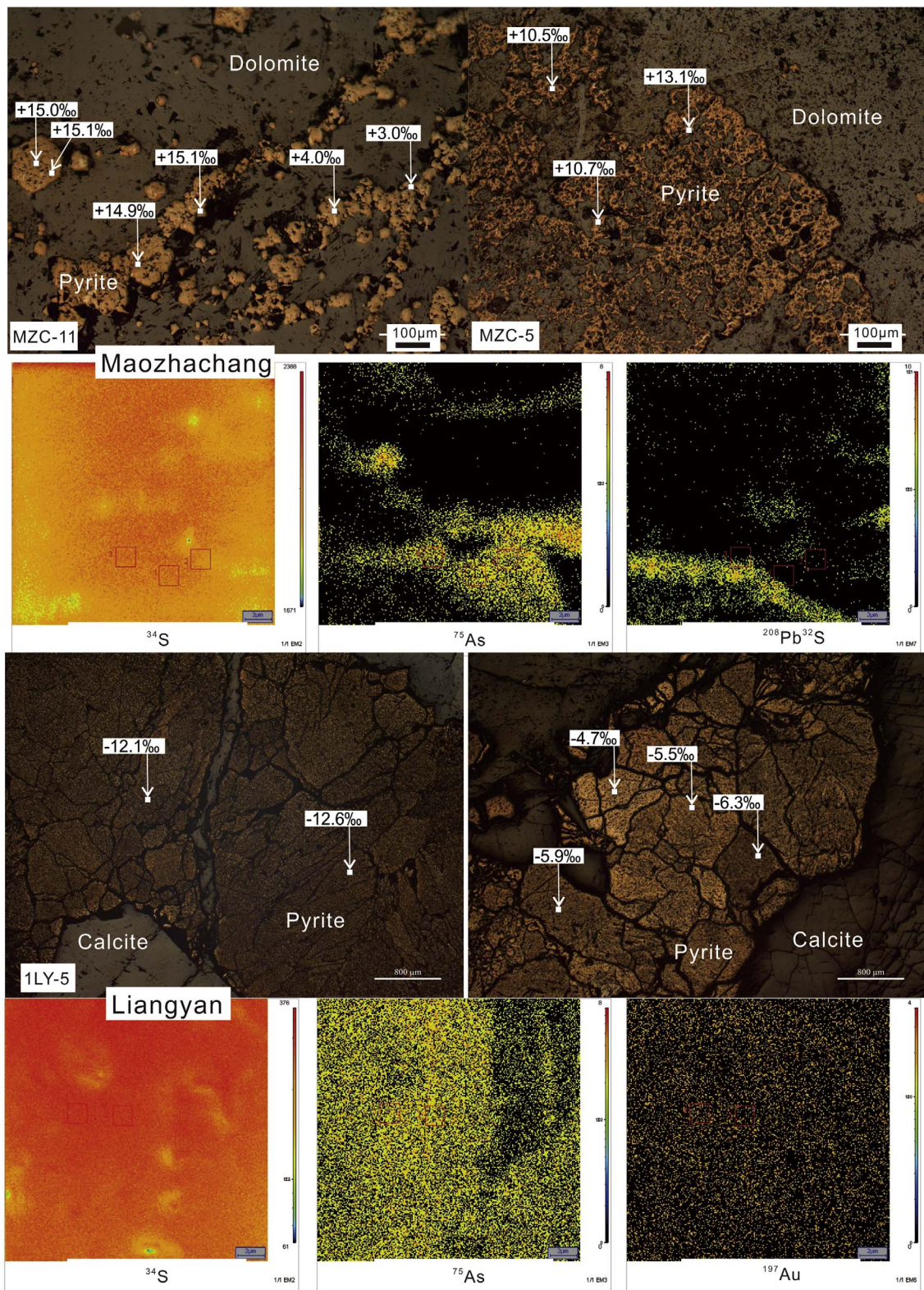
Fig. 23. NanoSIMS in situ S isotopic compositions of pyrite crystals from the Maozhachang and Liangyan Pb–Zn deposits, and their ^{34}S, ^{75}As, ^{208}Pb^{32}S and ^{197}Au micro-scale isotope mapping.

multiple Cu and Ni sulfide minerals (Zhou et al., 2018b), and C–O (Fig. 21), S (Fig. 27) and Zn isotopes (Figs. 28 and 29). Hence, the main sources of Pb are basement and sedimentary rocks, but having the various contributions from the ELIP locally.

In addition, Pb isotopic ratios of sulfides gradual decrease from the Maozhachang to Banbanqiao (Fig. 31c and d), Liangyan to Yunluhe

(Fig. 31e–f) and Qingshan to Nayongzhi deposits (Fig. 31g and h), revealing that the contributions of Pb from the basement rocks are gradually increasing, and the migration paths or evolution of the hydrothermal systems were likely from west to east in the western part of the NW Guizhou district, namely from the Yunluhe to Liangyan deposits along the NW-trending fault, whereas from east to west along the
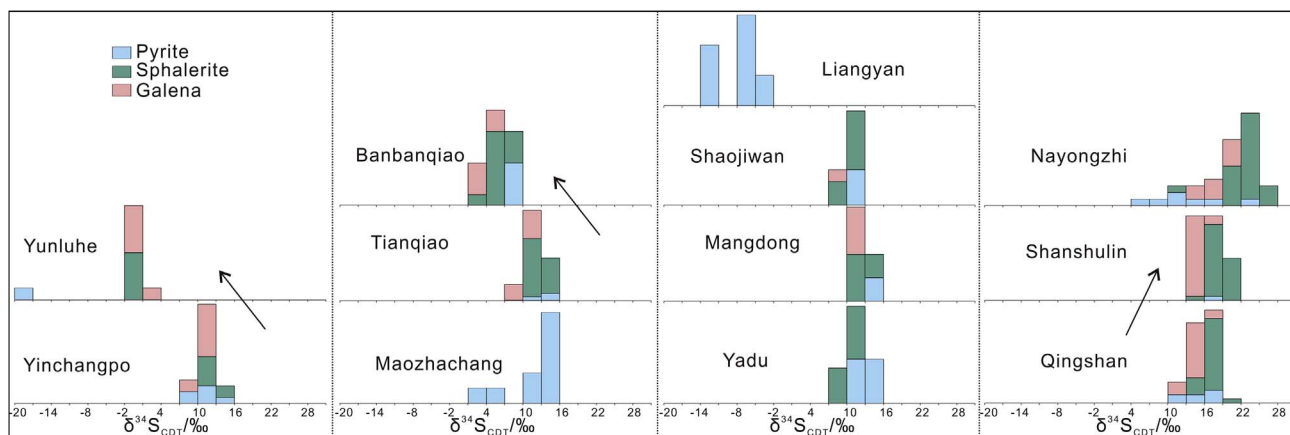
Fig. 24. A histogram of δ³⁴S values for sulfides from the chosen Pb–Zn deposits in the NW Guizhou district. Data are sourced from Chen (1986), Zhang et al. (1998, 2011, 2016), Hu (1999), Liu and Lin (1999), Fu (2004), Gu (2007), Jin (2008), Zhou et al. (2013d, 2014a, 2014b), Li et al. (2015), Xiang et al. (2015), Jin et al. (2016b), Chen et al. (2017) and Liu et al. (2017).
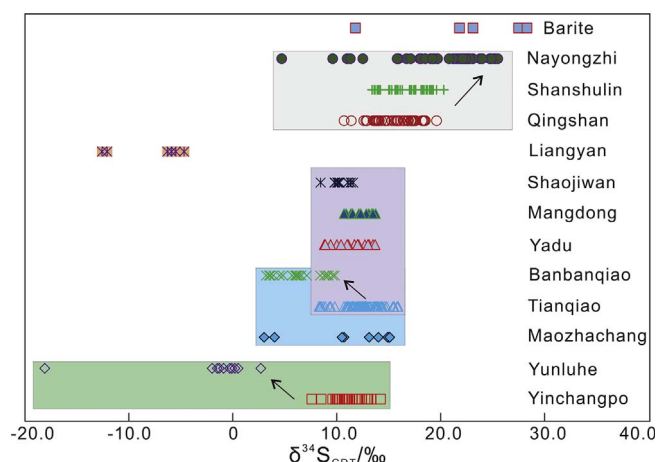

Fig. 25. A comparison plot of S isotopic compositions of sulfides among these chosen Pb–Zn deposits. The sources of data are the same to those in Fig. 23.

Fig. 26. Plot of δ³⁴S vs. Δ³⁴S for the coexisting sphalerite-galena pairs (after Zhou et al., 2013d; Liu et al., 2017).

Qingshan-Shanshulin and Maozhachang-Banbanqiao fault in the eastern part (Fig. 3), as suggested by S isotopes (see above).

9. Rubidium-Sr isotopic compositions and dating

9.1. Variations of Rb-Sr isotopic compositions

Bulk Rb–Sr isotopic data for hydrothermal minerals and ores in the Yinchangpo, Tianqiao, Shaojiwan, Qingshan and Shanshulin deposits, and whole-rock of Proterozoic metamorphic rocks, late Ediacaran to middle Permian sedimentary rocks and late Permian Emeishan basalts in the NW Guizhou district and adjacent area (Cong, 1988; Li and Qin, 1988; Chen and Ran, 1992; Gu, 1997; Hu, 1999; Deng et al., 2000; Huang et al., 2004; Jiang and Li, 2005; Shi et al., 2013; Zhou et al., 2013a, 2013b, 2013c, 2014b; Dou et al., 2014) are listed in Appendix Table S5 and are exhibited in Figs. 33 and 34.

Hydrothermal minerals/ores have Rb and Sr concentrations ranging from 0.03 to 13.5 μg/g (0.943 μg/g on average) and 0.5 to 338 μg/g (1835 μg/g on average), respectively, and have ⁸⁷Rb/⁸⁶Sr and ⁸⁷Sr/⁸⁶Sr ratios (Fig. 33a) ranging from 0.001 to 1.564 (0.223 on average) and 0.7107 to 0.7256 (0.7131 on average), respectively. Most of these Rb-Sr isotopic data did not yield isochron age, only five sulfides from the Tianqiao deposit record an isotopic age of 192 ± 7 Ma (Fig. 33b; Zhou et al., 2013a). There is a gradually decreasing of ⁸⁷Sr/⁸⁶Sr ratios for sulfide minerals/ores from the Yinchangpo to Tianqiao and Shaojiwan, and then to Qingshan and Shanshulin deposits along the regional
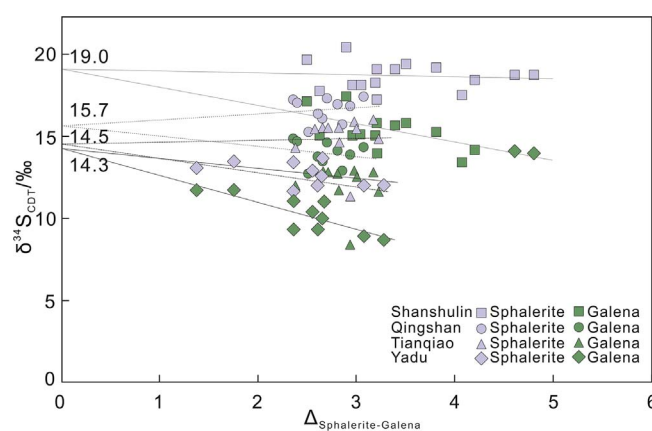
Kangding-Yiliang-Ziyun fault (KYZ in Figs. 2a, 3 and 33a).

On the other hand, ore-bearing sedimentary rocks have Rb and Sr concentrations of 0.005–15.2 μg/g (1.692 μg/g on average) and 23.5–350 μg/g (141.6 μg/g on average), respectively, and have ⁸⁷Rb/⁸⁶Sr and ⁸⁷Sr/⁸⁶Sr ratios of 0.0001–0.7365 (0.076 on average) and 0.7073–0.7174 (0.7098 on average) (Fig. 33a). Compared with the ⁸⁷Sr/⁸⁶Sr ratios of hydrothermal minerals/ores, the sedimentary rocks have lower ⁸⁷Sr/⁸⁶Sr ratios (0.7073–0.7105) with the exception of early Permian shale (⁸⁷Sr/⁸⁶Sr = 0.7174) and middle Devonian sandstone (⁸⁷Sr/⁸⁶Sr = 0.7132) (Fig. 33a).

9.2. Timing of Pb–Zn mineralization

Although the real status of Rb and Sr in sphalerite is still unclear, sphalerite Rb-Sr isotope system is the most reliable constraint on ore formation ages of base metal sulfide deposits due to lacking of suitable minerals and dating methods (Nakai et al., 1990; Brannon et al., 1992; Christensen et al., 1995; Li et al., 2005; Zhou et al., 2015). However, Rb–Sr dating of sphalerite is very difficult. Only a few sulfides Rb–Sr isochron ages for the Pb–Zn deposits in the western Yangtze Block were reported. For example, Yin et al. (2009) and Zhang et al. (2014b) reported sphalerite Rb-Sr isochron ages of 226–224 Ma and 196 ± 2 Ma for the Huize deposit, respectively. Sphalerite from the Paoma, Lehong and Jinshachang deposits records Rb-Sr isochron ages of 200 ± 1 Ma (Lin et al., 2010), 201 ± 8 Ma (Zhang et al., 2014b) and 207 ± 4 Ma (Zhou et al., 2015), respectively. Such ages match well with calcite/fluorite Sm–Nd isochron ages (Huize: 226–225 Ma, Li et al., 2007;
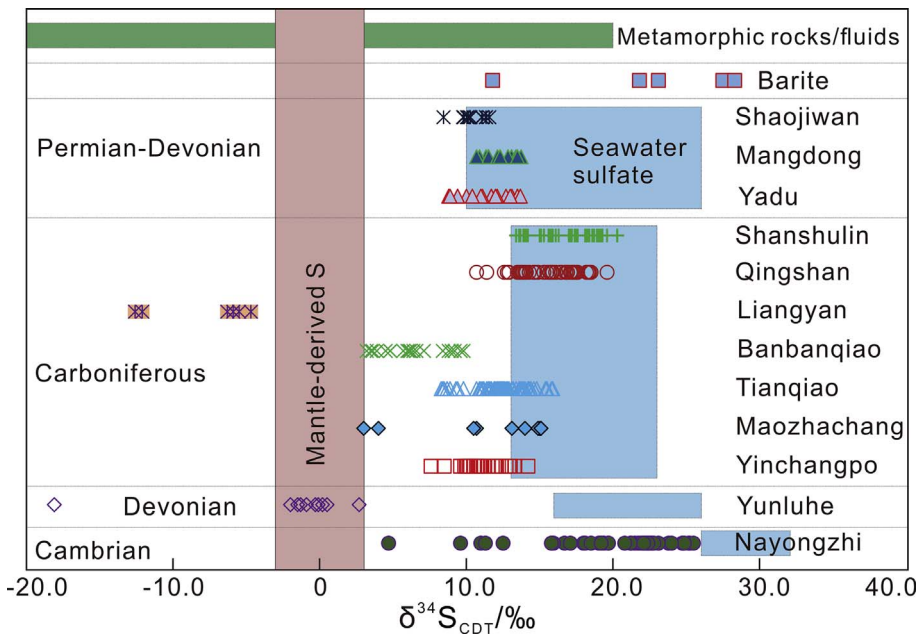
Fig. 27. A comparison plot of S isotopic compositions among sulfides from chosen Pb–Zn deposits, barite within evaporites, coeval seawater sulfate, mantle-derived S, and metamorphic rocks/fluids. The sources of data of sulfides and barite are the same to those in Fig. 23, other data are sourced from Claypool et al. (1980), Chaussidon et al. (1989), Seal et al. (2000), Seal (2006) and Hoefs (2009).
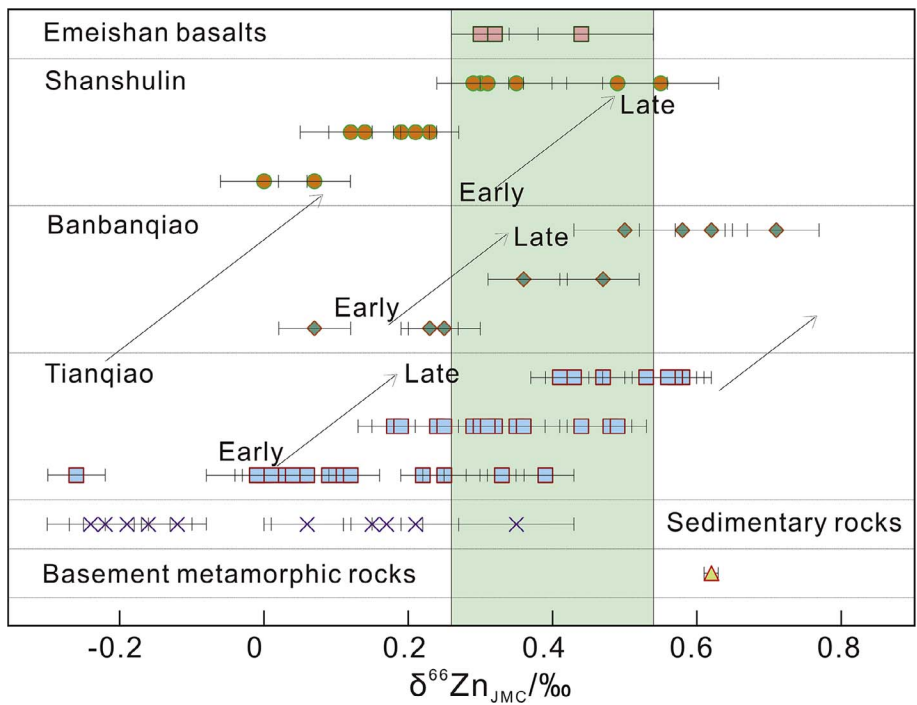

Fig. 28. The variation of Zn isotopes of sphalerite from chosen Pb–Zn deposits and whole-rock of Emeishan basalts, sedimentary rocks and metamorphic rocks. Data are sourced from Zhou et al. (2014a, 2014b, 2016b) and He et al. (2016).

Maozu: 196 ± 13 Ma, Zhou et al., 2013e; Jinshachang: 201 ± 6 Ma, Zhang et al., 2015b), and broadly match with those of basalt-hosted native Cu deposits (231–225 Ma: Zhu et al., 2007), Carlin-type Au deposits (235–204 Ma: Chen et al., 2015a) and detritus (~230–206 Ma) in the Songpan-Ganzê Orogenic Belt that are resulted from collision with the western Yangtze Block during late Triassic (Enkelmann et al., 2007). Thus, 230–200 Ma were considered to be the credible ore formation ages in the Upper Yangtze Pb–Zn metallogenic province (Zhou et al., 2014b; Hu et al., 2017). On the other hand, according to the Pb model ages, Guan and Li (1999) calculated that some Pb–Zn deposits in the western Yangtze Blocks were likely formed at ~245 Ma. Moreover, our recent research suggested that the formation of some Pb–Zn deposits is related to the ELIP and Indosinian orogeny, and the ore formation ages were most likely between 250 and 200 Ma (Zhou et al., 2018b). Hence, we propose that the Pb–Zn deposits in the Upper

Yangtze metallogenic province were most likely formed during Early Mesozoic (245–190 Ma), and can be divided into two main episodes, which are corresponding to early Triassic (245–220 Ma) and early Jurassic (215–190 Ma), respectively. The first episode of Pb–Zn mineralization was mainly occurred in the western part of the Upper Yangtze metallogenic province, whereas the second one is dominated in the eastern part (the NW Guizhou district in this study).

9.3. Sources and evolution of hydrothermal systems

Strontium (Sr) isotopes have been widely used to trace the sources, migration paths or evolution of hydrothermal fluids (Zheng and Wang, 1991; Yang and Zhou, 2001; Gromek et al., 2012; Deng et al., 2015; Beaudoin and Chiaradia, 2016). However, before using Sr isotopes of hydrothermal minerals, we need to obtain their initial $^{87}Sr/^{86}Sr$ ratios
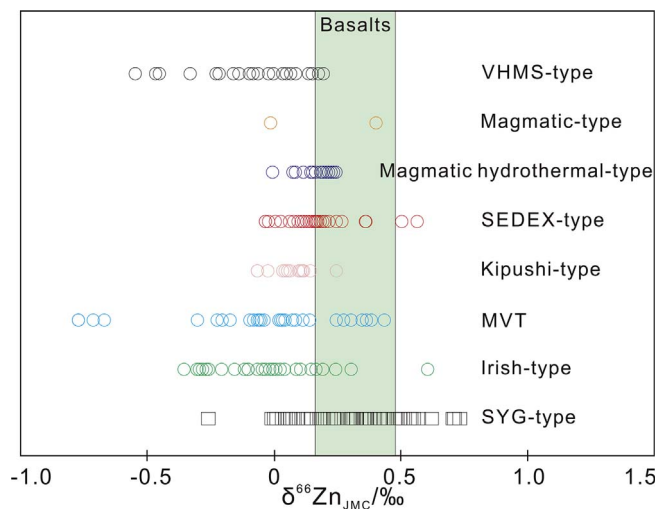
Fig. 29. A comparison plot of Zn isotopic compositions between the main types of Pb–Zn deposits worldwide and basalts. Data are sourced from Jiang et al. (2001), Albarède (2004), Mason et al. (2005), Wilkinson et al. (2005), Sonke et al. (2008), Kelley et al. (2009), Wang and Zhu (2010), Gagnevin et al. (2012), Pašava et al. (2014), Duan et al. (2016), He et al. (2016) and Zhou et al. (2016b).

(Deng et al., 2000; Zhou et al., 2013a; Gromek et al., 2012). As discussed above, the Pb–Zn deposits in the NW Guizhou district were most likely formed during 215–190 Ma (peaked at 200 Ma), so 200 Ma was used to calculate the initial $^{87}Sr/^{86}Sr$ ratios of minerals/ores and potential source rocks (Huang et al., 2004; Zhou et al., 2014b; Tan et al., 2017). Hydrothermal minerals and sulfide/oxidized ores have $^{87}Sr/^{86}Sr_{200\ Ma}$ ratios ranging from 0.7099 to 0.7255 (0.7125 on average), which are significantly higher than those of the age-corrected Emeishan basalts (Fig. 34; $^{87}Sr/^{86}Sr_{200\ Ma}$ = 0.7039–0.7078, 0.7058 on average: Huang et al., 2004) and upper mantle (0.704 ± 0.002: Faure, 1977), but overlap with those of age-corrected basement rocks (Fig. 34; $^{87}Sr/^{86}Sr_{200\ Ma}$ = 0.7243–0.7288; Cong, 1988Li and Qin, 1988; Chen and Ran, 1992) and sedimentary rocks (Fig. 34; $^{87}Sr/^{86}Sr_{200\ Ma}$ = 0.7073–0.7166, 0.7097 on average: Hu, 1999; Deng et al., 2000; Jiang and Li, 2005; Shi et al., 2013; Zhou et al., 2013b, 2014b). Such Sr isotope signatures indicate that the hydrothermal fluids were likely derived from, flowed through or interacted with basements and sedimentary rocks, and having the diverse influences from the ELIP.

Furthermore, as the basement rocks contain high radiogenic Sr, so the gradually decreased initial $^{87}Sr/^{86}Sr$ ratios from the Yinchangpo to Tianqiao and Shaojiwan, and then to Qingshan and Shanshulin deposits (Figs. 33 and 34), suggesting the contributions from basements are gradual decreased from west to east. This means that the migration paths or evolution of hydrothermal systems were most likely from west to east, namely from the Tianqiao to Shaojiwan and Qingshan, then to Shanshulin deposits along the NW-trending Kangding-Yiliang-Ziyun fault (KYZ in Fig. 2a). This is also supported by C–O (Fig. 20), Zn (Fig. 28) and Pb (Fig. 31) isotopes.

10. Ore genesis and a new genetic model

10.1. Ore genesis and relationship with the ELIP

Pb–Zn deposits in the NW Guizhou district spatially coexist with mantle-derived Emeishan basalts and mafic dikes (Figs. 2b, 3, 13a, 15a and 19a), which led some researches to classify them as a distal magmatic-hydrothermal type (Xie, 1963; Huang et al., 2004; Xu et al., 2014). Other lines of evidence for the linkage of Pb–Zn mineralization to Emeishan magmatism include the occurrence of hidden basalts-hosted Pb–Zn veins in the NE Yunnan district (Liu and Lin, 1999; Huang et al., 2004) and the mineralogical record of diverse Cu/Ni sulfides
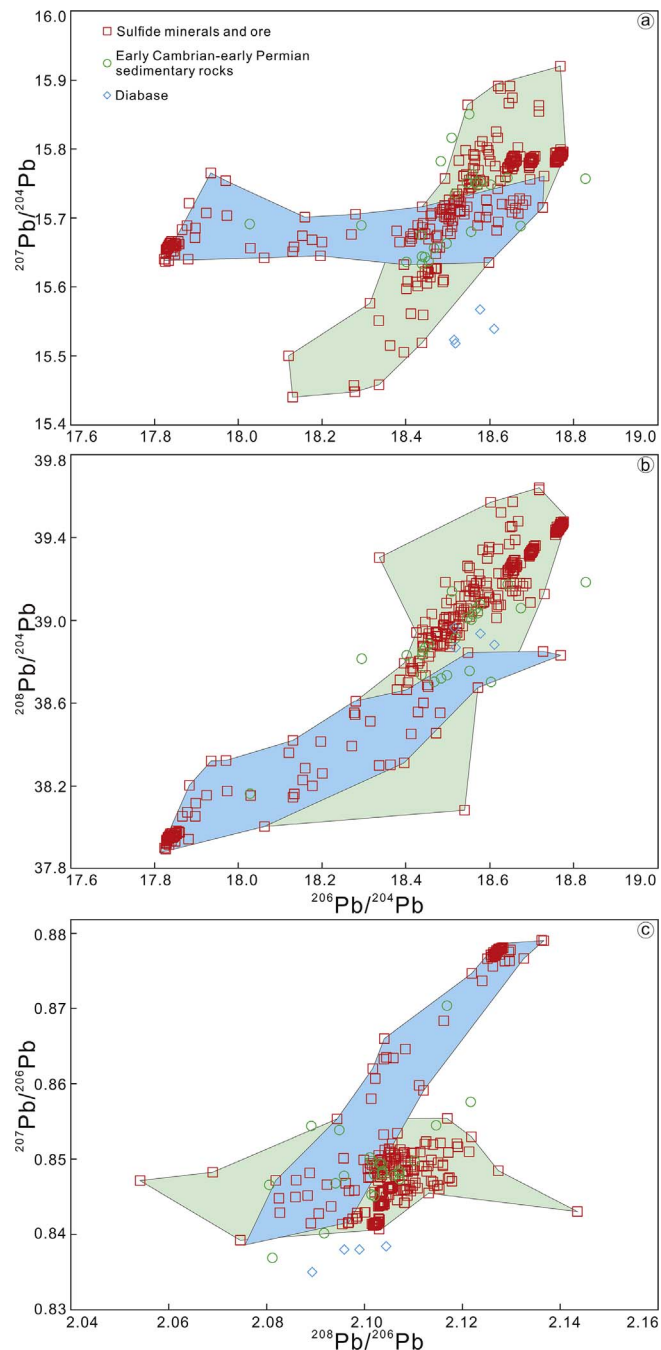

Fig. 30. Plots of $^{207}Pb/^{204}Pb$ vs. $^{206}Pb/^{204}Pb$ (a), $^{208}Pb/^{204}Pb$ vs. $^{206}Pb/^{204}Pb$ (b) and $^{207}Pb/^{206}Pb$ vs. $^{208}Pb/^{206}Pb$ (c) for sulfide minerals and ore, sedimentary rocks and diabase (c). Data are sourced from Wang (1993), Zheng (1994), Hu (1999), Zhang et al. (1998, 2016), Liu and Lin (1999), Fu (2004), Tang et al. (2012), Zhou et al. (2013a, 2013b, 2013c, 2014a, 2014b), Li et al. (2015), Jin et al. (2015, 2016b), Xiang et al. (2015), Bao et al., 2017; Chen et al. (2017), Kong et al., 2017; and Zeng et al. (2017).

coexisted with Pb–Zn sulfides in the Fule and other deposits (Zhou et al., 2018b). In contrast, sulfide ore bodies of Pb–Zn deposits in the NW Guizhou district occur in stratiform to lentiform shapes or veins that are clearly stratabound (Figs. 5b, 7b, 9b, 11b, 13b, 15b, 17b, and 19b), which led other researchers to classify them as a sedimentary exhalative (SEDEX)-type or sedimentary reworking-type (e.g. Zhang et al., 1998; Jin, 2008; Chen et al., 2015b). However, sulfide ore bodies of Pb–Zn deposits in the studied district are hosted by dolostone and limestone of late Ediacaran to middle Permian, which significantly differ from clastic rocks that host sulfide ore bodies of SEDEX-type
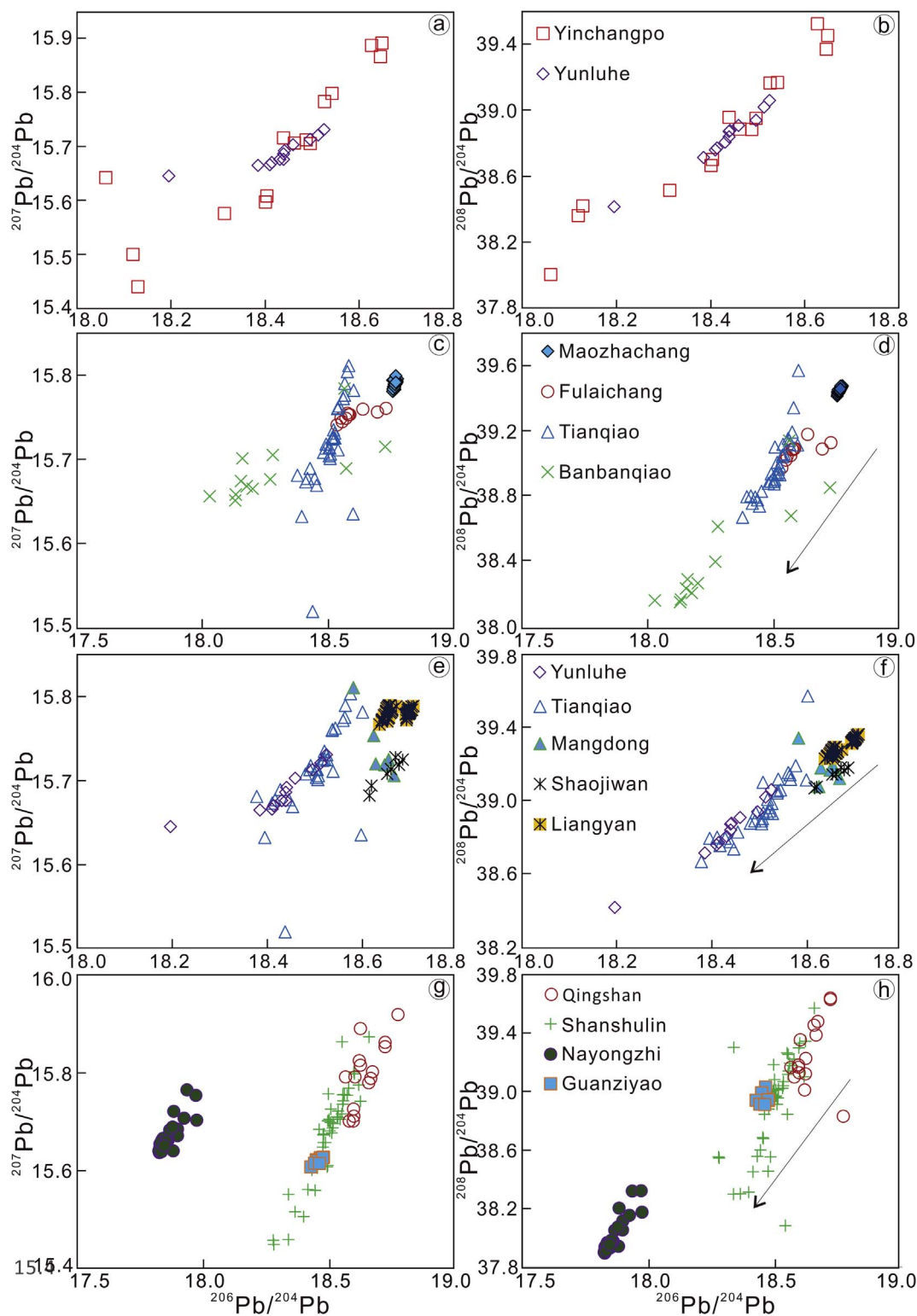
Fig. 31. Comparison plots of $^{207}Pb/^{204}Pb$ vs. $^{206}Pb/^{204}Pb$ (a, c, e and g) and $^{208}Pb/^{204}Pb$ vs. $^{206}Pb/^{204}Pb$ (b, d, f and h) among Pb–Zn deposits selected from different ore-forming tectonic belts in the NW Guizhou district. The sources of data are the same to those in Fig. 30.

(Leach et al., 2005). Additionally, these deposits were also considered to be an example of Mississippi Valley-type (MVT) mineralization (Zhang et al., 2015b; Jin et al., 2016b; Chen et al., 2017). The classical MVT deposits occur within extensional zones inboard of orogenic belts and lack spatially or genetically associated with igneous activities, and the formation of them is related to basinal brines, which are characterized by low temperatures (50–200 °C) and high salinities

(10–30 wt% NaCl equiv.) (Leach et al., 2005, 2010; Wilkinson, 2010). However, Pb–Zn deposits in the NW Guizhou district occurs within compressional zones (reverse fault-anticline tectonic systems) of passive margin tectonic settings (western Yangtze Block), and has spatial and genetic (thermal flow, volatiles and fluids) association with the ELIP (Figs. 2a and b, 20–34; Zhou et al., 2018b). Moreover, these deposits are characterized by high ore grades (> 10 wt% Pb + Zn), high
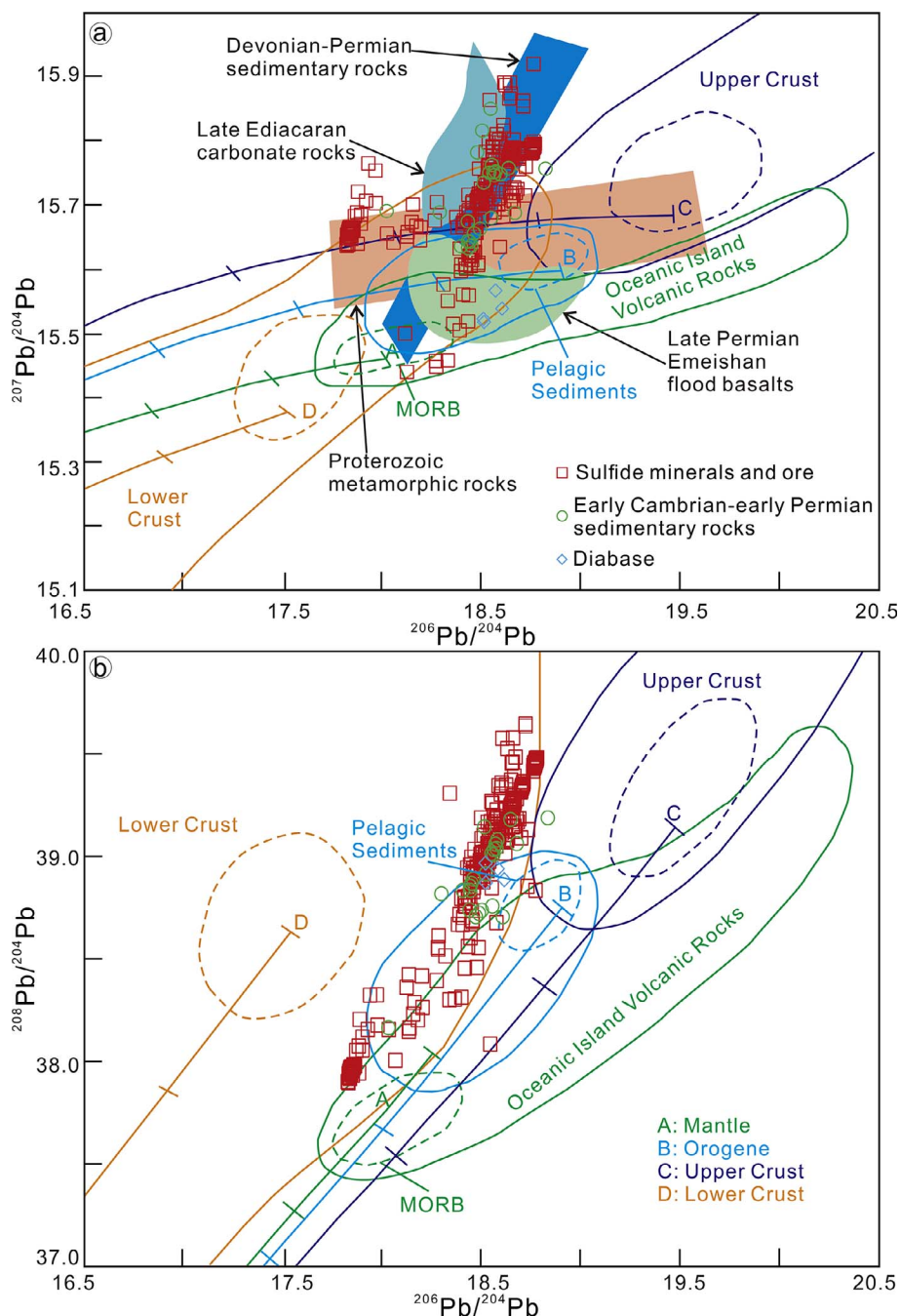
Fig. 32. Comparison plots of $^{207}Pb/^{204}Pb$ vs. $^{206}Pb/^{204}Pb$ (a) and $^{208}Pb/^{204}Pb$ vs. $^{206}Pb/^{204}Pb$ (b) among Pb–Zn deposits, sedimentary rocks, metamorphic rocks and igneous rocks in the studied district and adjacent area, and evolution lines and modern fields of upper crust, lower crust, orogene, and mantle. The sources of data of Pb–Zn deposits and rocks are the same to those in Fig. 30. Solid lines enclose 80% of all data points for each field, and dashed lines enclose probable average values (Zartman and Doe, 1981).

concentrations of associated elements (Cu, Ag, Ge, Ga and Cd), and medium-low temperatures (< 300 °C) and salinities (< 20 wt% NaCl equiv.) (e.g. Jin, 2008; Zhou et al., 2013a, 2013b, 2014a, 2014b, 2018b; Jin et al., 2016b; Zhu et al., 2016a). Furthermore, recent researches shown that there are existing indirect links with sediment-hosted base metal sulfide deposits (such as MVT and SEDEX-type) and mantle plumes (Pirajno, 2000; Xu et al., 2014; Davidheiser-Kroll et al., 2014; Zhou et al., 2018b). For example, in the Irish Pb–Zn ore district, hydrothermal fluids responsible for the Irish-type carbonate-hosted base metal deposits were considered to be driven by mantle heat (Davidheiser-Kroll et al., 2014). In this study, we find that the ELIP plays a crucial role in the formation of these Pb–Zn deposits in the Upper Yangtze province, for specific performance in: (i) the thermal flow and volatiles generated by the ELIP elevated the background geothermal gradient, and the ELIP began to release fluids at ~5–10 Ma after its basalts underplating and eruption, and this process can last

over ~50 Ma as suggested by thermal simulation (Xu et al., 2014). Such time exactly covers the ore-forming ages of basalts-hosted native Cu deposits (230–225 Ma; Zhu et al., 2007), Carlin-type Au deposits (235–204 Ma; Chen et al., 2015) and carbonate-hosted Pb–Zn deposits (245–190 Ma; Zhou et al., 2013a, 2013e, 2015, 2018b; Zhang et al., 2015b); (ii) if we consider the Pb–Zn deposits as a consequence of Indosinian tectonism (~257–200 Ma: Carter et al., 2001; Lepvrier et al., 2004; Enkelmann et al., 2007; Reid et al., 2007; Pullen et al., 2008), then it makes sense that the ELIP-related fluids could pass through the carbonate rocks and be involved in the mineralization, as evidenced by C–O (Figs. 20 and 21), S (Figs. 24–25 and 27), Zn (Figs. 28 and 29), Pb (Fig. 32) and Sr isotopes (Fig. 34). Hence, we propose that carbonate-hosted epigenetic Pb–Zn deposits in the western Yangtze Block are not a typical MVT mineralization and represent a new unique type of Pb–Zn deposits that are related to the ELIP (Table 2), which are named as the Upper Yangtze-type (previously known as SYG-type: Zhou et al., 2013a,
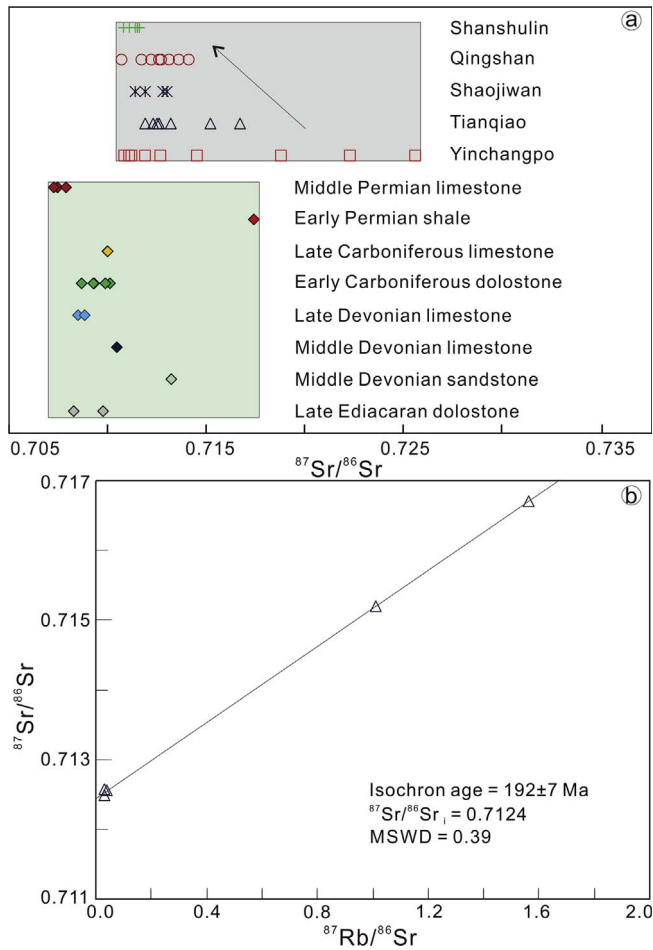
Fig. 33. (a) A comparison plot of $^{87}Sr/^{86}Sr$ between hydrothermal minerals and sedimentary rocks. Data are sourced from Gu et al. (1997), Hu (1999), Deng et al. (2000), Huang et al. (2004), Jiang and Li (2005), Shi et al. (2013), Zhou et al. (2013a, 2013b, 2013c, 2014b), Dou et al. (2014) and Kong et al. (2017); (b) plot of sulfide Rb–Sr isochron age for the Tianqiao Pb–Zn deposit (after Zhou et al., 2013a).

2014b).

In summary, the Upper Yangtze-type Pb–Zn deposits generally place in platform carbonate sequences and are typically occurred within compressional zones of passive margin tectonic settings. They have spatial and genetic association with a large igneous province, and are characterized by high ore grades (> 10 wt% Pb + Zn), high concentrations of associated metals (e.g. Cu, Ag, Ge, and Cd), and medium-low temperatures (usually < 300 °C) and salinities (commonly < 20 wt% NaCl equiv.).

10.2. A new genetic model

Integrating all the information, we propose a new "sandwich" model for Pb–Zn deposits in the Upper Yangtze metallogenic province (Fig. 35). This model can be described as follows: (i) underplating and eruption of basalts of the ELIP at ~ 260 Ma (Zhou et al., 2002; Shellnutt, 2014) provided thermal flow, volatiles (including H_2S, CO_2 and H_2O) and fluids (containing Zn and Cu), and elevated background geothermal gradient, both of which facilitated and enhanced the mobilization and extraction of mineralizing metals (e.g. Pb, Zn, and Ag) from basement rocks, and formed initial mixing of mantle and metamorphic fluids. These metal-rich fluids were driven upward along regional deep faults (for example KYZ in Fig. 2a) by mantle heat of the ELIP (Fig. 35a); (ii) during Early Mesozoic (245–190 Ma), the overall tectonic regimes shifted from extension to compression, and then to extension again (Carter et al., 2001; Reid et al., 2007; Lepvrier et al., 2008; Qiu et al., 2016; Hu et al., 2017a, 2017b; Zhou et al., 2018b), causing the initial metal-rich fluids flowed through or interacted with multiple lithostratigraphic units between late Permian Emeishan flood basalts and Proterozoic basement rocks. These metal-rich fluids were released into secondary structural units (for example fault-fold tectonic systems), and were trapped by late Ediacaran to middle Permian sedimentary strata (i.e. platform carbonate sequences) that are rich in organic matters, and some of which contain evaporites (parts of them had been reduced by BSR). Similarly, the multiple S species-bearing solutions were migrated, released, trapped and mixed with metal-rich fluids at the mineralized sites (Fusswinkel et al., 2013; Zhou et al., 2013d; Liu et al., 2017). Under the coupling of "structures (reverse fault-anticline), lithofacies (platform carbonate sequences) and fluids (metal-rich fluids and S-

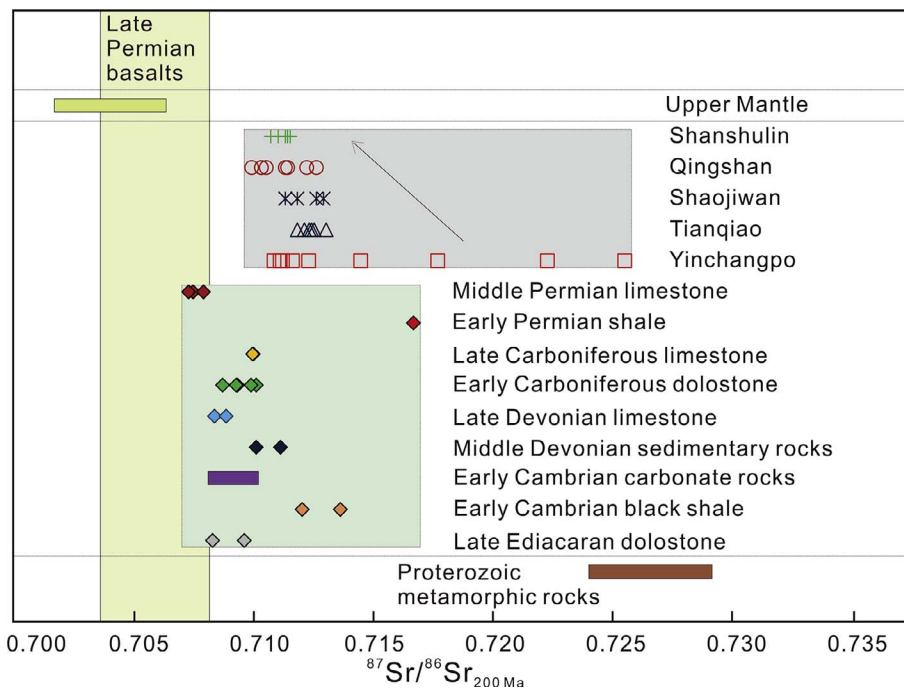**Fig. 34.** A comparison plot of $^{87}Sr/^{86}Sr_{200Ma}$ among hydrothermal minerals, sedimentary rocks, metamorphic rocks, upper mantle and Emeishan basalts. The sources of data are the same to those in Fig. 32, other data are sourced from Faure (1977), Cong (1988), Li and Qin (1988), Chen and Ran (1992) and Kong et al. (2017).

Table 2
A comparison between typical MVT deposits and Pb–Zn deposits in the Upper Yangtze metallogenic province, SW China.

| Characteristics	MVT deposits	Pb–Zn deposits in the Upper Yangtze province
Grades	Pb + Zn: av. < 10 wt%, Zn/(Zn + Pb): 0.8 ±	Pb + Zn: av. 10–35 wt%, Zn/(Zn + Pb): 0.9 ±
Tonnages	Pb + Zn metal reserves: single ore body < 1 Mt	Pb + Zn metal reserves: single ore body 0.1–1.5 Mt
Acreages	Hundreds of square kilometers	This province covers ~ 0.2×10^6 square kilometers
Host rocks	Cambrian to Carboniferous carbonate rocks	Proterozoic to middle Permian carbonate rocks
Depths of mineralization	< 1500 m	> 400–2000 m
Tectonic settings	Typically located within extensional zones inboard of orogenic belts	Typically places within compressional zones of passive margins
Relation with magmatic activity	Generally have the absence of temporally or spatially association with igneous activities	Spatially and genetically association with the ELIP
Ore-controlledfactors	Mainly controlled by open structure and lithology	Controlled by reverse fault-anticline tectonic systems and lithology
Ages	From Proterozoic to Cretaceous	250-200-(156) Ma
Ore textures and structures	Exhibiting disseminated, fine granular, branched, colloidal and massive structures and colloidal, skeleton coarse-crystalline textures	Mainly exhibiting massive structures, and fine-, medium- and coarse-grained textures
Mineral compositions	Sphalerite, galena, pyrite, barite, fluorite, dolomite and calcite	Sphalerite, galena, pyrite, chalcopyrite, dolomite and calcite
Fluid inclusions	10–30 wt% NaCl equiv.; $Cl^- - Na^+ - Ca^{2+} - K^+ - Mg^{2+}$; 50–200 °C	< 20 wt% NaCl equiv.; $Cl^- - Na^+ - Ca^{2+} - Mg^{2+} - SO_4^{2-}$; < 300 °C
Associated metals	Ag	Ag, Cu, Ge, Ga, Cd and In
C–O isotopes	Sourced from carbonate rocks	Mainly generated by W/R interaction between mantle/metamorphic fluids and carbonate rocks
S isotopes	+10 to +25‰, sourced from seawater sulfate	−18 to +25‰, sourced from multiple S reservoirs
Zn isotopes	−1.33 to +0.46‰, unknown	−0.26 to +0.71‰, mainly sourced from mantle-derived rocks of the ELIP, and minor from sediments and basements
Pb isotopes	Complicated Pb isotopic ratios and regional zonation, soured from basements and sediments	Normal and uniform Pb isotopes, sourced from basements and sediments, with variable contributions from ELIP rocks
Sr isotopes	Imply that the fluids were derived from, flowed through or interacted with multiple reservoirs	Imply that the fluids were derived from, flowed through or interacted with multiple reservoirs
Precipitation of sulfide	Reduced S, local sulfate reduction, or metal and reduced S-mixing	Fluid mixing, resulted in sulfate reduction, water/rock interaction, CO_2 degassing and carbonate buffer
References	Leach et al. (2005, 2010), Zhou et al. (2018a)	Zhou et al. (2013a, 2014a, 2015, 2018b), This paper
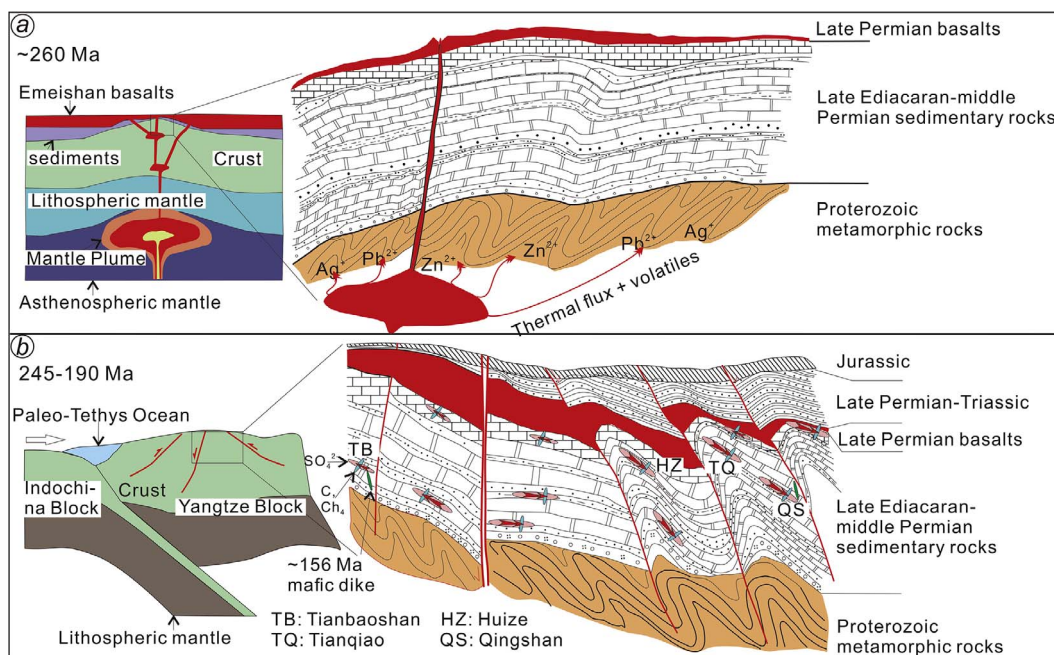
Fig. 35. A new "sandwich" genetic model proposed for the Upper Yangtze Pb–Zn metallogenic province, SW China. (a) at ~ 260 Ma, underplating and eruption of basalts of the ELIP (Zhou et al., 2002; Shellnutt, 2014) provided mantle fluids, and elevated background geothermal gradient and heat flow in the western Yangtze Block, both of which facilitated and enhanced the mobilization and extraction of metals from the Proterozoic basement rocks, and formed initial mixed mantle and metamorphic fluids. These initial fluids were driven upward along regional faults by mantle heat of the EILP; (b) during 245–190 Ma, the overall tectonic regimes shifted from extension to compression, and then to extension again (Carter et al., 2001; Reid et al., 2007; Lepvrier et al., 2008; Qiu et al., 2016; Hu et al., 2017a, 2017b; Zhou et al., 2018b), causing these initial fluids flowed through or interacted with Proterozoic to Paleozoic multiple geological units, and then forming metal-rich fluids. These metal-rich fluids were released into fault-fold tectonic systems and were trapped by platform carbonate sequences that are rich in organic matters, and some of which contain marine sulfate (parts of them had been reduced by bacterial sulfate reduction, BSR). Similarly, the multiple S species-bearing solutions were migrated, released, trapped and mixed with metals-rich fluids at the mineralized sites (Fusswinkel et al., 2013; Zhou et al., 2013d; Liu et al., 2017). Under the coupling of "structures, lithofacies and fluids", through the processes of thermochemical sulfate reduction (TSR), water/rock (W/R) interaction and CO_2 degassing (carbonate buffer), causing the precipitation of hydrothermal minerals and forming the high grade Upper Yangtze-type Pb–Zn deposits in the western Yangtze Block (Zhou et al., 2018b).

bearing solutions)", through the processes of TSR, W/R interaction and CO_2 degassing (carbonate buffer), causing the continuous and huge precipitation of hydrothermal minerals, and forming the high grade Upper Yangtze Pb–Zn metallogenic province (Fig. 35b) (Zhou et al.,

2018b). The Emeishan flood basalts also acted as an impermeable and protective layer, and even as ore-hosting rocks. In addition, the migration paths or evolution of the hydrothermal systems were mainly from west and east to center, namely the mantle/metamorphic-derived

metal-rich fluids were migrated from west to east, whereas the strata-derived S-bearing solutions were transported from east to west, both of which were released, trapped and mixed at the depositional sites that are rich in reduction geochemical barrier (such as organic matters). The S sourced from metamorphic and mantle reservoirs may be trapped at the mineralized areas before metal-rich fluids arrived.

11. Conclusions

(1) More than 400 Pb–Zn deposits in SW China define the giant Upper Yangtze Pb–Zn metallogenic province and formed during Early Mesozoic.

(2) Ore-hosting carbonate rocks, mantle-derived rocks of the ELIP and organic matters within ore-bearing sedimentary strata jointly supplied C and O to the ore-forming fluids.

(3) Multiple sources for S, and the reduction of marine-derived sulfate by both abiotic thermochemical (TSR) and bacterially mediated (BSR) processes were key to the formation of these deposits.

(4) Zn was mainly sourced from ELIP rocks, and minor from sediments and basements. Variations of Zn isotopes were associated with the evolution of fluids during sphalerite precipitation.

(5) Pb was mainly sourced from basement rocks and ore-bearing sedimentary rocks with variable contributions from ELIP rocks.

(6) The carbonate-hosted epigenetic Pb–Zn deposits in the NW Guizhou district are the mixed products of multiple S species-bearing fluids and metal-rich fluids, both of which were derived from, flowed through or interacted with multiple lithostratigraphic units, including basement rocks, ore-bearing sedimentary rocks, and overlying basalts and other ELIP rocks.

(7) The Upper Yangtze Pb–Zn metallogenic province formed in platform carbonate sequences, occurs within compressional zones of passive margin tectonic settings, and is genetically related to a large igneous province, different from typical MVT deposits.

Acknowledgements

Appendix A. Supplementary material

Supplementary data associated with this article can be found, in the online version, at https://doi.org/10.1016/j.jseaes.2017.12.032.

References

Albarède, F., 2004. The stable isotope geochemistry of copper and zinc. Rev. Mineral. Geochem. 55, 409–427.

Ali, J.R., Thompson, G.M., Zhou, M.F., Song, X.Y., 2005. Emeishan large igneous province, SW China. Lithos 79, 475–489.

Bai, J., Huang, Z., Zhu, D., Yan, Z., Zhou, J., 2013. Isotopic compositions of sulfur in the Jinshachang lead-zinc deposit, Yunnan, China, and its implication on the formation of sulfur-bearing minerals. Acta Geol. Sin. 87, 1355–1369.

Bao, Z., Li, Q., Wang, C.Y., 2017. Metal source of giant Huize Zn-Pb deposit in SW China: New constraints from in situ Pb isotopic compositions of galena. Ore Geol. Rev. 91, 824–836.

Bao, Z., Yuan, W., Yuan, H., Liu, X., Chen, K., Zong, C., 2016. Non-matrix-matched determination of lead isotope ratios in ancient bronze artifacts by femtosecond laser ablation multi-collector inductively coupled plasma mass spectrometry. Inter. J. Mass Spectrom. 402, 12–19.

Barker, S.L., Hickey, K.A., Cline, J.S., Dipple, G.M., Kilburn, M.R., Vaughan, J.R., Longo, A.A., 2009. Uncloaking invisible gold: Use of nanoSIMS to evaluate gold, trace elements, and sulfur isotopes in pyrite from Carlin-type gold deposits. Econ. Geol. 104, 897–904.

Basuki, N.I., Taylor, B.E., Spooner, E.T.C., 2008. Sulfur isotope evidence for thermochemical reduction of dissolved sulfate in Mississippi valley type zinc-lead mineralization, Bongara area, northern Peru. Econ. Geol. 103, 183–799.

Beaudoin, G., Chiaradia, M., 2016. Fluid mixing in orogenic gold deposits: Evidence from the H-O-Sr isotope composition of the Val-d'Or vein field (Abitibi, Canada). Chem. Geol. 437, 7–18.

Bottinga, Y., 1968. Calculation of fractionation factors for carbon and oxygen isotopic exchange in the system calcite-carbon dioxide-water. J. Phys. Chem. 72, 800–808.

Bradley, D.C., Leach, D.L., 2003. Tectonic controls of Mississippi Valley-type lead–zinc mineralization in orogenic forelands. Mineral. Deposita 38, 652–667.

Brannon, J.C., Podosek, F.A., McLimans, R.K., 1992. Alleghenian age of the Upper Mississippi Valley zinc-lead deposit determined by Rb-Sr dating of sphalerite. Nature 356, 509–511.

Carr, G.R., Dean, J.A., Suppel, D.W., Heithersay, P.S., 1995. Precise lead isotope fingerprinting of hydrothermal activity associated with Ordovician to Carboniferous metallogenic events in the Lachlan fold belt of New South Wales. Econ. Geol. 90, 1467–1505.

Carter, A., Roques, D., Bristow, C., Kinny, P., 2001. Understanding Mesozoic accretion in Southeast Asia: Significance of Triassic thermotectonism (Indosinian Orogeny) in Vietnam. Geology 29, 211–214.

Changkakoti, A., Gray, J., Krstic, D., Cumming, G.L., Morton, R.D., 1988. Determination of radiogenic isotopes (Rb-Sr, Sm-Nd and Pb-Pb) in fluid inclusion waters: an example from the Bluebell Pb-Zn deposit, British Columbia. Canada. Geochim. Cosmochim. Acta 52, 961–967.

Chaussidon, M., Albarède, F., Sheppard, S.M.F., 1989. Sulphur isotope variations in the mantle from ion microprobe analyses of micro-sulphide inclusions. Earth Planet. Sci. Lett. 92, 144–156.

Chen, H.S., Ran, C.Y., 1992. Isotope Geochemistry of Copper Deposit in Kangdian Area. Geological Publishing House, Beijing, pp. 1–25 (in Chinese).

Chen, G.Y., Wang, L., Fan, Y.M., Zheng, W., 2015a. Ore-search prospect of the deep subsurface in the Wuzhishan Pb-Zn ore field, Guizhou province. Geol. Explor. 51, 859–869 (in Chinese with English abstract).

Chen, W., Kong, Z., Liu, F., Wang, X., Deng, M., Zhao, J., Liu, Y., Zhang, X., 2017. Geology, geochemistry and ore genesis of the Nayongzhi Pb-Zn deposit, Guizhou Province, SW China. Acta Geol. Sin. 91, 1269–1284 (in Chinese with English abstract).

Chen, M., Mao, J., Li, C., Zhang, Z., Dang, Y., 2015b. Re-Os isochron ages for arsenopyrite from Carlin-like gold deposits in the Yunnan-Guizhou-Guangxi "golden triangle", southwestern China. Ore Geol. Rev. 64, 316–327.

Chen, S.J., 1986. A discussion on the sedimentary origin of Pb–Zn deposits in western Guizhou and northeastern Yunnan. Guizhou Geol. 8, 35–39 (in Chinese with English abstract).

Christensen, J.N., Halliday, A.N., Vearncombe, J.R., Kesler, S.E., 1995. Testing models of large-scale crustal fluid flow using direct dating of sulfides Rb-Sr evidence for early dewatering and formation of Mississippi valley-type deposits, Canning Basin, Australia. Econ. Geol. 90, 877–884.

Claypool, G.E., Holser, W.T., Kaplan, I.R., Sakai, H., Zak, I., 1980. The age curves of sulfur and oxygen isotopes in marine sulfate and their mutual interpretation. Chem. Geol. 28, 199–260.

Cong, B.L., 1988. Evolution and Formation on Panxi Rift. Science Press, Beijing, pp. 10–33 (in Chinese).

Davidheiser-Kroll, B., Stuart, F.M., Boyce, A.J., 2014. Mantle heat drives hydrothermal fluids responsible for carbonate-hosted base metal deposits: evidence from ^{3}He/^{4}He of ore fluids in the Irish Pb-Zn ore district. Mineral. Deposita 49, 547–553.

Demény, A., Ahijado, A., Casillas, R., Vennemann, T.W., 1998. Crustal contamination and fluid/rock interaction in the carbonatites of Fuerteventura (Canary Islands, Spain): A C, O, H isotope study. Lithos 44, 101–115.

Deng, H.L., Li, C.Y., Tu, G.Z., Zhou, Y.M., Wang, C.W., 2000. Strontium isotope geochemistry of the Lemachang independent silver ore deposit, northeastern Yunnan, China. Sci. China Earth Sci. 43, 337–346.

Deng, X.H., Chen, Y.J., Bagas, L., Zhou, H.Y., Yao, J.M., Zheng, Z., Wang, P., 2015. Isotope (S-Sr-Nd-Pb) constraints on the genesis of the ca. 850Ma Tumen Mo-F deposit in the Qinling Orogen, China. Precambrian Res. 266, 108–118.

Dou, S., Zhou, J., 2013. Geology and C-O isotope geochemistry of carbonate-hosted Pb-Zn deposits, NW Guizhou Province, SW China. Chin. J. Geochem. 32, 7–18.

Dou, S., Liu, J., Zhou, J., 2014. Strontium isotopic geochemistry of Tianqiao Pb-Zn deposit, Southwest China. Chin. J. Geochem. 33, 131–137.

Duan, J., Tang, J., Lin, B., 2016. Zinc and lead isotope signatures of the Zhaxikang Pb Zn deposit, South Tibet: Implications for the source of the ore-forming metals. Ore Geol. Rev. 78, 58–68.

Enkelmann, E., Weislogel, A., Ratschbacher, L., Eide, E., Renno, A., Wooden, J., 2007. How was the Triassic Songpan-Ganzi basin filled? A provenance study. Tectonic 26. http://dx.doi.org/10.1029/2006TC002078.

Faure, G., 1977. Principles of Isotope Geology. John Wiley & Sons, New York, pp. 28–110.

Fu, S.H., 2004. Metallogenesis of Pb-Zn Deposits and Enrichment Regularity of Dispersed Elements Cd, Ga, and Ge in SW Yangtze Block. PhD thesis (in Chinese with English abstract). Institute of Geochemistry Chinese Academy of Sciences, Guiyang, pp. 1–92.

Fujii, T., Moynier, F., Pons, M.L., Albarède, F., 2011. The origin of Zn isotope fractionation in sulfides. Geochim. Cosmochim. Acta 75, 7632–7643.

Fusswinkel, T., Wagner, T., Wälle, M., Wenzel, T., Heinrich, C.A., Markl, G., 2013. Fluid mixing forms basement-hosted Pb-Zn deposits: Insight from metal and halogen geochemistry of individual fluid inclusions. Geology 41, 679–682.

Gagnevin, D., Boyce, A.J., Barrie, C.D., Menuge, J.F., Blakeman, R.J., 2012. Zn, Fe and S isotope fractionation in a large hydrothermal system. Geochim. Cosmochim. Acta 88, 183–198.

Gao, S., Yang, J., Zhou, L., Li, M., Hu, Z.C., Guo, J.L., Yuan, H.L., Gong, H.J., Xiao, G.Q., Wei, J.Q., 2011. Age and growth of the Archean Kongling terrain, South China, with emphasis on 3.3 Ga granitoid gneisses. Am. J. Sci. 311, 153–182.

Gromek, P., Gleeson, S.A., Simonetti, A., 2012. A basement-interacted fluid in the N81 deposit, Pine Point Pb-Zn district, Canada: Sr isotopic analyses of single dolomite crystals. Mineral. Deposita 47, 749–754.

Groves, D.I., Bierlein, F.P., 2007. Geodynamic settings of mineral deposit systems. J. Geol. Soc. 164, 19–30.

Gu, S.Y., 2007. Study on the sulfur isotope compositions of lead-zinc deposits in northwestern Guizhou Province. J. Guizhou Univ. Technol. 36, 8–13 (in Chinese with English abstract).

Gu, S.Y., Zhang, Q.H., Mao, J.Q., 1997. The strontium isotope evidence for two solutions mixing in Qingshan lead-zinc deposit of Guizhou. J. Guizhou Univ. Technol. 26, 50–54 (in Chinese with English abstract).

Guan, S.P., Li, Z.X., 1999. Pb and S isotope study of carbonate-hosted Pb-Zn deposits at the eastern margin of the Kangdian axis. Geol. Geochem. 27, 45–54 (in Chinese with English abstract).

Habicht, K.S., Canfield, D.E., 1997. Sulfur isotope fractionation during bacterial sulfate reduction in organic-rich sediments. Geochim. Cosmochim. Acta 61, 5351–5361.

He, C.Z., Xiao, Y.L., Wen, H.J., Zhou, T., Zhu, C.W., Fan, H.F., 2016. Zn-S isotopic compositions of the Tianbaoshan carbonate-hosted Pb-Zn deposit in Sichuan, China: Implications for source of ore components. Acta Petrol. Sin. 32, 3394–3406.

Heijlen, W., Muchez, P., Banks, D.A., Schneider, J., Kucha, H., Keppens, E., 2003. Carbonate-hosted Zn-Pb deposits in Upper SiJesia, Poland: Origin and evolution of mineralizing fluids and constraints on genetic models. Econ. Geol. 98, 911–932.

Hoefs, J., 2009. Stable isotope geochemistry, sixth ed., Springer-Verlag Berlin Heidelberg, http://doi: 10.1007/978-3-540-70708-0.

Hu, R., Fu, S., Huang, Y., Zhou, M., Fu, S., Zhao, C., Wang, Y., Bi, X., Xiao, J., 2017a. The giant South China Mesozoic low-temperature metallogenic domain: Reviews and a new geodynamic model. J. Asian Earth Sci. 137, 9–34.

Hu, R.Z., Chen, W.T., Xu, D.R., Zhou, M.F., 2017b. Reviews and new metallogenic models of mineral deposits in South China: An introduction. J. Asian Earth Sci. 137, 1–8.

Hu, Y.G., 1999. Ag Occurrence, Source of Ore-forming Metals and Mechanism of Yinchangpo Ag-Pb-Zn Deposit, Guizhou. Ph.D. Thesis (in Chinese with English abstract). Institute of Geochemistry, Chinese Academy of Sciences, pp. 10–55.

Huang, Z.L., Chen, J., Han, R.S., Li, W.B., Liu, C.Q., Zhang, Z.L., Ma, D.Y., Gao, D.R., Yang, H.L., 2004. Geochemistry and Ore-formation of the Huize Giant Lead-zinc Deposit, Yunnan, Province, China-Discussion on the Relationship Between Emeishan Flood Basalts and Lead-zinc Mineralization (in Chinese). Geological Publishing House, Beijing, pp. 1–204.

Huang, Z., Li, X., Zhou, M., Li, W., Jin, Z., 2010. REE and C-O isotopic geochemistry of calcites from the word-class Huize Pb-Zn deposits, Yunnan, China: Implication for the ore genesis. Acta Geol. Sin. 84, 597–613.

Ikehata, K., Notsu, K., Hirata, T., 2008. In situ determination of Cu isotope ratios in copper-rich materials by NIR femtosecond LA-MC-ICP-MS. J. Anal. Atomic Spectrom. 23, 1003–1008.

Jian, P., Li, D.Y., Kröner, A., Zhang, Q., Wang, Y.Z., Sun, X.M., Zhang, W., 2009. Devonian to Permian plate tectonic cycle of the Paleo-Tethys Orogen in southwest China (II): Insights from zircon ages of ophiolites, arc/back-arc assemblages and within-plate igneous rocks and generation of the Emeishan CFB province. Lithos 113, 767–784.

Jiang, Y.H., Li, S.R., 2005. Study on the isotope data tracing and isotopic chronology in the black-rock series type Ni-Mo deposit in the Lower Cambrian in Hunan and Guizhou provinces. J. Mineral. Petrol. 25, 62–66 (in Chinese with English abstract).

Jiang, S.Y., Lu, J.J., Gu, L.X., Hua, R.M., Jiang, Y.H., 2001. Determination of Cu, Zn, Fe isotopic compositions by MC-ICPMS and their geological applications. Bull. Mineral. Petrol. Geochem. 20, 431–433 (in Chinese with English abstract).

Jin, C.H., Jiang, S.P., Qi, C.L., Zhang, X.G., Zhang, Y., Shen, Z.W., Zhang, D., 2015. Ore-controlling factors and ore prospecting direction of the Maozu deposit. Mineral. Resour. Geol. 29, 1–6 (in Chinese with English abstract).

Jin, X.L., Meng, C.Z., Leng, C.B., Qi, Y.Q., Tang, Y.Y., Zhang, H., Chen, X., 2016a. Element geochemical characteristics and C-O isotopic compositions of Pb-Zn deposit in Yunluhe area of Guizhou and their geolocial implications. J. Earth Sci. Environ. 38, 778–790 (in Chinese with English abstract).

Jin, Z.G., 2008. The Ore-control Factors, Ore-forming Regularity and Ore Forecasting of Pb-Zn Deposits in NW Guizhou Province. Engine Industry Press, Beijing, pp. 1–105 (in Chinese).

Jin, Z.G., Zhou, J.X., Huang, Z.L., Ye, L., Luo, K., Gao, J.G., Chen, X.L., Wang, B., Peng, S., 2016b. Ore genesis of the Nayongzhi Pb-Zn deposit, Puding city, Guizhou Province, China: Evidences from S and in situ Pb isotopes. Acta Petrol. Sin. 32, 3441–3455 (in Chinese with English abstract).

John, S.G., Rouxel, O.J., Craddock, P.R., Engwall, A.M., Boyle, E.A., 2008. Zinc stable isotopes in seafloor hydrothermal vent fluids and chimneys. Earth Planet. Sci. Lett. 269, 17–28.

Jørgenson, B.B., Isaksen, M.F., Jannasch, H.W., 1992. Bacterial sulfate reduction above 100°C in deep sea hydrothermal vent sediments. Science 258, 1756–1757.

Kamona, A.F., Leveque, J., Friedrich, G., Haack, U., 1999. Lead isotopes of the carbonate-hosted Kabwe, Tsumeb, and Kipushi Pb-Zn-Cu sulphide deposits in relation to Pan African orogenesis in the Damaran-Lufilian fold belt of Central Africa. Mineral. Deposita 34, 273–283.

Kelley, K.D., Wilkinson, J.J., Chapman, J.B., Crowther, H.L., Weiss, D.J., 2009. Zinc isotopes in sphalerite from base metal deposits in the Red Dog district, Northern Alaska. Econ. Geol. 104, 767–773.

Kump, L.R., Arthur, M.A., 1999. Interpreting carbon-isotope excursions: Carbonates and organic matter. Chem. Geol. 161, 181–198.

Kong, Z., Wu, Y., Liang, T., Zhang, F., Meng, X., Lu, L., 2017. Sources of ore-forming material for Pb-Zn deposits in the Sichuan-Yunnan-Guizhou triangle area: Multiple constraints from C-H-O-S-Pb-Sr isotopic compositions. Geol. J. http://dx.doi.org/10.1002/gj.3019.

Leach, D.L., Rowan, E.L., 1986. Genetic link between Ouachita foldbelt tectonism and the Mississippi Valley-type lead-zinc deposits of the Ozarks. Geology 14, 931–935.

Leach, D.L., Bradley, D.C., Huston, D., Pisarevsky, S.A., Taylor, R.D., Gardoll, S.J., 2010. Sediment-hosted lead-zinc deposits in Earth history. Econ. Geol. 105, 593–625.

Leach, D.L., Sangster, D., Kelley, K.D., Large, R.R., Garven, G., Allen, C., Gutzmer, J., Walters, S., 2005. Sediment-hosted lead-zinc deposits: A global perspective. Econ. Geol. 100th Anniversary, 561–607.

Lepvrier, C., Maluski, H., Tich, V.V., Leyreloup, A., Thi, P.T., Vuong, N.V., 2004. The early Triassic Indosinian orogeny in Vietnam (Truong Son Belt and Kontum Massif): Implications for the geodynamic evolution of Indochina. Tectonophysics 393, 87–118.

Lepvrier, C., Vuong, N.V., Maluski, H., Thi, P.T., Tich, V.V., 2008. Indosinian tectonics in Vietnam. Comp. Rend. Geosci. 340, 94–111.

Li, F.H., Qin, J.M., 1988. Presinian System in Kangdian Area. Chongqing Press, Chongqing, pp. 15–45 (in Chinese).

Li, Q.L., Chen, F.K., Wang, X.L., Li, C.F., 2005. Ultra-low procedural blank and the single grain mica Rb–Sr isochron dating. Chin. Sci. Bull. 50, 2861–2865.

Li, W.B., Huang, Z.L., Yin, M.D., 2007. Dating of the giant Huize Zn-Pb ore field of Yunnan province, southwest China: Constraints from the Sm-Nd system in hydrothermal calcite. Resour. Geol. 57, 90–97.

Li, B., Zhou, J., Li, Y., Chen, A., Wang, R., 2016. Geology and Isotope geochemistry of the Yinchanggou-Qiluogou Pb-Zn Deposit, Sichuan Province, Southwest China. Acta Geol. Sin. 90, 1768–1779.

Li, B., Zhou, J.X., Huang, Z.L., Yan, Z.F., Bao, G.P., Sun, H.R., 2015. Geological, rare earth elemental and isotopic constraints on the origin of the Banbanqiao Zn–Pb deposit, southwest China. J. Asian Earth Sci. 111, 100–112.

Li, H., Zhang, Z., Santosh, M., Lv, L., Han, L., Liu, W., 2017. Late Permian basalts in the Yanghe area, eastern Sichuan Province, SW China: Implications for the geodynamic of the Emeishan flood basalts province and Permian global mass extinction. J. Asian Earth Sci. 134, 293–308.

Lin, Z.Y., Wang, D.H., Zhang, C.Q., 2010. Rb-Sr isotopic age of sphalerite from the Paoma lead-zinc deposit in Sichuan Province and its implications: Geol. China 37, 488–1196 (in Chinese with English abstract).

Liu, H.C., Lin, W.D., 1999. Study on the law of Pb-Zn-Ag ore deposit in northeast Yunnan, China. Yunnan University Press, Kunming, pp. 1–468.

Liu, X., Liang, Q., Li, Z., Castillo, P.R., Shi, Y., Xu, J., Huang, X., Liao, S., Huang, W., Wu, W., 2017a. Origin of Permian extremely high Ti/Y mafic lavas and dykes from western Guangxi, SW China: Implications for the Emeishan mantle plume magmatism. J. Asian Earth Sci. 141, 97–111.

Liu, W.H., Zhang, J., Wang, J., 2017b. Sulfur isotope analysis of carbonate-hosted Zn–Pb deposits in northwestern Guizhou Province, Southwest China: Implications for the source of reduced sulfur. J. Geochem. Explor. 181, 31–44.

Machel, H.G., Krouse, H.R., Sassen, R., 1995. Products and distinguishing criteria of bacterial and thermo-chemical sulfate reduction. Appl. Geochem. 10, 373–389.

Machel, H.G., 2001. Bacterial and thermochemical sulfate reduction in diagenetic settings—old and new insights. Sediment. Geol. 140, 143–175.

Mao, J.W., Zhou, Z.H., Feng, C.Y., Wang, Y.T., Zhang, C.Q., Peng, H.J., Miao, Y., 2012. A preliminary study of the Triassic large-scale mineralization in China and its geodynamic setting. Geol. China 39, 1437–1471 (in Chinese with English abstract).

Mao, J.Q., Zhang, Q.H., Gu, S.Y., 1998. Tectonic Evolution and Pb-Zn Mineralization of Shuicheng Fault Subsidence. Guizhou Science and Technology Publishing Company, Guiyang, pp. 104–129 (in Chinese).

Mao, D.M., 2000. Oxygen and carbon isotope in Guizhou Tianqiao Pb-Zn deposit. J. Guizhou Univ. Technol. 29, 8–11 (in Chinese with English abstract).

Maréchal, C.N., Sheppard, S.M.F., 2002. Isotopic fractionation of Cu and Zn between chloride and nitrate solutions and malachite or smithsonite at 30 °C and 50 °C. Goldschmidt Conf. Geochim. Cosmochim. Acta 66, A484.

Marsh, E., Hitzman, M.W., Leach, D.L., 2016. Critical elements in sediment-hosted deposits (clastic-dominated Zn-Pb-Ag, Mississippi Valley-type Zn-Pb, sedimentary rock-hosted Stratiform Cu, and carbonate-hosted Polymetallic Deposits): A review. Econ. Geol. Special Review Chapter 12, 307–321.

Mason, T.F.D., Weiss, D.J., Chapman, J.B., Wilkinson, J.J., Tessalina, S.G., Spiro, B., Horstwood, M.S.A., Spratt, J., Coles, B.J., 2005. Zn and Cu isotopic variability in the Alexandrinka volcanic-hosted massive sulphide (VHMS) ore deposit, Urals, Russia. Chem. Geol. 221, 170–187.

Muchez, P., Heijlen, W., Banks, D., Blundell, D., Boni, M., Grandia, F., 2005. Extensional tectonics and the timing and formation of basin-hosted deposits in Europe. Ore Geol. Rev. 27, 241–267.

Nakai, S.I., Halliday, A.N., Kesler, S.E., Jones, H.D., 1990. Rb-Sr dating of sphalerites from Tennessee and the genesis of Mississippi Valley type ore-deposits. Nature 346, 354–357.

Nishizawa, M., Maruyama, S., Urabe, T., Takahata, N., Sano, Y., 2010. Micro-scale (1.5 μm) sulphur isotope analysis of contemporary and early Archean pyrite. Rapid Commun. Mass Spectrom. 24, 1397–1404.

Ohmoto, H., 1972. Systematics of sulfur and carbon isotopes in hydrothermal ore deposits. Econ. Geol. 67, 551–579.

Ohmoto, H., Goldhaber, M.B., 1997. Sulfur and carbon isotopes. In: Barnes, H.L. (Ed.), Geochemistry of Hydrothermal Ore Deposits, third ed. Wiley, New York, pp. 517–611.

Ohmoto, H., Kaiser, C.J., Geer, K.A., 1990. Systematic of sulfur isotopes in recent marine sediments and ancient sediment–hosted base metal deposits. In: Herbert, H.K., Ho, S.

E., (Eds.), Stable Isotopes and Fluid Processes in Mineralization. Geol. Dep. Univ. Extens. Univ. Western Australia, 23, pp. 70–120.

O'Neil, J.R., Clayton, R.N., Mayeda, T.K., 1969. Oxygen isotope fractionation in divalent metal carbonates. J. Chem. Phys. 51, 5547–5558.

Pašava, J., Tornos, F., Chrastný, V., 2014. Zinc and sulfur isotope variation in sphalerite from carbonate-hosted zinc deposits, Cantabria, Spain. Mineral. Deposita 49, 797–807.

Pass, H.E., Cookem, D.R., Davidson, G., Maas, R., Dipple, G., Rees, C., Ferreira, L., Taylor, C., Deyell, C.L., 2014. Isotope geochemistry of the northeast zone, Mount Polley alkalic Cu-Au-Ag porphyry deposit, British Columbia: A case for carbonate assimilation. Econ. Geol. 109, 859–890.

Pirajno, F., 2000. Ore Deposits and Mantle Plumes. Springer, Science & Business Media, pp. 1–572. http://doi:10.1007/978-94-017-2502-6.

Pirajno, F., 2013. Large igneous provinces (Xiong'er, Dashigou, 827 Ma Event, Tarim, Emeishan) and the Yanshanian tectono-thermal event of eastern China. The Geology and Tectonic Settings of China's Mineral Deposits, Springer, Netherlands, pp. 547–638.

Powell, T.G., Macqueen, R.W., 1984. Precipitation of sulfide ores and organic matter: sulfate reactions at Pine Point, Canada. Science 224, 63–67.

Pullen, A., Kapp, P., Gehrels, G.E., Vervoort, J.D., Lin, D., 2008. Triassic continental subduction in central Tibet and Mediterranean-style closer of the Paleo-Tethys Ocean. Geology 36, 351–354.

Qiu, L., Tang, S.L., Wang, Q., Yang, W.X., Tang, X.L., Wang, J.B., 2016. Mesozoic geology of southwestern China: Indosinian foreland overthrusting and subsequent deformation. J. Asian Earth Sci. 122, 91–105.

Reid, A., Wilson, C.J.L., Shun, L., Pearson, N., Belousova, E., 2007. Mesozoic plutons of the Yidun Arc, SW China: U-Pb geochronology and Hf isotopic signature. Ore Geol. Rev. 31, 88–106.

Rye, R.O., Sawkins, F.J., 1974. Fluid inclusion and stable isotope studies on the Casapalca Ag-Pb-Zn-Cu deposit, central Andes. Peru. Econ. Geol. 69, 181–205.

Seal, I.R., 2006. Sulfur isotope geochemistry of sulfide minerals. Rev. Mineral. Geochem. 61, 633–677.

Seal, R.R., Alpers, C.N., Rye, R.O., 2000. Stable isotope systematics of sulfate minerals. Rev. Mineral. Geochem. 40, 541–602.

Shellnutt, J.G., 2014. The Emeishan large igneous province. A synthesis. Geosci. Frontiers 5, 369–394.

Shi, H., Huang, S.J., Shen, L.C., Zhang, M., 2013. Strontium isotope composition of the Cambrian Luojiaguo section in Xiushan, Chongqing and its stratigraphic significance. J. Stratigraphy 27, 71–76 (in Chinese with English abstract).

Sonke, J.E., Sivry, Y., Viers, J., Freydier, R., Dejonghe, L., André, L., Aggarwal, J.K., Fontan, F., Dupré, B., 2008. Historical variations in the isotopic composition of atmospheric zinc deposition from a zinc smelter. Chem. Geol. 252, 145–157.

Sun, W.H., Zhou, M.F., Yan, D.P., Li, J.W., Ma, Y.X., 2008. Provenance and tectonic setting of the Neoproterozoic Yanbian Group, western Yangtze Block (SW China). Precambrian Res. 167, 213–236.

Tan, S.C., Zhou, J.X., Li, B., Zhao, J.X., 2017. In situ Pb and bulk Sr isotope analysis of the Yinchanggou Pb-Zn deposit in Sichuan Province (SW China): Constraints on the origin and evolution of hydrothermal fluids. Ore Geol. Rev. 91, 432–443.

Tang, S.K., Ma, X., Li, X.G., Dai, C.G., Zhang, H., Zhou, Q., Kuang, S.D., Yang, K.G., 2012. Pb isotope composition of the Fulaichang lead-zinc ore deposit in northwest Guizhou and its geological implications. Geotecton. Metallogenia 36, 549–558 (in Chinese with English abstract).

Taylor, H.P., Frechen, J., Degens, E.T., 1967. Oxygen and carbon isotope studies of carbonatites from the Laacher See District, West Germany and the Alnö District, Sweden. Geochim. Cosmochim. Acta 31, 407–430.

Taylor, R.D., Leach, D.L., Bradley, D.C., Pisaresky, S.A., 2009. Compilation of mineral resource data for Mississippi Valley-type and clastic-dominated sediment-hosted lead-zinc deposits. U.S. Geological Survey Open-File Report 2009–1297, pp. 1–42.

Tompkins, L.A., Pedone, V.A., Roche, M.T., Groves, D.I., 1994. The Cadjebut deposit as an example of Mississippi Valley-type mineralization on the Lennard Shelf, Western Australia: single episode or multiple events? Econ. Geol. 89, 450–466.

Toutain, J.P., Sonke, J., Munoz, M., Nonell, A., Polvé, M., Viers, J., Freydier, R., Sortino, F., Joron, J.L., Sumarti, S., 2008. Evidence for Zn isotopic fractionation at Merapi volcano. Chem. Geol. 253, 74–78.

Tran, T.H., Polyakov, G.V., Tran, T.A., Borisenko, A.S., Izokh, A.E., Balykin, P.A., Ngo, T.P., Pham, T.D., 2016. Intraplate magmatism and metallogeny of North Vietnam. Springer, Modern Approaches in Solid Earth Sciences, Dordrecht, pp. 1–381. http://doi:10.1007/978-3-319-25235-3.

Veizer, J., Hoefs, J., 1976. The nature of O^{18}/O^{16} and C^{13}/C^{12} secular trends in sedimentary carbonate rocks. Geochim. Cosmochim. Acta 40, 1387–1395.

Wang, Y., Zhu, X.K., 2010. Application of Zn isotopes to study of mineral deposits: A review. Mineral Deposits 29, 843–852 (in Chinese with English abstract).

Wang, C.M., Deng, J., Carranza, E.J.M., Lei, X.R., 2014. Nature, diversity and temporal-spatial distributions of sediment-hosted Pb-Zn deposit in China. Ore Geol. Rev. 56, 327–351.

Wang, C.Y., Wei, B., Zhou, M.F., Minh, D.H., Qi, L., 2017. A synthesis of magmatic Ni-Cu-(PGE) sulfide deposits in the ~260 Ma Emeishan large igneous province, SW China and Northern Vietnam. J. Asian Earth Sci. http://dx.doi.org/10.1016/j.jseaes. 2017. 12.024.

Wang, H.Y., 1993. Geochemistry of Pb-Zn mineralization in Guizhou. Guizhou Geol. 10, 272–290 (in Chinese with English abstract).

Wang, L.J., 1994. Geological and geochemical features of lead-zinc deposits in northwestern Guizhou Province, China. J. Guilin Coll. Geol. 14, 125–130 (in Chinese with English abstract).

Wang, H.Y., Liang, F.L., Zeng, D.Q., 1996. Geology of the Pb-Zn Deposits in Guizhou Province. Guizhou Technological Publishing House, Guiyang, pp. 1–231 (in Chinese).

Wei, A.Y., Xue, C.D., Xiang, K., Li, J., Liao, C., Akhter, Q.J., 2015. The ore-forming process of the Maoping Pb-Zn deposit, northeastern Yunnan, China: Constraints from cathodoluminescence (CL) petrography of hydrothermal dolomite. Ore Geol. Rev. 70, 562–577.

Wilkinson, J.J., 2010. A review of fluid inclusion constraints on mineralization in the Irish ore field and implications for the genesis of sediment-hosted Zn-Pb deposits. Econ. Geol. 105, 417–442.

Wilkinson, J.J., Weiss, D.J., Mason, T.F.D., Coles, B.J., 2005. Zinc isotope variation in hydrothermal systems: preliminary evidence from the Irish Midlands ore field. Econ. Geol. 100, 583–590.

Wilkinson, J.J., Stoffell, B., Wilkinson, C.C., Jeffries, T.E., Appold, M.S., 2009. Anomalously metal-rich fluids form hydrothermal ore deposits. Science 323, 764–767.

Worden, R.H., Smalley, P.C., Oxtoby, N.H., 1995. Gas souring by the thermo chemical sulfate reduction at 140°C. AAPG Bull. 79, 854–863.

Wu, Y., Zhang, C., Mao, J., Ouyang, H., Sun, J., 2013. The genetic relationship between hydrocarbon systems and Mississippi Valley-type Zn-Pb deposits along the SW margin of Sichuan Basin, China. Inter. Geol. Rev. 55, 941–957.

Xiang, D., Wang, L., Qian, Z., 2015. Ore deposit geochemical characteristics and geological implications of Mangdong Pb-Zn deposit, Hezhang City, Guizhou Province, China. Acta Mineral. Sin. 35, 447–452 (in Chinese with English abstract).

Xie, J.R., 1963. Introduction of the Chinese ore deposits. Scientific Books Publishing House Beijing 1–71 (in Chinese).

Xu, Y., Chung, S.L., Jahn, B.M., Wu, G., 2001. Petrologic and geochemical constraints on the petrogenesis of Permian-Triassic Emeishan flood basalts in southwestern China. Lithos 58, 145–168.

Xu, J.F., Suzuki, K., Xu, Y.G., Mei, H.J., Li, J., 2007. Os, Pb, and Nd isotope geochemistry of the Permian Emeishan continental flood basalts: insights into the source of a large igneous province. Geochim. Cosmochim. Acta 71, 2104–2119.

Xu, Y., Huang, Z., Zhu, D., Luo, T., 2014. Origin of hydrothermal deposits related to the Emeishan magmatism. Ore Geol. Rev. 63, 1–8.

Yan, D.P., Zhou, M.F., Song, H.L., Wang, X.W., Malpas, J., 2003. Origin and tectonic significance of a Mesozoic multilayer overthrust system within the Yangtze Block (South China). Tectonophysics 361, 239–254.

Yang, J.H., Zhou, X.H., 2001. Rb-Sr, Sm-Nd, and Pb isotope systematics of pyrite: Implications for the age and genesis of lode gold deposits. Geology 29, 711–714.

Ye, L., Cook, N.J., Ciobanu, C.L., Yuping, L., Qian, Z., Tiegeng, L., Wei, G., Yulong, Y., Danyushevskiy, L., 2011. Trace and minor elements in sphalerite from base metal deposits in South China: a LA-ICPMS study. Ore Geol. Rev. 39, 188–217.

Yin, M., Li, W., Sun, X., 2009. Rb-Sr isotopic dating of sphalerite from the giant Huize Zn-Pb ore field, Yunnan Province, Southwestern China. Chin. J. Geochem. 28, 70–75.

Yuan, H.L., Yin, C., Liu, X., Chen, K.Y., Bao, Z.A., Zong, C.L., Dai, M.N., Lai, S.C., Wang, R., Jiang, S.Y., 2015. High precision *in-situ* Pb isotopic analysis of sulfide minerals by femtosecond laser ablation multi-collector inductively coupled plasma mass spectrometry. Sci. China Earth Sci. 58, 1713–1721.

Zartman, R.E., Doe, B.R., 1981. Plumbotectonics-the model. Tectonophysics 75, 135–162.

Zaw, K., Peters, S.G., Cromie, P., Burrett, C., Hou, Z.Q., 2007. Nature, diversity of deposit types and metallogenic relations of South China. Ore Geol. Rev. 31, 3–47.

Zeng, G., He, L., Zhang, D., Huang, L., Yang, K., 2017. Pb isotopic composition of Guanziyao lead-zinc ore deposits in west Guizhou and its geological implications. Geotecton. Metallogenia 41, 305–314 (in Chinese with English abstract).

Zhang, J., Lin, Y., Yang, W., Shen, W., Hao, J., Hu, S., Cao, M., 2014a. Improved precision and spatial resolution of sulfur isotope analysis using NanoSIMS. J. Anal. Atomic Spectrom. 29, 1934–1943.

Zhang, C., Wu, Y., Wang, D., Chen, Y., Rui, Z., Lou, D., Chen, Z., 2014b. Brief introduction on metallogeny of Pb-Zn deposits in China. Acta Geol. Sin. 88, 2252–2268.

Zhang, C., Liu, H., Wang, D., Chen, Y., Rui, Z., Lou, D., Wu, Y., Jia, F., Chen, Z., Meng, X., 2015a. A preliminary review on the metallogeny of Pb-Zn deposits in China. Acta Geol. Sin. 89, 1333–1358.

Zhang, C., Wu, Y., Hou, L., Mao, J., 2015b. Geodynamic setting of mineralization of Mississippi Valley-type deposits in world-class Sichuan-Yunnan-Guizhou Zn-Pb triangle, southwest China: Implications from age-dating studies in the past decade and the Sm-Nd age of the Jinshachang deposit. J. Asian Earth Sci. 103, 103–114.

Zhang, Q.H., Mao, J.Q., Guang, S.Y., 1998. The studies of ore-forming material sources of metal deposit in Hezhang Pb–Zn mine Shuicheng, Guizhou province. J. Guizhou Univ. Technol. 27, 26–34 (in Chinese with English abstract).

Zhang, H., Meng, C., Qi, Y., Tang, Y., Jin, X., Chen, X., Leng, C., 2016. Sources of the ore-forming material from Yunluheba ore field in northwest Guizhou Province, China: Constraints from S and Pb isotope geochemistry. Acta Mineral. Sin. 36, 271–276 (in Chinese with English abstract).

Zhang, Z., Huang, Z., Zhou, J., Li, X., Jin, Z., Zhang, L., 2011. Study of S isotope geochemistry for the Shaojiwan Pb-Zn deposit, NW Guizhou Province, China. Acta Mineral. Sin. 31, 496–501 (in Chinese with English abstract).

Zheng, Y.F., Hoefs, J., 1993. Carbon and oxygen isotopic covariations in hydrothermal calcites. Mineral. Deposita 28, 79–89.

Zheng, Y.F., 1990. Carbon-oxygen isotopic covariation in hydrothermal calcite during degassing of CO_2. Mineral. Deposita 25, 246–250.

Zheng, C.L., 1994. An approach on the source of ore-forming metals of lead-zinc deposits in Northwestern part, Guizhou, Province. J. Guilin Coll. Geol. 14, 113–124 (in Chinese with English abstract).

Zheng, M.H., Wang, X.C., 1991. Genesis of the Daliangzi Pb-Zn deposit in Sichuan, China. Econ. Geol. 86, 831–846.

Zhong, Y.T., He, B., Mundil, R., Xu, Y.G., 2014. CA-TIMS zircon U-Pb dating of felsic ignimbrite from the Binchuan section: implications for the termination age of Emeishan large igneous province. Lithos 204, 14–19.

Zhou, C.X., Wei, C.S., Guo, J.Y., 2001. The source of metals in the Qilingchang Pb-Zn

deposit, Northeastern Yunnan, China: Pb-Sr isotope constraints. Econ. Geol. 96, 583–598.

Zhou, J., Huang, Z., Zhou, G., Li, X., Ding, W., Bao, G., 2010. Sulfur isotopic compositions of the Tianqiao Pb-Zn ore deposit, Guizhou Province, China: Implications for the source of sulfur in the ore-forming fluids. Chin. J. Geochem. 29, 301–306.

Zhou, J., Huang, Z., Zhou, G., Li, X., Ding, W., Bao, G., 2011. Trace elements and rare earth elements of sulfide minerals in the Tianqiao Pb-Zn ore deposit, Guizhou Province, China. Acta Geol. Sin. 85, 189–199.

Zhou, J., Huang, Z., Zhou, M., Li, X., Jin, Z., 2013a. Constraints of C-O-S-Pb isotope compositions and Rb-Sr isotopic age on the origin of the Tianqiao carbonate-hosted Pb-Zn deposit, SW China. Ore Geol. Rev. 53, 77–92.

Zhou, J., Huang, Z., Bao, G., 2013b. Geological and sulfur-lead-strontium isotopic studies of the Shaojiwan Pb-Zn deposit, southwest China: Implications for the origin of hydrothermal fluids. J. Geochem. Explor. 128, 51–61.

Zhou, J.X., Huang, Z.L., Gao, J.G., Yan, Z.F., 2013c. Geological and C-O-S-Pb-Sr isotopic constraints on the origin of the Qingshan carbonate-hosted Pb-Zn deposit, Southwest China. Inter. Geol. Rev. 55, 904–916.

Zhou, J., Huang, Z., Bao, G., Gao, J., 2013d. Sources and thermo-chemical sulfate reduction for reduced sulfur in the hydrothermal fluids, southeastern SYG Pb-Zn metallogenic province, SW China. J. Earth Sci. 24, 759–771.

Zhou, J., Huang, Z., Yan, Z., 2013e. The origin of the Maozu carbonate-hosted Pb-Zn deposit, southwest China: Constrained by C-O-S-Pb isotopic compositions and Sm-Nd isotopic age. J. Asian Earth Sci. 73, 39–47.

Zhou, J.X., Huang, Z.L., Zhou, M.F., Zhu, X.K., Muchez, P., 2014a. Zinc, sulfur and lead isotopic variations in carbonate-hosted Pb-Zn sulfide deposits, southwest China. Ore Geol. Rev. 58, 41–54.

Zhou, J.X., Huang, Z.L., Lv, Z.C., Zhu, X.K., Gao, J.G., Mirnejad, H., 2014b. Geology, isotope geochemistry and ore genesis of the Shanshulin carbonate-hosted Pb-Zn deposit, southwest China. Ore Geol. Rev. 63, 209–225.

Zhou, J.X., Bai, J.H., Huang, Z.L., Zhu, D., Yan, Z.F., Lv, Z.C., 2015. Geology, isotope geochemistry and geochronology of the Jinshachang carbonate-hosted Pb-Zn deposit, southwest China. J. Asian Earth Sci. 98, 272–284.

Zhou, J.X., Dou, S., Huang, Z.L., Cui, Y.L., Ye, L., Li, B., Gan, T., Sun, H.R., 2016a. Origin of the Luping Pb deposit in the Beiya area, Yunnan Province, SW China: Constraints

from geology, isotope geochemistry and geochronology. Ore Geol. Rev. 72, 179–190.

Zhou, J.X., Luo, K., Li, B., Huang, Z.L., Yan, Z.F., 2016b. Geological and isotopic constraints on the origin of the Anle carbonate-hosted Zn-Pb deposit in northwestern Yunnan Province, SW China. Ore Geol. Rev. 74, 88–100.

Zhou, J.X., Wang, X.C., Wilde, S.A., Luo, K., Huang, Z.L., Wu, T., Jin, Z.G., 2018a. New insights into the metallogeny of MVT Pb-Zn deposits: A case study from the Nayongzhi in South China, using field data, fluid compositions, and in situ S-Pb isotopes. Am. Mineral. http://dx.doi.org/10.2138/am-2018-6238.

Zhou, J.X., Luo, K., Wang, X.C., Wilde, S.A., Wu, T., Huang, Z.L., Cui, Y.L., Zhao, J.X., 2018b. Ore genesis of the Fule Pb-Zn deposit and its relationship with the Emeishan Large Igneous Province. Evidence from mineralogy, bulk C-O-S and in situ S-Pb isotopes. Gondwana Res. 54, 161–179.

Zhou, M.F., Yan, D.P., Kennedy, A.K., Li, Y.Q., Ding, J., 2002. SHRIMP zircon geochronological and geochemical evidence for Neo-Proterozoic arc-related magmatism along the western margin of the Yangtze Block, South China. Earth Planet. Sci. Lett. 196, 1–67.

Zhou, M.F., Zhao, X.F., Chen, W.T., Li, X.C., Wang, W., Yan, D.Y., Qiu, H.N., 2014c. Proterozoic Fe-Cu metallogeny and supercontinental cycles of the southwestern Yangtze Block, southern China and northern Vietnam. Earth Sci. Rev. 139, 59–82.

Zhu, B.Q., Hu, Y.G., Zhang, Z.W., Cui, X.J., Mo, D.M., Chen, G.H., Peng, J.H., Sun, Y.G., Liu, D.H., Chang, X.Y., 2007. Geochemistry and geochronology of native copper mineralization related to the Emeishan flood basalts, Yunnan Province, China. Ore Geol. Rev. 32, 366–380.

Zhu, C., Wen, H., Zhang, Y., Fan, H., 2016a. Cadmium and sulfur isotopic compositions of the Tianbaoshan Zn-Pb-Cd deposit, Sichuan Province, China. Ore Geol. Rev. 76, 152–162.

Zhu, C.W., Wen, H.J., Zhang, Y.X., Fu, S.H., Fan, H.F., Cloquet, C., 2017. Cadmium isotope fractionation in the Fule Mississippi Valley-type deposit, Southwest China. Mineral. Deposita 52, 675–686.

Zhu, G.Y., Fei, A.G., Zhao, J., Liu, C., 2014. Sulfur isotopic fractionation and mechanism for thermochemical sulfate reduction genetic H₂S. Acta Petrol. Sin. 30, 3772–3786.

Zhu, L.Y., Su, W.C., Shen, N.P., Dong, W.D., Cai, J.L., Zhang, Z.W., Zhao, H., Xie, P., 2016b. Fluid inclusion and sulfur isotopic studies of lead-zinc deposits, northwestern Guizhou, China. Acta Petrol. Sin. 32, 3431–3440 (in Chinese with English abstract).